NAVAL POSTGRADUATE SCHOOL

MONTEREY, CALIFORNIA

DISSERTATION

NONLINEAR ESTIMATION WITH SPARSE TEMPORAL MEASUREMENTS

by

Paul J. Frontera

September 2016

Dissertation Supervisor: I. Michael Ross

Approved for public release. Distribution is unlimited.

THIS PAGE INTENTIONALLY LEFT BLANK

REPORT DOCUMENTATION PAGE

Form Approved OMB No. 0704–0188

1. AGENCY USE ONLY *(Leave Blank)*	2. REPORT DATE	3. REPORT TYPE AND DATES COVERED
	September 2016	Dissertation 12-22-2014 to 09-23-2016

4. TITLE AND SUBTITLE

NONLINEAR ESTIMATION WITH SPARSE TEMPORAL MEASUREMENTS

5. FUNDING NUMBERS

6. AUTHOR(S)

Paul J. Frontera

7. PERFORMING ORGANIZATION NAME(S) AND ADDRESS(ES)

Naval Postgraduate School
Monterey, CA 93943

8. PERFORMING ORGANIZATION REPORT NUMBER

9. SPONSORING / MONITORING AGENCY NAME(S) AND ADDRESS(ES)

N/A

10. SPONSORING / MONITORING AGENCY REPORT NUMBER

11. SUPPLEMENTARY NOTES

The views expressed in this document are those of the author and do not reflect the official policy or position of the Department of Defense or the U.S. Government. IRB Protocol Number: N/A.

12a. DISTRIBUTION / AVAILABILITY STATEMENT

Approved for public release. Distribution is unlimited.

12b. DISTRIBUTION CODE

13. ABSTRACT *(maximum 200 words)*

Nonlinear estimators based on the Kalman filter, the extended Kalman filter (EKF) and unscented Kalman filter (UKF) are commonly used in practical application. The Kalman filter is an optimal estimator for linear systems; the EKF and UKF are sub-optimal approximations of the Kalman filter. The EKF uses a first-order Taylor series approximation to linearize nonlinear models; the UKF uses an approximation of the states' joint probability distribution. Long measurement intervals exacerbate approximation error in each approach, particularly in covariance estimation. EKF and UKF performance under varied measurement frequency is studied through two problems, a single dimension falling body and simple pendulum. The EKF is shown more sensitive to measurement frequency than the UKF in the falling body problem. However, both estimators display insensitivity to measurement frequency in the simple pendulum problem. The literature's lack of consensus as to whether the EKF or UKF is the superior nonlinear estimator may be explained through covariance approximation error.

Tools are presented to analyze EKF and UKF measurement frequency sensitivity. Covariance is propagated forward using the approximations of the EKF and UKF. Each propagated covariance is compared for similarity with a Monte Carlo propagation. The similarity of the covariance matrices is shown to predict filter performance. Portions of the state trajectory susceptible to EKF divergence are found using the Frobenius norm of the Jacobian matrix, limiting the need to consider covariance propagation along the entire state trajectory.

Long measurement intervals also reveal a commonly overlooked challenge in UKF application: sigma point selection methods may produce sigma point vectors that violate physical state constraints. Although the UKF can function under this condition over short measurement intervals, unexpected failure may occur without consideration of physical constraints. A novel constrained UKF, using the scaled unscented transform, is proposed to address this issue.

14. SUBJECT TERMS	15. NUMBER OF PAGES
nonlinear estimation, measurement, frequency, EKF, UKF, constrained	147
	16. PRICE CODE

17. SECURITY CLASSIFICATION OF REPORT	18. SECURITY CLASSIFICATION OF THIS PAGE	19. SECURITY CLASSIFICATION OF ABSTRACT	20. LIMITATION OF ABSTRACT
Unclassified	Unclassified	Unclassified	UU

NSN 7540-01-280-5500

Standard Form 298 (Rev. 2–89)
Prescribed by ANSI Std. 239–18

THIS PAGE INTENTIONALLY LEFT BLANK

Approved for public release. Distribution is unlimited.

NONLINEAR ESTIMATION WITH SPARSE TEMPORAL MEASUREMENTS

Paul J. Frontera
Commander, United States Navy
B.S., United States Naval Academy, 1996
M.S., University of Maryland-College Park, 2002
M.S., National Defense University, 2011

Submitted in partial fulfillment of the
requirements for the degree of

DOCTOR OF PHILOSOPHY IN MECHANICAL ENGINEERING
from the
NAVAL POSTGRADUATE SCHOOL
September 2016

Approved by:

I. Michael Ross
Distinguished Professor of Mechanical and Aerospace Engineering
Dissertation Supervisor & Committee Chair

Isaac I. Kaminer
Professor of Mechanical and Aerospace Engineering

Wei Kang
Professor of Applied Mathematics

Ronald J. Proulx
Research Professor of Space Systems Academic Group

Mark Karpenko
Research Associate Professor of Mechanical and Aerospace Engineering

Approved by:

Garth V. Hobson
Chair, Department of Mechanical and Aerospace Engineering

Approved by:

Douglas Moses
Vice Provost for Academic Affairs

THIS PAGE INTENTIONALLY LEFT BLANK

ABSTRACT

Nonlinear estimators based on the Kalman filter, the extended Kalman filter (EKF) and unscented Kalman filter (UKF) are commonly used in practical application. The Kalman filter is an optimal estimator for linear systems; the EKF and UKF are sub-optimal approximations of the Kalman filter. The EKF uses a first-order Taylor series approximation to linearize nonlinear models; the UKF uses an approximation of the states' joint probability distribution. Long measurement intervals exacerbate approximation error in each approach, particularly in covariance estimation. EKF and UKF performance under varied measurement frequency is studied through two problems, a single dimension falling body and simple pendulum. The EKF is shown more sensitive to measurement frequency than the UKF in the falling body problem. However, both estimators display insensitivity to measurement frequency in the simple pendulum problem. The literature's lack of consensus as to whether the EKF or UKF is the superior nonlinear estimator may be explained through covariance approximation error.

Tools are presented to analyze EKF and UKF measurement frequency sensitivity. Covariance is propagated forward using the approximations of the EKF and UKF. Each propagated covariance is compared for similarity with a Monte Carlo propagation. The similarity of the covariance matrices is shown to predict filter performance. Portions of the state trajectory susceptible to EKF divergence are found using the Frobenius norm of the Jacobian matrix, limiting the need to consider covariance propagation along the entire state trajectory.

Long measurement intervals also reveal a commonly overlooked challenge in UKF application: sigma point selection methods may produce sigma point vectors that violate physical state constraints. Although the UKF can function under this condition over short measurement intervals, unexpected failure may occur without consideration of physical constraints. A novel constrained UKF, using the scaled unscented transform, is proposed to address this issue.

THIS PAGE INTENTIONALLY LEFT BLANK

Table of Contents

List of Figures

THIS PAGE INTENTIONALLY LEFT BLANK

List of Tables

THIS PAGE INTENTIONALLY LEFT BLANK

List of Acronyms and Abbreviations

CIUKF	constrained interval unscented Kalman filter
CUKF	constrained unscented Kalman filter
CUT	conjugate unscented transformation
EKF	extended Kalman filter
EKF2	second-order extended Kalman filter
GPS	Global Positioning System
HS	hyper-pseudospectral
IUKF	interval unscented Kalman filter
JBLD	Jensen-Bregman log-det
KF	Kalman filter
MHE	moving horizon estimation
PF	particle filter
PDF	probability density function
SIUKF	sigma-point interval unscented Kalman filter
TIUKF	truncated interval unscented Kalman filter
TUKF	truncated unscented Kalman filter
UKF	unscented Kalman filter
UKF-S	scaled unscented Kalman filter
URNDDR	unscented recursive nonlinear dynamic data reconciliation
UT	unscented transform

THIS PAGE INTENTIONALLY LEFT BLANK

Acknowledgments

I thank my dissertation supervisor, Dr. Ross, for skillfully guiding me through the process and helping me to wander with purpose. Dr. Proulx provided me with a mathematician's vantage that paired well with my operational point of view. Dr. Karpenko ensured that my thoughts transferred intelligibly into my writing. I owe special thanks to all three for the significant hours spent discussing the finer points of nonlinear Kalman filtering. Drs. Kaminer and Kang provided the practitioner's point of view, ensuring that my work contributed to the field. Additionally, Dr. Horner's support was essential for completing the requirements for this degree.

While too numerous to detail, my interactions with other students, faculty and staff improved my education in many meaningful ways.

I thank my family for their support during my academic journey. My parents instilled in me a love of education at an early age. My children, Lillian, Joseph, and Anneliese, provided daily inspiration. Above all, my wife, Lori, has selflessly supported me through completion of this dissertation and my preceding academic pursuits.

THIS PAGE INTENTIONALLY LEFT BLANK

CHAPTER 1:
Introduction

System state determination remains a challenging engineering problem despite advances in measurement technology. Measurements have inherent precision and accuracy uncertainty preventing perfect knowledge of the system state. Additionally, each system state may not be directly measurable in a given application. Furthermore, in some applications, none of the states can be measured directly and the state values must be derived from available measurement information. Fundamental measurement uncertainty and unavailability of state measurements led to the development of state estimation methods.

Estimates are commonly generated through use of a system model, a mathematical representation of the system. Models, like measurements, also have inherent uncertainty in their representation of actual systems. The combination of measurement and system model uncertainty necessitate a probabilistic vice deterministic representation of the state estimate. A stochastic state representation improves understanding of the system state at the expense of increased complexity of estimation techniques.

This dissertation investigates state estimation in instances when not all system states are measurable, measurements are subject to sparse availability relative to system states' potential rate of change, and a nonlinear model describes the system.

1.1 Motivation

Navigation, as defined in *The New American Practical Navigator*, is "the process of planning, recording, and controlling the movement of a craft or vehicle from one place to another" [1]. Navigation recording is the act of determining the vessel's position, "a point defined by stated or implied coordinates," at a specified time [1]. The practice of determining a vessel's position at sea has significantly changed over the course of history, but remains necessary for the safe completion of ocean voyages. Open ocean navigation has traditionally involved taking measurements to celestial bodies, when they are in sight, to record a fix: a position determined without reference to any former position. When celestial bodies are not in sight, the vessel's position must be estimated, traditionally through dead

reckoning. Dead reckoning is the practice of estimating the vessel's position by plotting out the vessel's direction and distance traveled from the last fix [1]. This approach does not accurately account for all forces, such as current and wind, acting on the vessel; therefore, dead reckoning may not produce an adequate solution for safe navigation over an extended time.

The Global Positioning System (GPS) satellite constellation is commonly the primary source for recording position for open ocean navigation today. While the GPS signal is almost continuously available for surface vessels, it remains unavailable to submarines operating at depth. The submarine environment requires the navigator to rely on estimating the vessel's position due to the relative sparsity, both in space and time, of available mapped features. While dead reckoning can provide a rough estimate of position, inertial sensors, first widely employed in the middle of the 20^{th} century, have demonstrated improved accuracy. Inertial navigation systems measure inertial acceleration and rotational velocity, effectively recording all forces acting on a vessel, and integrate these measurements to generate an estimated position.

An exact nonlinear kinematic inertial model exists for a vessel operating near the Earth's surface [2]. However, accurate rotational velocity and linear acceleration measurements in the desired reference frame are required to generate an accurate estimated attitude and position. Calibration techniques exist that use a known reference to determine system alignment errors, sensor bias and scale factors, etc. Although the system alignment is unlikely to significantly change while in operation, inertial sensor bias and scale factors values are known to drift over time. Integrated imprecise rotational velocity measurements will produce an inaccurate estimate of vessel attitude over time and, subsequently, an inaccurate estimate of position. Unfortunately, inertial sensor bias and scale factors cannot be measured directly in the absence of a known reference. Therefore, a technique is required to accurately estimate sensor bias and scale corrections following initial sensor calibration to facilitate accurate position estimation over time.

The state of practice is to use an extension of the Kalman filter, the extended Kalman filter (EKF), to estimate bias and scale factors in inertial navigation systems. The EKF enabled practical application of inertial navigation for land vehicles, aircraft, ships, submarines, and spacecraft [2]. However, each application has different requirements for es-

timated position accuracy and the maximum time between measurements. The submarine navigation problem has particularly challenging requirements, as long duration submerged operations require maintaining an accurate position estimate over an extended measurement interval in the absence of navigation fix information.

This dissertation investigates the hypothesis that an improved parameter mean and covariance estimate will allow for increasing the time between measurements in a nonlinear, Kalman filter (KF)–based parameter estimation technique without significantly impacting the steady state estimation error. Two well-studied problems, a single dimension falling body and a simple pendulum, are considered; each problem employs a nonlinear dynamic process model. These problems are analogous to the submarine inertial navigation problem and provide insight into the effect measurement interval has on parameter estimation. The following literature review provides a general overview of nonlinear estimation techniques.

1.2 Literature Review

Estimation theory development was driven primarily by the desire to determine an optimal system state estimate from noisy measurements. The measurement signal is available at a relatively high rate for a large number of estimation applications. As a result, estimation literature does not focus on the effect of sparse temporal measurements. The submarine inertial navigation problem that motivates this dissertation is an example of the problem type that may benefit from improved understanding of the effect of sparse temporal measurements.

The previous section presents a number of terms used in the literature without definition. The following definitions are provided for clarity in better understanding existing approaches to nonlinear estimation. Additionally, this section provides a general overview of existing approaches to the nonlinear estimation problem along with detailed background on KF–based nonlinear estimation techniques.

A key concept mentioned in the previous section is the state space. Kalman [3] defined this concept intuitively as "some quantitative information (a set of numbers, a function, etc.) which is the least amount of data one has to know about the past behavior of the system in order to predict its future behavior." This concept is vital if one seeks to generate the best possible description of a system from available imperfect measurements. One must at

least develop a description of the system that includes the minimum information necessary to ensure the validity of future predictions. Reliable prediction is not possible should the state space include less than the minimum description.

Imperfect measurements, $y(t) = x_1(t) + w(t)$, are considered to consist of the signal of interest, $x_1(t)$, and an additive noise, $w(t)$ [3]. The problem of determining the state is therefore fundamentally stochastic since $w(t)$ is not directly observable. Kalman [3] additionally notes that observed measurements are often discrete, taking the form of $y(t) = y(t_0), y(t_1), \ldots, y(t_k)$, where t_0 is the first measurement observed and t_k is the most recent observed measurement. If t_i is the time of interest and t_n is the present time, the problem will take on different meaning depending upon the relation between t_n and t_i. The term "estimation" collectively refers to smoothing ($t_i < t_n$), filtering ($t_i = t_n$), and predicting ($t_i > t_n$) [3]. This dissertation is focused on the filtering problem, but the ideas discussed are applicable across the estimation continuum.

State estimation can be approached from two points of view, either as a batch or recursive update. The batch update approach produces an updated state estimate following intervals of collecting measurements. As a result, a delay exists between obtaining information through individual measurement and incorporation of this information in the state estimate. This approach was used by Gauss for the purpose of orbit parameter estimation in the late 18^{th} century [4].

The recursive approach generates a new update immediately following a measurement [5]. The recursive approach is considered in this dissertation as the motivating application benefits from the immediate inclusion of available information.

Nonlinear estimation refers to estimation in which the descriptions of how the system state changes with time and how the measurement relates to the system state are not restricted to the linear form. Equations (1.1) and (1.2) show the estimation problem in a linear or nonlinear form, respectively.

$$\left.\begin{aligned} \dot{x}(t) &= F(t)x(t) + D(t)u(t) + G(t)w(t) \\ y(t) &= H(t)x(t) + v(t) \end{aligned}\right\} \tag{1.1}$$

$$\left.\begin{array}{c} \dot{x}(t) = f(x(t),u(t),t) + d(u(t),t) + g(x(t),t)w(t) \\ y(t) = h(x(t),t,v(t)) \end{array}\right\} \tag{1.2}$$

The estimation problem can also be composed of a combination of linear and nonlinear models.

This dissertation is focused on the problem of estimating the state with infrequently available measurement information. As noted in Section 1.1, the primary goal of the submarine navigation problem is to develop an adequate estimate of the submarine's position with infrequent access to measurement information from external landmarks or beacons. As such, sparse temporal measurements in the dissertation title refer to the infrequency of measurement information in time. The definition of sparse is investigated in Chapter 2.

1.2.1 Problem of Interest

Mathematical formulation of the problem of interest is shown in Equation (1.3).

$$\begin{array}{c} \dot{x}(t) = f(x(t),u(t),t) + G(t)w(t) \\ y(t_k) = h(x(t_k),u(t_k),v(t_k)) \end{array} \tag{1.3}$$

This problem can be viewed as one of using all available noisy measurement information to estimate the system state in a least squares sense. The system dynamics are continuous in this problem, but the available measurements are discrete since measurement information is not continuously available.

1.2.2 Bayesian Inference

Bayesian inference is commonly used to generate a state estimate, $\hat{x}(t)$ at $t = t_k$. The estimate, $\hat{x}(t_k)$, and noisy measurement, $\tilde{y}(t_k)$, are independent assuming that the noise corrupting the measurement signal, $v(t_k)$, and the noise associated with the system dynamics, $w(t)$, are independent. Independent distributions have the property shown in Equation (1.4) [6].

$$Pr(ABC) = Pr(A)Pr(B)Pr(C) \tag{1.4}$$

Therefore, one can use the concept of conditional probability shown in Equation (1.5) combined with Equation (1.4) to formulate an estimate of the state conditioned on the

noisy measurements, Equation (1.6) [5].

$$\begin{aligned} Pr(A|B) &= \frac{Pr(AB)}{Pr(B)} \\ Pr(B|A) &= \frac{Pr(AB)}{Pr(A)} \end{aligned} \tag{1.5}$$

$$Pr(A|B) = \frac{Pr(B|A)Pr(A)}{Pr(B)} \tag{1.6}$$

Bayes' theorem, shown in Equation (1.7) [6], summarizes the concept.

$$Pr(A_j|B) = \frac{Pr(B|A_j)Pr(A_j)}{\sum_{k=1}^{j-1} Pr(B|A_k)Pr(A_k)} \tag{1.7}$$

The prior, or *a priori*, value of A, $P(A_j)$ occurs immediately prior to the observation of event B. The posterior, or *a posteriori*, value of A, $P(A_j|B)$ occurs immediately following the observation of event B. Kalman [3] notes that the *conditional expectation* can be used analogously, allowing the implementation of a finite dimensional recursive filter described in the following section.

1.2.3 Kalman Filter

Kalman [3] applied the state transition method to solve the optimal linear estimation problem for systems with discrete measurements in the form of Equation (1.8) [7].

$$\begin{aligned} \dot{x}(t) &= F(t)x(t) + G(t)w(t),\ w(t) \sim \mathcal{N}(\mathbf{0}, Q(t)) \\ \tilde{y}_k &= H_k x(t_k) + v_k,\ v_k \sim \mathcal{N}(\mathbf{0}, R_k) \end{aligned} \tag{1.8}$$

The process noise, $w(t)$, and the measurement noise, v_k, are assumed independent and Gaussian as shown in Equation (1.8). The assumption of independence allows for application of Bayes' theorem; likewise, independence ensures orthogonality, and therefore optimality of the estimate [3]. The estimate is optimal in the minimum mean squared error sense for linear process and measurement models with zero mean Gaussian noise.

The state and covariance estimates are propagated forward to generate a prediction at the measurement time by integrating Equation (1.9) [5].

$$\begin{aligned} \dot{\hat{x}}(t) &= F(t)(\hat{x}(t), t) \\ \dot{P} &= F(t)P(t) + P(t)F^T(t) + G(t)Q(t)G^T(t) \end{aligned} \tag{1.9}$$

Kalman [3] propagated Equation (1.9) between t_{k-1} and t_k through the application of a state transition matrix, $\Phi_{k|k-1}$, to generate a predicted state vector and covariance matrix. This predicted estimate is used to generate the optimal stochastic estimate of the state in the form of a mean vector and a covariance matrix. The mean vector is produced through a linear combination of the predicted state vector and a weighted residual. The residual, $Res(t_k)$, or innovation, is the difference between the noisy measurement and the predicted measurement as shown in Equation (1.10) [5].

$$Res(t_k) = \tilde{y}_k - H_k \hat{x}_k^- \tag{1.10}$$

The resulting estimated state is a linear combination of the *a priori* estimate and the weighted innovation as shown in Equation (1.11) [5].

$$\begin{aligned} \hat{x}_k^+ &= \hat{x}_k^- + K_k(\tilde{y}_k - H_k \hat{x}_k^-) \\ P_k^+ &= (I - K_k H_k) P_k^- \end{aligned} \tag{1.11}$$

The weight, known as the Kalman gain, K_k, is determined, as shown in Equation (1.12) [5].

$$K_k = P_k^- H_k^T \left(H_k P_k^- H_k^T + R_k \right)^{-1} \tag{1.12}$$

The KF structure requires initialization of a number of factors. These include the process noise variance, Q_i, the measurement noise variance, R_j, and the initial mean, $x(t_0)$, and covariance, $P(t_0)$.[1] The initialization should leverage all information available prior to attempting estimation. Information regarding sensor performance, R_j, can be obtained via experimentation. Similarly, initial mean and covariance assumptions can be obtained through either experimentation or simulation such that the filter is initialized with meaningful information. Selection of Q_i is more challenging since this term should account for any unknown modeling error.

Kalman [3] notes that optimality and convergence are only assured if the dynamic system is linear. Linearity is necessary to guarantee that the mean and covariance matrix completely

[1]The process noise matrix, Q, is a diagonal matrix with terms, Q_i, along the main diagonal that represent the process noise variance associated with each state, x_i. Each state is assumed independent; therefore, off diagonal terms are zero. The measurement noise matrix, R, is also a diagonal matrix with terms, R_j, that represent the measurement noise variance associated with each measurement, $\tilde{y}_j$.

describe the probability density function of the stochastic state variable [8]. Unfortunately, many actual processes are nonlinear dynamic systems and therefore cannot be estimated by the KF without making use of an approximation technique.

The estimated covariance matrix, $P(t)$, will increase appropriately as the time interval between measurements increases for the linear KF [8]. In other words, the uncertainty associated with the *a priori* state estimate grows accurately for long time intervals. The predicted uncertainty may become significantly larger than the measurement uncertainty. Therefore, the filter will effectively trust the measurement information more than the predicted estimate for sparse temporal measurements; this attribute results in an estimate that closely tracks the measurement signal. For this reason, sparse temporal measurements for a linear system will reduce the filter's effectiveness but should not lead to divergence as defined in Section 1.2.7.

1.2.4 Transformation of a Random Variable

Equations (1.13) and (1.14) detail the transformed mean and covariance, respectively, for a time independent transformation, $g(x)$.

$$\begin{aligned} \mu_{g(x)} =& \mathbb{E}[g(x)] \\ =& \int \dots \int g(x)p(x)dx_1 \dots dx_n \end{aligned} \tag{1.13}$$

$$\begin{aligned} \Sigma_{g(x)} =& \mathbb{E}[(g(x) - \mu_{g(x)})(g(x) - \mu_{g(x)})^T] \\ =& \mathbb{E}[(g(x)g(x)^T] - \mu_{g(x)}\mu_{g(x)}^T \end{aligned} \tag{1.14}$$

Linear Transformation

These equations simplify to Equation (1.15) for a linear transformation, $g(x) = Ax + b$, producing the exact transformed mean and covariance matrix using only the mean and

covariance prior to transformation.[2]

$$\begin{aligned} \mu_{g(x)} &= A\mu_x + b \\ \Sigma_{g(x)} &= A\Sigma_x A^T \end{aligned} \tag{1.15}$$

Analytic solutions, like the linear transformation of a random variable shown in Equation (1.15), are not universally available for the transformation of random variables. Instead, one of the following three techniques are commonly employed for approximation in absence of an analytic solution.

Linearization

Linearization entails performing a Taylor series expansion of the nonlinear function, $g(x)$, shown in Equation (1.16).

$$g(x,t) = g(\hat{x},t) + \left.\frac{\partial g}{\partial x}\right|_{x=\hat{x}} (x-\hat{x}) + \frac{1}{2}\left.\frac{\partial^2 g}{\partial x^2}\right|_{x=\hat{x}} (x-\hat{x})(x-\hat{x})^T + \dots \tag{1.16}$$

Once the function, $g(x)$ is linearized, the transformation is performed as shown in Equation (1.15).[3] First-order expansions (i.e., truncation of Equation (1.16) following the first order partial derivative term) are commonly used although higher order Taylor series expansion may be necessary to produce a more accurate approximation. In general, this approach provides a poor approximation in regions where the process is highly nonlinear or x significantly deviates from the linearization point, $\hat{x}$. However, linearization can provide an adequate approximation if both conditions are satisfied [9].

Monte Carlo

The Monte Carlo technique applies the law of large numbers to obtain an asymptotically close approximation of the probability distribution function following any transformation

[2]This transformation is used for the time independent measurement model of the continuous process-discrete measurement time KF.

[3]Higher order Taylor series expansions require corrections to be applied to Equation (1.15).

[10]. Equations (1.17) and (1.18) describe the concept.

$$\mu_{g(x)} \approx \frac{1}{N}\sum_{i=1}^{N} g(x_i) \tag{1.17}$$

$$\begin{aligned}\Sigma_{g(x)} \approx & \frac{1}{N-1}\sum_{i=1}^{N}(g(x_i)-\mu_{g(x)})(g(x_i)-\mu_{g(x)})^T \\ \approx & \frac{1}{N-1}\sum_{i=1}^{N} g(x_i)g(x_i)^T - \frac{1}{N-1}\sum_{i=1}^{N}\left(g(x_i)\mu_{g(x)}^T + \mu_{g(x)}g(x_i)^T\right) \\ & + \frac{1}{N-1}\sum_{i=1}^{N}\mu_{g(x)}\mu_{g(x)}^T\end{aligned} \tag{1.18}$$

This method rapidly succumbs to Bellman's "curse of dimensionality," the exponential increase in number of samples, N, required as the dimension of the random variable increases [9]. As a result, processing the number of samples required to obtain an accurate approximation of a multidimensional random variable may often require more computation time than is available for real time application.

Unscented Transform

Another approach, the unscented transform (UT), is "founded on the intuition that it is easier to approximate a probability distribution than it is to approximate an arbitrary nonlinear function or transformation" [11]. In general, estimation problems require the transformation of $n-$dimension random variables. A set of sigma points, S, shown in Equation (1.19), consists of vectors, χ_i, and corresponding weights, W_i, that approximate any distribution by matching its moments as shown in Equation (1.20). Julier and Uhlmann [11] emphasize that the approximation should be *unbiased* (i.e., weights can be positive or negative, but $\sum_{i=0}^{N} W_i = 1$, where N is the total number of sigma points used to represent the joint probability distribution).

$$S = \{i = 0, 1, \ldots, N : \chi_i, W_i\} \tag{1.19}$$

The UT approach consists of selecting vectors and weights that satisfy the requirements of Equation (1.20) where c is a cost function and $\mathbf{c}$ are nonlinear constraints that specify the

moment matching [11].

$$\min_{S} c\left[S, p_x(x)\right] \quad \text{subject to} \quad \mathbf{c}\left[S, p_x(x)\right] \tag{1.20}$$

For example, the sigma point set shown in Equation (1.22) is the set that minimizes a cost function, c, favoring use of the minimum number of vectors, χ_i, while it exactly matches the first three moments of a Gaussian distribution; the mean, $\bar{x}$, the covariance, P_{xx}, and the skew, $\mathbf{0}$. As such, this sigma point set satisfies the constraints shown in Equation (1.21) [11].

$$\begin{aligned} \mathbf{c}_1\left[S, p_x(x)\right] &= \sum_{i=0}^{p} W_i \chi_i - \bar{x} \\ \mathbf{c}_2\left[S, p_x(x)\right] &= \sum_{i=0}^{p} W_i \left(\chi_i - \bar{x}\right)\left(\chi_i - \bar{x}\right)^T - P_{xx} \\ \mathbf{c}_3\left[S, p_x(x)\right] &= \sum_{i=0}^{p} W_i \left(\chi_i - \bar{x}\right)^3 \end{aligned} \tag{1.21}$$

In general, distribution approximation accuracy improves with the higher order moments being matched. Julier and Uhlmann [12] note that lowest order moments have the greatest impact on approximation accuracy.

Julier et al. [13] detail a symmetric set of $2n$ sigma points that accurately capture the first two moments, as shown in Equation (1.22) where $i = 1, \ldots, n$.

$$\begin{aligned} \chi_i &= \bar{x} + \sqrt{(n+\kappa)P_{xx}} & W_i &= \tfrac{1}{2(n+\kappa)} \\ \chi_{i+n} &= \bar{x} - \sqrt{(n+\kappa)P_{xx}} & W_{i+n} &= \tfrac{1}{2(n+\kappa)} \end{aligned} \tag{1.22}$$

Julier and Uhlmann [12] extend the symmetric sigma point set by incorporating the mean, χ_0, as shown in Equation (1.23) where $i = 1, \ldots, n$.

$$\begin{aligned} \chi_0 &= \bar{x} & W_0 &= \tfrac{\kappa}{n+\kappa} \\ \chi_i &= \bar{x} + \sqrt{(n+\kappa)P_{xx}} & W_i &= \tfrac{1}{2(n+\kappa)} \\ \chi_{i+n} &= \bar{x} - \sqrt{(n+\kappa)P_{xx}} & W_{i+n} &= \tfrac{1}{2(n+\kappa)} \end{aligned} \tag{1.23}$$

This set uses $2n+1$ vectors and corresponding weights to accurately capture a $n-$dimension random variable's mean, $\bar{x}$, and covariance, P_{xx}. The factor, $\kappa \in \mathfrak{R}$, provides some freedom to more closely match the random variable's higher order moments.

The simplex sigma point set was proposed by Julier and Uhlmann [14] to reduce the total

number of sigma point vectors used to represent a distribution to $n+1$ from $2n+1$. Reduced computational requirements provided the motivation to define a smaller set of sigma points since the UT requires propagation of each sigma point vector. Simplex points are generated on the insight that the smallest affine, independent set of points for a given dimension, n, is a set of n points with an additional point necessary to ensure that the covariance is nonsingular. Julier and Uhlmann [14] note that a triangle, formed by 3 points, forms the largest possible set of affinely independent points in a two-dimensional space. A simplex, such as a tetrahedron for a three-dimensional space, defines this set when considering higher dimensions.

The penalty for reducing the number of points from $2n + 1$ to $n + 1$ is distortion of the represented higher-order moments. Whereas the extended symmetric sigma point set properly reflected a Gaussian skew of $\mathbf{0}$, the simplex points do not. The minimal skew simplex sigma points address this by selecting the sigma point vectors and weights in a manner that minimizes the skew in each dimension [14]. This approach reduces the error in matching the skew, the third moment, but does not eliminate it. Weights are selected using the algorithm shown in Equation (1.24) [14], where $0 \leq W_0 \leq 1$. The sigma point vectors, χ_i^{j+1} are found by expanding the vector sequence of Equation (1.25) for $j = 2, \ldots, n$. The vector sequence is initialized as $\left\{\chi_0^1 = [0], \chi_1^1 = \left[\frac{-1}{\sqrt{2W_1}}\right], \chi_2^1 = \left[\frac{1}{\sqrt{2W_1}}\right]\right\}$.

$$W_i = \begin{cases} \frac{1-W_0}{2^n} & \text{for } i = 1 \\ W_1 & \text{for } i = 2 \\ 2^{i-2}W_1 & \text{for } i = 3, \ldots, n+1 \end{cases} \tag{1.24}$$

$$\chi_i^{j+1} = \begin{cases} \begin{bmatrix} \chi_0^j \\ 0 \end{bmatrix} & \text{for } i = 0 \\ \begin{bmatrix} \chi_i^j \\ \frac{-1}{\sqrt{2W_j}} \end{bmatrix} & \text{for } i = 1, \ldots, j \\ \begin{bmatrix} \mathbf{0}_j \\ \frac{1}{\sqrt{2W_j}} \end{bmatrix} & \text{for } i = j+1 \end{cases} \tag{1.25}$$

The spherical simplex sigma points seek to minimize the hyper-sphere radius that bounds

the sigma point vectors to improve numerical stability [15]. The minimal skew simplex sigma point set algorithm is altered to achieve this objective. Weights are selected using the algorithm shown in Equation (1.26), where $0 \leq W_0 \leq 1$. The sigma point vectors, χ_i^{j+1} are found by expanding the vector sequence of Equation (1.25) for $j = 2, \ldots, n$ [15]. The vector sequence is initialized in the same manner as the minimum skew simplex sigma points.

$$W_i = \frac{1 - W_0}{n + 1} \text{ for } i = 1, \ldots, n + 1 \tag{1.26}$$

$$\chi_i^{j+1} = \begin{cases} \begin{bmatrix} \chi_0^{j-1} \\ 0 \end{bmatrix} & \text{for } i = 0 \\ \begin{bmatrix} \chi_i^{j-1} \\ \frac{-1}{\sqrt{j(j+1)W_1}} \end{bmatrix} & \text{for } i = 1, \ldots, j \\ \begin{bmatrix} \mathbf{0}_{j-1} \\ \frac{1}{\sqrt{j(j+1)W_1}} \end{bmatrix} & \text{for } i = j + 1 \end{cases} \tag{1.27}$$

The simplex sigma points are not used in this dissertation since the extended symmetric set has been shown to produce a better estimate of mean and covariance than the simplex sigma point [11].

Sigma points are used in the UT to approximate the integrals in Equations (1.13) and (1.14) as a weighted sum of the transformed points. This approximation is shown in Equations (1.28) and (1.29).

$$\mu_{g(x)} \approx \sum_{i=1}^{N} w^{(i)} g(\chi_i) \tag{1.28}$$

$$
\begin{aligned}
\Sigma_{g(x)} &\approx \sum_{i=1}^{N} w^{(i)}(g(\chi_i) - \mu_{g(x)})(g(\chi_i) - \mu_{g(x)})^T \\
&\approx \sum_{i=1}^{N} w^{(i)}(g(\chi_i)g(\chi_i)^T - g(\chi_i)\mu_{g(x)}^T - \mu_{g(x)}g(\chi_i)^T + \mu_{g(x)}\mu_{g(x)}^T) \\
&\approx \sum_{i=1}^{N} w^{(i)}g(\chi_i)g(\chi_i)^T - \sum_{i=1}^{N} w^{(i)}(g(\chi_i)\mu_{g(x)}^T + \mu_{g(x)}g(\chi_i)^T) \\
&\quad + \sum_{i=1}^{N} w^{(i)}\mu_{g(x)}\mu_{g(x)}^T
\end{aligned}
\tag{1.29}
$$

The quality of the UT approximation for nonlinear transformations may depend upon the initial sigma point set matching the initial distribution's higher order moments.[4] As a result, the quality of the estimated statistics may be adversely impacted for some nonlinear transformations [16].

Gustafsson and Hendeby [16] investigated the impact of these transformation techniques on filter performance. The specific transformation leads to these three nonlinear transformation approaches varying in performance [16]. A nonlinear transformation, $g(x) = x^T x$, that has an analytic solution is used to demonstrate the effect that the transformation approximation has on both the mean and covariance. Many other approaches exist to produce sigma points. These include methods to match higher order moments such as conjugate unscented transformation (CUT) sigma points, presented in [17], and hyper-pseudospectral (HS) points, presented in [18], that can include higher order information in the selection of the sigma points. Frontera et al. [19] extend Gustafsson and Hendeby [16], demonstrating that an UT using HS sigma points that match all moments through the fourth order produces an exact transformation unattainable using the first order Taylor series linearization or Monte Carlo approaches.

This dissertation employs the extended symmetric sigma points, detailed in Equation (1.23), that exactly match a Gaussian distribution's first three moments unless otherwise noted. The linearization, Monte Carlo, and UT techniques are used throughout the dissertation to demonstrate the effect of sparse temporal measurements on nonlinear estimators.

[4] Application of the UT for a linear transformation, $g(x) = Ax + B$, produces nearly exact transformed first and second moments if the sigma point set exactly matches the pre-transformation first and second moments. Any error stems from numerical computation of the summation of the propagated sigma points.

1.2.5 Vector Stochastic Process

Kalman's [3] insight that "a random function of time may be thought of as the output of a dynamic system excited by an independent Gaussian random process," frames the problem of interest. Analogous to the ability to define a state for a deterministic process, the value of a vector stochastic process, $x(t)$, at the immediately previous time, t_{k-1}, provides as much information about $x(t_k)$ as the complete time history $x(t_0), x(t_1), \ldots, x(t_{k-1})$.[5] This is a Markov-1 process, a process in which the current distribution representing the system state evolves from the immediately previous distribution [20].

The evolution of the state's distribution, $p(X,t|Y_{t_{k-1}})$, therefore, can be considered as a series of transition probability densities that have been shown to satisfy the forward Kolmogorov, or Fokker-Planck equation [20]; this partial differential equation is shown in (1.30) [21].

$$\frac{\partial p_x}{\partial t} = -\sum_{i=1}^{n} \frac{\partial p F_i}{\partial x_i} + \frac{1}{2}\sum_{i=1}^{n}\sum_{j=1}^{n} \frac{\partial p \left(GQG^T\right)_{ij}}{\partial x_i \partial x_j} \tag{1.30}$$

p_x is the joint probability density function (PDF) of the $n-$dimension random variable, x.

Equation (1.30) is often challenging to solve for practical problems, forcing practitioners to apply suboptimal estimators instead. Section 1.2.6 provides a brief description of nonlinear estimators that seek to address the potential change in the state's PDF. Sections 1.2.7 and 1.2.8 detail KF–based nonlinear estimators that do not attempt to account for the state's PDF changing with respect to time.

1.2.6 Nonlinear Estimation Techniques

The following three sections describe methods that seek to account for the change in the joint PDF. The joint PDF remains Gaussian in instances when Kalman's assumptions for linearity and Gaussian noise are maintained [20]. As a result, the KF produces an optimal state estimate if these assumptions hold. The EKF and unscented Kalman filter (UKF) techniques do not explicitly account for the change in the joint probability density function. Rather, they operate with an assumption that the approximated conditional mean and covariance remain in proximity to the actual mean and covariance to produce a viable suboptimal state estimate.

[5] This has been shown for both continuous and discrete time processes [8].

Particle Filter

The particle filter (PF) employs a Monte Carlo approach to the nonlinear estimation problem to approximate the multi-dimension integrals required to determine the estimated state [22]. A large number of "particles," state variables randomly drawn from the known pre-transformation state distributions, are used with associated weights to determine a *proportional* representation of the post-transformation distribution [22]. While the post-transformation distribution will not be known exactly to allow for resampling, new particles are drawn based on a weighted sample in the vicinity of the transformed particles. This approach is computationally challenging for applications with a large number of states and is subject to a number of implementation challenges [9].

Moving Horizon Estimation

The moving horizon estimation (MHE) was developed with the goal of incorporating state constraints within a nonlinear estimation algorithm [23]. Since the conditional probability density function, $p(x_k | y_{0,1,\ldots,k})$, is challenging to determine for nonlinear problems, this approach instead leverages the conditional probability density function, $p(x_{0,1,\ldots,k} | y_{0,1,\ldots,k})$, of the full state trajectory [24]. This entails solving a non-convex constrained optimization problem that grows in scope with each time step [24]. The MHE approach is to limit the time window for optimization, thereby reducing computational cost [23].

Exact Nonlinear Filter

As noted above, a forward Kolmogorov partial differential equation must be solved to obtain the optimal solution to a nonlinear estimation problem. Exact nonlinear filters seek to approximate the solution to the partial differential equation using ordinary differential equations. Daum [22] notes that finite dimensional exact filters exist for special cases and that a general exact filter has not yet been discovered.

1.2.7 Extended Kalman Filter

As noted in Section 1.2.3, the KF assumes a linear process and measurement model in order to ensure optimality and convergence. Many applications cannot satisfy this assumption. However, approximation techniques allow application of the KF structure to problems of the form shown in Equation (1.3). The EKF extends the KF to nonlinear systems by using

a Taylor series approximation, introduced in Section 1.2.4, of the process and measurement models to linearize the nonlinear functions [5].

The EKF employs a first-order Taylor series approximation of the process and measurement models. The first-order approximation, obtained by truncating the series after the first-order partial derivatives, is used to reduce the algorithm's computational complexity. Use of higher-order Taylor series approximations improves the approximation accuracy at the expense of additional computational requirements. The second-order extended Kalman filter (EKF2) uses the second-order Taylor series approximation for enhanced accuracy.

The EKF generates the updated mean estimate, $\hat{x}_k^-$, by using the best estimate of the mean following the previous measurement, $\hat{x}_{k-1}^+$, as the initial condition to propagate the nonlinear dynamics, $f\left(x(t)\right)$. The updated covariance estimate, $\hat{P}_k^-$, is generated through use of a first order Taylor series approximation of the nonlinear process model, $f(x(t))$. Function $f(x(t))$ is linearized at $\hat{x}_{k-1}^+$ using Equation (1.31) [5], and the covariance is propagated using Equation (1.32) [5].

$$F(\hat{x}(t),t) = \left.\frac{\partial f(x(t),t)}{\partial x(t)}\right|_{x(t)=\hat{x}(t)} \tag{1.31}$$

$$\begin{aligned} \dot{\hat{x}}(t) &= f(\hat{x}(t),t) \\ \dot{P}(t) &= F(\hat{x}(t),t)P(t) + P(t)F^T(\hat{x}(t),t) + G(t)Q(t)G^T(t) \end{aligned} \tag{1.32}$$

This approach effectively allows for the application of the linear Kalman filter structure; although $\hat{x}_k^-$ and $\hat{P}_k^-$ are only approximately the conditional estimated *a priori* mean and covariance, respectively. As discussed in Section 1.2.5, the nonlinear transformation alters the distribution over time so that the mean and covariance may not uniquely describe the estimated states' PDF. As a result, the EKF may produce a poor approximation in regions where the process is highly nonlinear or the true value of the state significantly deviates from the linearization point. However, linearization can provide an adequate approximation if both conditions are satisfied [9].

The weight, K_k, is determined, as shown in Equation (1.33) [5],

$$K_k = P_k^- H_k^T(\hat{x}_k^-)\left(H_k(\hat{x}_k^-)P_k^- H_k^T(\hat{x}_k^-) + R_k\right)^{-1} \tag{1.33}$$

with H_k, the linearized measurement model, as defined in Equation (1.34) [5].

$$H_k(\hat{x}_k^-) = \left.\frac{\partial h(x(t_k))}{\partial x(t_k)}\right|_{x(t_k)=\hat{x}_k^-} \tag{1.34}$$

The *a priori* state estimate, $\hat{x}_k^-$, is used in conjunction with the measurement to determine the innovation, or residual, $Res(t_k)$, as shown in Equation (1.35) [5].

$$Res(t_k) = \tilde{y}_k - h_k(\hat{x}_k^-) \tag{1.35}$$

The resulting estimated state is a linear combination of the *a priori* estimate and the weighted innovation, as shown in Equation (1.36).

$$\begin{aligned} \hat{x}_k^+ &= \hat{x}_k^- + K_k\left(\tilde{y}_k - h_k(\hat{x}_k^-)\right) \\ P_k^+ &= \left(I - K_k H_k(\hat{x}_k^-)\right) P_k^- \end{aligned} \tag{1.36}$$

The EKF2 uses the same general process to propagate the estimated mean and covariance. Second-order Taylor series approximations of the nonlinear models are employed to improve the mean and covariance estimates. The mean is propagated through the nonlinear function, and a correction term is applied to remove bias in the *a priori* mean estimate. The correction is determined using the second-order linear function approximation. The Kalman gain and *a posteriori* estimate are also adjusted to improve the estimation accuracy [25]. Equation (1.37) [9] shows the change in the *a priori* estimate, where **Tr** is the matrix trace and ϕ_i is a $n \times 1$ zero vector with 1 in the i^{th} element.

$$\begin{aligned} \dot{\hat{x}}(t) &= f(\hat{x}(t),t) + \tfrac{1}{2}\sum_{i=1}^{n}\phi_i \mathbf{Tr}\left[\left.\frac{\partial^2 f_i}{\partial x^2}\right|_{\hat{x}} P\right] \\ \dot{P}(t) &= F(\hat{x}(t),t)P(t) + P(t)F^T(\hat{x}(t),t) + G(t)Q(t)G^T(t) \end{aligned} \tag{1.37}$$

Equation (1.38) shows the correction, Λ_k, to the Kalman gain that incorporates the second order Taylor series information [9].

$$K_k = P_k^- H_k^T(\hat{x}_k^-)\left(H_k(\hat{x}_k^-)P_k^- H_k^T(\hat{x}_k^-) + R_k + \Lambda_k\right)^{-1} \tag{1.38}$$

Equation (1.39) incorporates the second order Taylor series information in the *a posteriori*

estimated mean through the addition of the correction, π_k, and the Kalman gain [9].

$$\begin{aligned} \hat{x}_k^+ &= \hat{x}_k^- + K_k\left(\tilde{y}_k - h_k(\hat{x}_k^-)\right) + \pi_k \\ P_k^+ &= P_k^- - P_k^- H_k^T(\hat{x}_k^-)\left(H_k(\hat{x}_k^-)P_k^- H_k^T(\hat{x}_k^-) + R_k + \Lambda_k\right)^{-1} H_k^T(\hat{x}_k^-)P_k^- \end{aligned} \tag{1.39}$$

The *a posteriori* covariance is improved through incorporation of the Λ_k term in the Kalman gain. The correction terms are detailed in Equation (1.40) [9]. [6]

$$\begin{aligned} \pi_k &= \tfrac{1}{2}\sum_{i=1}^{n} \phi_i \mathbf{Tr}\left[\left.\frac{\partial^2 h_i}{\partial x^2}\right|_{\hat{x}_k^-} P\right] \\ \Lambda_k(i,j) &= \tfrac{1}{2}\mathbf{Tr}\left[\left.\frac{\partial^2 h_i(x_k, t_k)}{\partial x^2}\right|_{\hat{x}_k^-} P_k^- \left.\frac{\partial^2 h_j(x_k, t_k)}{\partial x^2}\right|_{\hat{x}_k^-} P_k^-\right] \end{aligned} \tag{1.40}$$

As noted in Section 1.2.3, the KF estimate is a weighted combination of information obtained from the model and noisy measurements. As such, the possibility exists that the filter can weight the model prediction more than new measurement information. While a desirable feature to ignore heavily degraded measurement information, this weighting can lead to a condition where the filter rejects all measurement information. Maybeck [8] notes that "it is very possible for the filter not to perform as well as it *thinks* it does. If the computed error covariance is inappropriately small, so is the computed gain: the filter weights its internal system model too heavily and discounts data from the *real world* too much, leading to filter estimates not corresponding to true system performance... a condition called divergence." The filter, therefore, fails to perform its desired function and becomes a system liability. Divergence can be detected through consideration of the residual, as discussed in detail in Section 2.3.4. This condition may occur as the result of extended time intervals between measurements leading to underestimation of the covariance matrix.

1.2.8 Unscented Kalman Filter

The UKF employs the KF structure like the EKF, but rather than linearizing the nonlinear model using a Taylor series expansion, it employs the UT, as detailed in Section 1.2.4, to indirectly propagate the estimated mean and covariance of the state in between measurements, to generate the predicted measurement, and to determine the Kalman gain. It does not approximate the nonlinear process and measurement model, but rather propagates

[6] Simon [9] provides additional details along with the derivation of each correction term.

sigma points, χ_i where $i = 1,\ldots,N$, through the actual process and measurement model to generate the post-transformation mean and covariance [11]. This approach theoretically can generate more accurate approximations of the transformed mean and covariance in some instances, leading to improved performance as compared to the EKF [11].

The UKF represents the *a posteriori* state estimate, $\hat{x}_{k-1}^{+}$, as a set of $i = 1,\ldots,N$ weights, ${w_{k-1}^{+}}^{(i)}$, and vectors, ${\chi_{k-1}^{+}}^{(i)}$, where N is the total number of points. Sigma points may be chosen in a number of ways, as discussed in Section 1.2.4. The *a priori* state estimate is produced, as shown in Equation (1.41) [11]. Process noise, Q_{k-1}, increases the estimated covariance [9].

$$\begin{aligned}
\hat{x}_k^{-} = &\ \tfrac{1}{N}\sum_{i=1}^{N} {w_{k-1}^{+}}^{(i)} \int_{t_{k-1}}^{t_k} f(x(t), {\chi_{k-1}^{+}}^{(i)}, t)\ dt \\
\hat{P}_x^{-} = &\ \tfrac{1}{N}\sum_{i=1}^{N} {w_{k-1}^{+}}^{(i)} \left(\int_{t_{k-1}}^{t_k} f(x(t), {\chi_{k-1}^{+}}^{(i)}, t)\ dt - \hat{x}_k^{-}\right) \cdot \\
&\ \left(\int_{t_{k-1}}^{t_k} f(x(t), {\chi_{k-1}^{+}}^{(i)}, t)\ dt - \hat{x}_k^{-}\right)^T + Q_{k-1}
\end{aligned} \tag{1.41}$$

Sigma points representing the *a priori* estimate distribution are selected to match the mean and covariance using the process described in Section 1.2.4. The predicted measurement is calculated, as shown in Equation (1.42) [9].

$$\begin{aligned}
\hat{y}_k &= \tfrac{1}{N}\sum_{i=1}^{N} {w_k^{-}}^{(i)} h({\chi_k^{-}}^{(i)}, t_k) \\
\hat{P}_y &= \tfrac{1}{N}\sum_{i=1}^{N} {w_k^{-}}^{(i)} \left(h({\chi_k^{-}}^{(i)}, t_k) - \hat{y}_k\right)\left(h({\chi_k^{-}}^{(i)}, t_k) - \hat{y}_k\right)^T + R_k
\end{aligned} \tag{1.42}$$

The Kalman gain is selected using the predicted measurement covariance comprised of the propagated predicted measurement covariance and the measurement noise, R_k, as shown in Equation (1.42). The cross covariance between $\hat{x}_k^{-}$ and $\hat{y}_k$ is calculated, as shown in Equation (1.43) [9].

$$\hat{P}_{xy} = \tfrac{1}{N}\sum_{i=1}^{N} {w_k^{-}}^{(i)} \left(\int_{t_{k-1}}^{t_k} f({\chi_{k-1}^{+}}^{(i)}, t_k)\ dt - \hat{x}_k^{-}\right)\left(h({\chi_k^{-}}^{(i)}, t_k) - \hat{y}_k\right)^T \tag{1.43}$$

The Kalman gain is selected, as shown in Equation (1.44) [11].

$$K_k = P_{xy} P_y^{-1} \tag{1.44}$$

The assumption that the measurement noise is uncorrelated with both the *a priori* estimate and estimate error is central to the derivation of the UKF Kalman gain. Although Equation (1.44) appears different from the EKF Kalman gain shown in Equation (1.33), authors of [16] and [26] have shown their equivalence. The UKF measurement update takes the form shown in Equation (1.45) [11].

$$\begin{aligned} \hat{x}_k^+ &= \hat{x}_k^- + K_k \left(\tilde{y}_k - \hat{y}_k \right) \\ P_k^+ &= P_k^- - K_k P_y K_k^T \end{aligned} \tag{1.45}$$

1.2.9 EKF and UKF Performance Comparison

The literature is reviewed for comparison of the EKF and UKF performance in various applications. The following examples of EKF and UKF performance comparisons are provided to demonstrate that despite 20 years having passed since the introduction of the UKF, a clear consensus as to the relative performance of the two approaches remains elusive despite the UT's theoretical second-order accuracy being superior to the first-order Taylor series approximation.

Kurt-Yavuz and Yavuz [27] compare an EKF and UKF application to the simultaneous localization and mapping problem. This work concluded that the UKF outperformed the EKF on average in this application. Ristic et al. [28] came to a similar conclusion for the ballistic re-entry tracking problem. Crassidis [29] presents a comparison of an EKF and UKF in an aircraft inertial navigation system application. GPS measurements are received at a 1 Hz rate. This comparison reveals that the UKF outperformed the EKF in instances with large initialization errors, but similar performance is noted in instances with small initialization errors.

Giannitrapani et al. [30] compared an EKF and UKF, estimating spacecraft position using angles-only measurements from the spacecraft to the Earth and Moon while traveling along a Earth-to-Moon transfer orbit and a geostationary orbit-raising trajectory. Measurements

are taken each hour and the error for both estimators is the same order of magnitude. The EKF and UKF are implemented with different process noises; a larger process noise is used with the EKF to tune the filter for improved consistency. Giannitrapani et al. [30] do not consider varying the measurement frequency, choosing to vary the relative angle between the objects. They conclude that the acUKF demonstrated superior "average localization error and consistency of the estimates."

Allotta et al. [31] discuss the application of an EKF and UKF for estimating the position of an autonomous underwater vehicle. This work centers on a simulation using previously collected sensor information, specifically, a Doppler velocity log to measure speed through water, a pressure transducer to provide depth measurements and an inertial measuring unit. Both filters are initialized with the GPS initial position and the filters are propagated forward in time until another GPS position is received. Filter performance is determined by comparing the EKF and UKF estimated positions with the GPS termination point, respectively. Allotta et al. [31] conclude that the UKF outperformed the EKF on the basis of termination position error. The analysis presented does not investigate the effect of sparse temporal measurements, as the sensor data obtained is not KF measurement data (i.e., GPS position). Rather, the sensor data are actually inputs into the process model. Their work, however, demonstrates that the EKF significantly underestimates the estimated position covariance compared with the UKF.

Rhudy et al. [32] note the lack of a clear consensus in the literature comparing EKF and UKF performance and cite additional examples of performance discrepancies in a wide variety of applications. Rhudy et al. conclude through studying three analytic nonlinear transformations that the UKF provides equal or better performance compared with the EKF in determining the mean, but the covariance determination performance varies. Their approach, however, does not consider the effect of longer propagation intervals on covariance transformation.

One case of direct comparison between the EKF and UKF at varied measurement frequencies is found in the literature. Laviola [33] compared the performance of these two approaches in the case of a virtual reality head and hand tracking example. The frequencies considered, $25\ \text{Hz}, 80\ \text{Hz}$, and $215\ \text{Hz}$, in [33] are relatively fast compared to the system time constant during this experiment. As a result, a significant difference between

the EKF and UKF estimate does not exist. Laviola [33] notes that "if the sampling rate is sufficiently high, ... the error in linearization minimal." This result and interpretation suggest that performance of the EKF and UKF should be nearly identical in any system if the measurement rate frequency is sufficiently fast.

Both estimators in [33] are initialized identically to allow for a comparison in performance. Of interest, process noise, Q_k, is included in both cases and selected in the same manner. Inclusion of process noise covariance establishes the minimum level of confidence that the filter will have in the *a priori* estimate and may mask differences between the approximation approaches. Laviola [33] notes that in the 25 Hz case neither estimator significantly outperforms the raw measurements statistics suggesting that this measurement frequency is not sufficiently fast enough to merit filtering. However, the inclusion of process noise could explain the failure of either filter to outperform the raw measurements along with the EKF outperforming the UKF.

1.3 Contributions

The literature does not contain detailed study of KF–based nonlinear estimator performance with sparse temporal measurements. Therefore, this dissertation investigates the effect of measurement frequency on the EKF and UKF for nonlinear parameter estimation. This approach was chosen in lieu of seeking to either directly solve the forward Kolmogorov partial differential equation or find its approximate solution because the state of practice entails using a version of the KF in operational systems.

KF–based nonlinear estimators employ feedback to correct for approximation errors; feedback provides robust filter performance in most conditions while potentially masking underlying aspects that could lead to unexpected poor performance. This dissertation highlights that comparison between KF–based nonlinear estimators is challenged by the relatively short measurement time intervals found in common application. Differences in estimator performance are explained through study of the filters using longer measurement intervals.

Chapter 2 employs a single-dimension falling body problem to demonstrate that the EKF and UKF may respond differently when subjected to sparse temporal measurements. The propagation of covariance between measurements is shown to cause the difference in esti-

mator performance. Additionally, longer measurement intervals highlight that propagation of an individual sigma point can significantly impact the quality of the UT. Specifically, physical constraint violations may lead to a single sigma point propagation producing unrealistic results that dominate the results from of the all other sigma points. This aspect is overlooked in the literature since the error magnitude is often small over short propagation intervals. A novel approach to implement a constrained UKF is presented to facilitate study of the UKF response under longer measurement intervals. This approach leverages the Julier's scaled UT [34] in a new way that ensures underlying sigma point accurately represent the estimated state while respecting parameter constraints. The measurement update state of the UKF is altered if necessary to ensure that the state estimate respects constraints.

Chapter 3 employs a simple pendulum problem to provide experimental validation of the measurement frequency effect shown through simulation in Chapter 2. The pendulum problem also demonstrates that the effect of sparse temporal measurements is problem dependent. Additionally, this problem illustrates that the UT does not produce a more accurate approximation of a propagated random variable in all instances.

Chapter 4 proposes two complementary techniques for predicting if the propagated covariance will be significantly affected by sparse temporal measurements in a given application. The process model Jacobian is analyzed to locate portions of the state trajectory that may result in significant errors impacting estimator performance. Covariance propagation is analyzed through these regions to determine if filter performance may be impacted by approximation error. This approach facilitates characterization of a problem in advance of filter application, providing the designer with a means of predicting application challenges resulting from measurement frequency.

Conclusions are provided in Chapter 5 along with future work necessary to advance KF–based nonlinear estimation in parameter estimation applications with long measurement intervals.

CHAPTER 2:
Falling Body Problem

A single-dimension falling body problem, described in detail in Section 2.1, is used to demonstrate the effect of sparse temporal measurements on KF–based nonlinear estimators. The details of the simulation are presented in Section 2.2. Section 2.3 simulation results uncover differences in estimator performance as a result of the measurement frequency.

Section 2.4 provides background on constrained UKF. Section 2.5 proposes the scaled unscented Kalman filter (UKF-S) as a method of accounting for parameters that are inequality constrained. This method, based on the traditional UKF, uses scaling of the sigma points and Kalman gain, as necessary, to respect parameter constraints. The falling body problem is used to demonstrate UKF-S application.

2.1 Problem Description

Figure 2.1 depicts an object falling in a single-dimension through an atmosphere while being monitored periodically by a single radar. Equation (2.1) details the states and parameters used in the model.

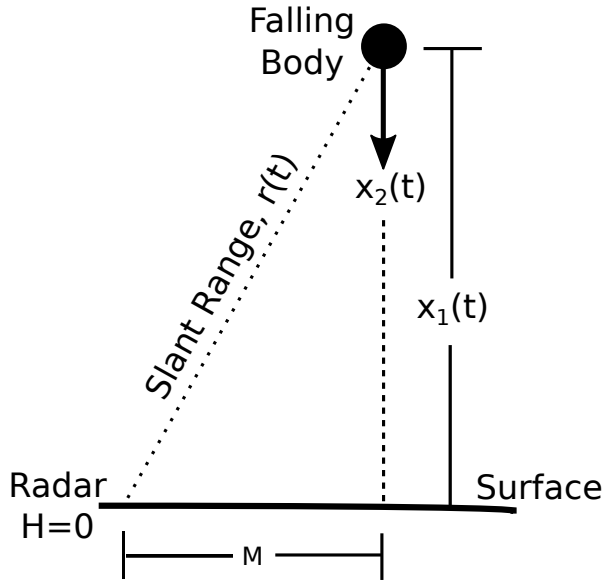

Figure 2.1. Falling body problem. Adapted from [25].

$$\begin{aligned} x_1 &= \text{Altitude, ft} & x_2 &= \text{Velocity, ft/s} \\ x_3 &= \text{Ballistic Coefficient, 1/ft} & x_4 &= \text{Gravitational Acceleration, ft/s}^2 \end{aligned} \tag{2.1}$$

Athans et al. [25] first proposed using this classic problem in a 1968 paper to compare the EKF and EKF2. Athans et al. sought to use a single radar to track multiple objects by increasing interpulse radar transmission periods. Authors of [35], [36], [37] have since used this problem to compare novel estimation techniques with the EKF. An additional parameter, gravitational acceleration, that is usually not considered in the literature is estimated, as shown in Equation (2.1), to increase the dimension of the state space.

Despite using this problem to evaluate nonlinear filter performance, the effect of measurement update frequency was not explicitly considered in [20], [25], [35]–[37]. Each author assumes measurements at a 1 Hz rate.

Equation (2.2) describes $f\left(x(t)\right)$ how each state changes in time while a body falls toward a planet's surface through an atmosphere.

$$\begin{bmatrix} \dot{x}_1 \\ \dot{x}_2 \\ \dot{x}_3 \\ \dot{x}_4 \end{bmatrix} = f(x(t)) = \begin{bmatrix} -x_2 \\ -\exp(-\gamma x_1) x_2^2 x_3 + x_4 \\ 0 \\ 0 \end{bmatrix} + \begin{bmatrix} 0 \\ w_2 \sim \mathcal{N}(0, Q_2) \\ w_3 \sim \mathcal{N}(0, Q_3) \\ 0 \end{bmatrix} \tag{2.2}$$

The process noise, $w_i(t)$, represents the uncertainty associated with the modeled dynamics. As noted in [25] and Section 1.2.7, the process noise is chosen to be Gaussian distributed, $\sim \mathcal{N}(0, Q_i(t))$. Velocity and acceleration in Athans et al. [25] are positive when the body is traveling toward the ground and negative when traveling upward in the atmosphere. γ is a parameter defining the exponential increase in the density of the atmosphere at altitudes close to the surface of the planet. This example assumes a number representative of Earth's atmosphere, $\gamma = 5 \times 10^{-5}$ 1/ft [25].

The ballistic coefficient and gravitational acceleration are constant parameters, $\dot{x}_3 = \dot{x}_4 = 0$, with no anticipated dynamics. The state space describing the system dynamics is augmented with parameters to improve model fidelity as is the practice for inertial navigation

systems. The ballistic coefficient, x_3, is always positive, as defined in Equation (2.3) [25].

$$
\begin{aligned}
x_3 = \tfrac{C_D A \rho_0}{2m} &: \text{ Ballistic Coefficient (1/ft), where} \\
C_D &: \text{Drag Coefficient, dimensionless, } > 0 \text{ by definition} \\
A &: \text{Surface Area, ft}^2 \\
\rho_0 &: \text{Atmospheric Density at surface, lb/ft}^3 \\
m &: \text{Mass, lb}
\end{aligned}
\tag{2.3}
$$

Gravitational acceleration in Athans et al. [25] is positive and acts to attract the body towards the ground since the planet is assumed to be of significantly greater mass than the falling body. The gravitational acceleration is effectively constant over the studied altitude range. Equation (2.4) details the slant range radar measurement equation, $h_k\left(x(t_k)\right)$, used to relate the state to the radar distance measurement [25].

$$
\begin{aligned}
r(t_k) = \sqrt{M^2 + (x_1(t_k) - H)^2}, \text{ where } M&\text{: radar horizontal offset} \\
H&\text{: radar altitude}
\end{aligned}
\tag{2.4}
$$

Measurements are assumed to occur at specified discrete intervals, t_k. The measurement model is nonlinear.

2.2 Simulation Details

The system of equations shown in Equation (2.2) is propagated in time to generate a truth model using MATLAB's *ode*45 function. The model is considered to perfectly represent the system; therefore, the process noise, $w_i(t) = 0$, is nonexistent for each state. Assumed actual initial conditions are $x_1 = 300{,}000$ ft; $x_2 = 20{,}000$ ft/s; $x_3 = 1 \times 10^{-3}$ 1/ft; and $x_4 = 32.17405$ ft/s^2. Figure 2.2 shows the truth model used for this example throughout the dissertation. The nonlinear effect is most prominent in the area highlighted by the blue rectangle between $t = 6$ s and $t = 22$ s. The falling body's rapid exponential deceleration during this time as it interacts with an increasingly dense atmosphere causes this effect.

As shown in Equation (2.5), the radar range measurements are assumed noisy to accurately

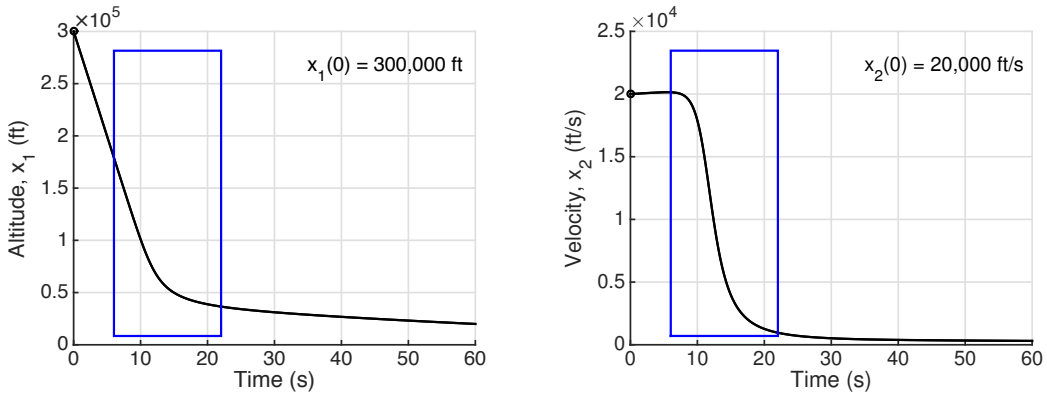

Figure 2.2. Truth generated by propagating initial conditions for the falling body problem: (a) depicts altitude (x_1) and (b) velocity (x_2).

reflect the sensor's inherent measurement uncertainty [25].

$$y(x(t_k)) = r(t_k) + v(t_k), \text{ where } v(t_k)\text{: measurement noise, } \sim \mathcal{N}(0, \sigma^2) \tag{2.5}$$

Results presented assume the radar is on the surface ($H = 0$), providing noisy measurements with $\sim \mathcal{N}(0 \text{ ft}, 1 \times 10^4 \text{ ft}^2)$ distribution. Figure 2.3a highlights the nonlinear relationship between altitude and radar range. A 100 trial Monte Carlo study based on the trajectory depicted in Figure 2.2 is conducted to determine the filter performance. Each trial uses a unique measurement signal corrupted by independent noise. Measurements are generated at a 100 Hz rate and sampled as indicated to test filter performance with longer measurement intervals. Each filter is tested using the same 100 trials to allow performance comparison. Figure 2.3b noisy measurements are a representative example of the measurement error used within each individual trial for filter comparison throughout this section.

The EKF, EKF2, and UKF are initialized identically in mean and covariance to facilitate comparison with respect to the measurement update rate. Results provided in Section 2.3 used the following initialization parameters: altitude, $x_1(0) = 300{,}000$ ft, velocity $x_2(0) = 20{,}000$ ft/s, ballistic coefficient, $x_3(0) = 3 \times 10^{-5}$ 1/ft, and gravitational acceleration, $x_4(0) = 32.17405$ ft/s^2. The ballistic coefficient, $x_3(0)$, is not initialized with the value used to generate the truth since this parameter is likely not well known prior to estimation.

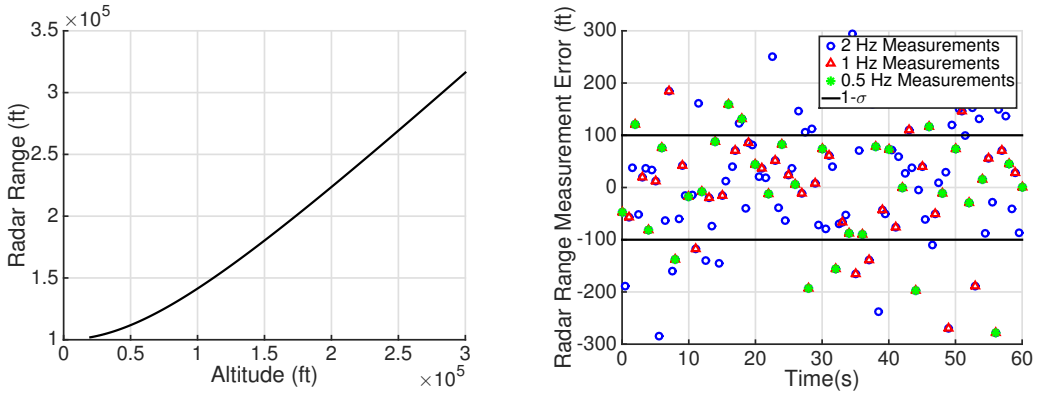

Figure 2.3. Radar slant range measurements: (a) depicts calculated true radar slant range and (b) representative radar measurement error used in simulation.

The variances associated with each state are $P_{x_1}(0) = 1 \times 10^6$ ft^2, $P_{x_2}(0) = 4 \times 10^6$ (ft/s)^2, $P_{x_3} = 1 \times 10^{-4}$ (1/ft)^2, and $P_{x_4} = 1 \times 10^{-4}$ (ft/s^2)^2.[7] The initial level of uncertainty is set to reflect the likely knowledge of each state when estimation commences.

A fixed step, Runge-Kutta fourth-order solver is used to propagate the process model between measurements. The measurement interval determines the total propagation time. The maximum integration step size is limited to 0.01 s to ensure that the integration method does not contribute to degrading the estimate [25]. All filters assume a measurement noise identical to that used to generate the measurements, $\sim \mathcal{N}(0 \text{ ft}, 1 \times 10^4 \text{ ft}^2)$. Although process noise could be introduced to "tune" the EKF [20], it is not considered in this case since the model is known to accurately represent the process.

2.3 Simulation Results

MATLAB is used to conduct a 100 trial Monte Carlo study to compare the performance of the EKF, EKF2, and UKF for varied measurement frequencies. Figure 2.4 shows the average absolute error for each state with the measurement frequency at a 1 Hz rate as is common in the literature. These results are consistent with those obtained by Athans et al. [25]. The EKF2 and UKF outperform the EKF in terms of average absolute steady

[7]These initial conditions are similar to those used by Athans et al. [25].

state altitude and velocity *a posteriori* estimation error. The EKF2 and UKF exhibit similar performance in all states.

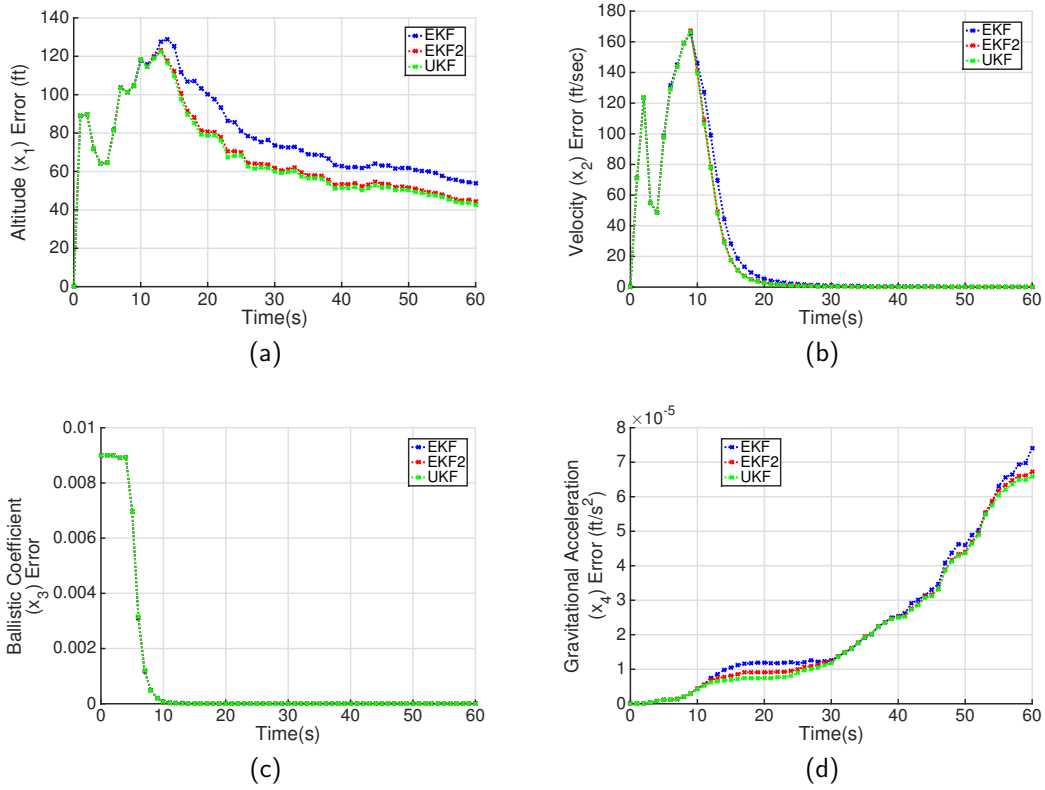

Figure 2.4. Comparison of EKF, EKF2, UKF estimation performance at 1Hz measurements, 100 trial average: (a) depicts average absolute altitude, x_1, error, (b) average absolute velocity, x_2, error, (c) average absolute ballistic coefficient, x_3, error and (d) average absolute gravitational acceleration, x_4, error.

Average absolute error results generated using a lower 0.5Hz measurement frequency are presented in Figure 2.5. At this measurement frequency, the UKF demonstrates superior steady-state performance compared to the EKF and EKF2. Figure 2.5a most clearly highlights the performance difference.

The same simulation is run using denser measurements to determine filter performance with shorter intervals between measurements. Representative results are presented in Figure 2.6 at the 2Hz measurement rate. All three filters produce nearly identical results at

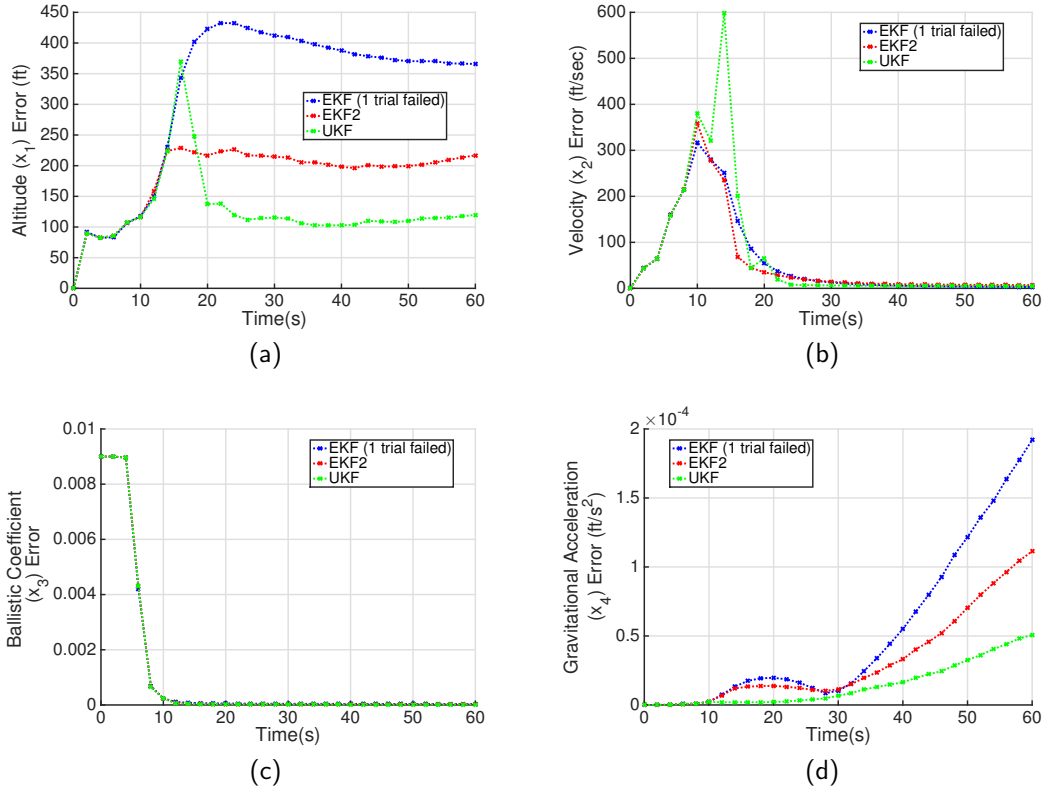

Figure 2.5. Comparison of EKF, EKF2, UKF estimation performance at 0.5Hz measurements, 100 trial average: (a) depicts average absolute altitude, x_1, error, (b) average absolute velocity, x_2, error, (c) average absolute ballistic coefficient, x_3, error and (d) average absolute gravitational acceleration, x_4, error.

a measurement frequency of 5Hz. These results suggest that when the measurement frequency is *sufficiently fast*, the different EKF and UKF approximation techniques do not impact estimator performance.

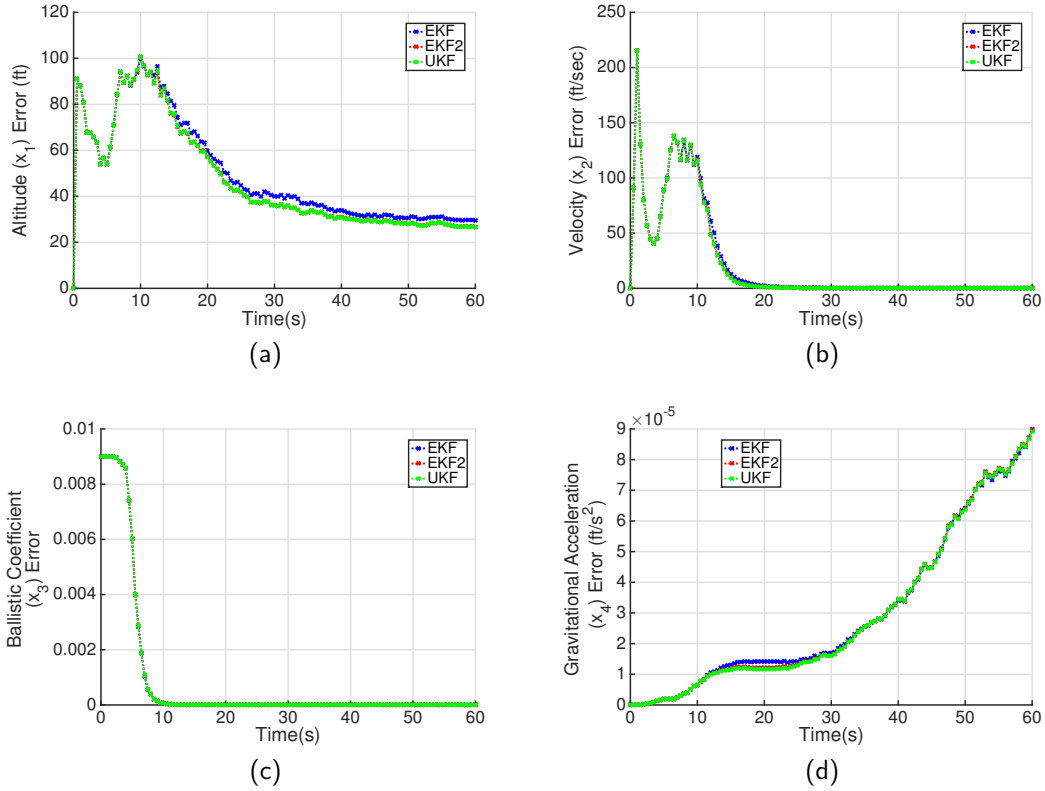

Figure 2.6. Comparison of EKF, EKF2, UKF estimation performance at 2Hz measurements, 100 trial average: (a) depicts average absolute altitude, x_1, error, (b) average absolute velocity, x_2, error, (c) average absolute ballistic coefficient, x_3, error and (d) average absolute gravitational acceleration, x_4, error.

2.3.1 Measurement Frequency Greater Than or Equal 0.5 Hz

More detailed results from this study are presented in Figures 2.7 - 2.9 for the EKF, EKF2, and UKF, respectively. These plots highlight the effect of measurement frequency on estimator performance. The three-dimensional and two-dimensional views show the same 100 trial average absolute altitude estimation error. The plots are produced by calculating the average absolute error using measurement frequencies of 0.5 Hz - 1 Hz at 0.1 Hz intervals and 2 Hz and interpolating. Both views are presented and the axes and color bars are identical to facilitate comparison between the three filters. For this particular problem, measurement rates in excess of 1.5 Hz produce negligible differences between these nonlinear estimation techniques.

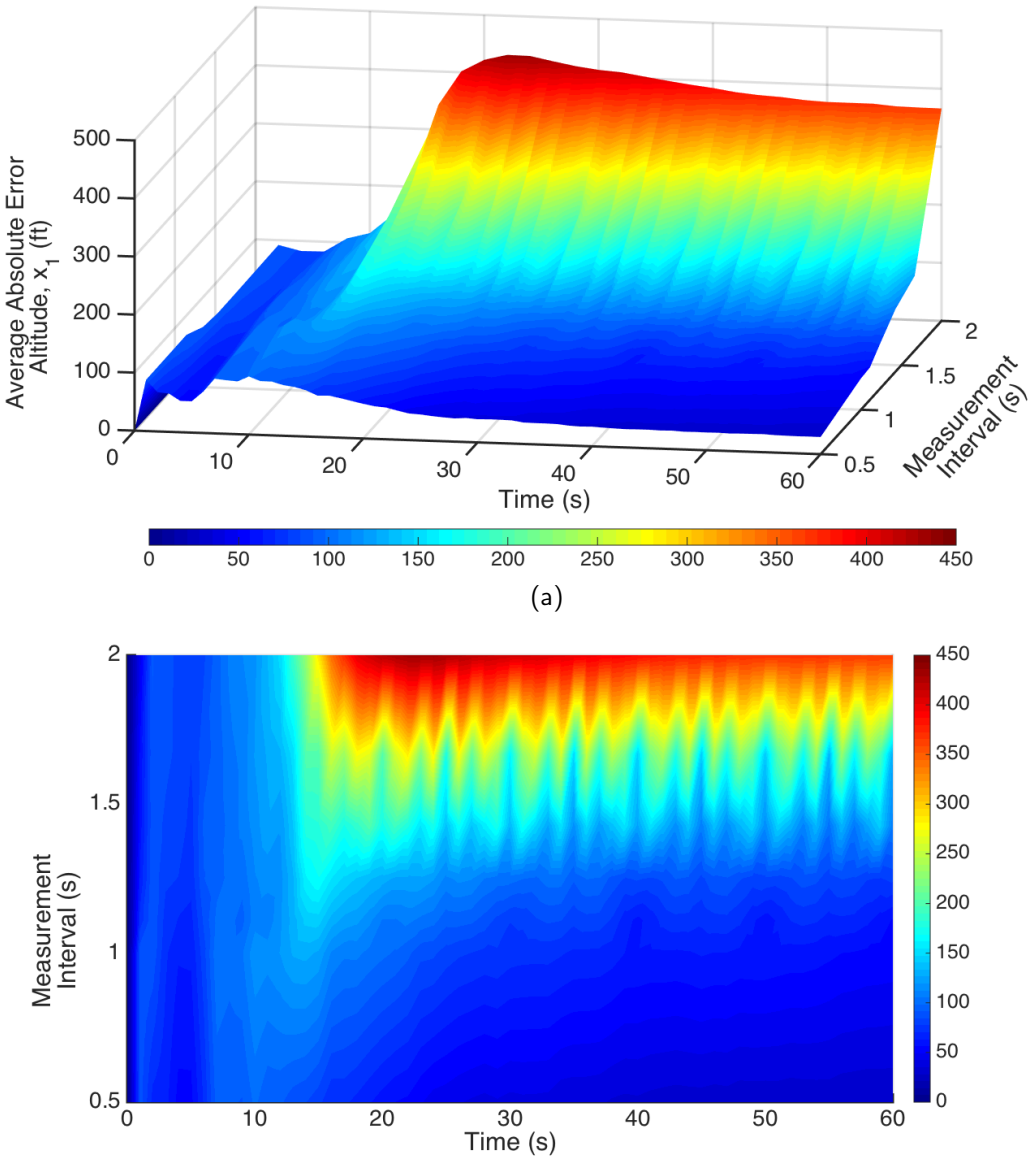

Figure 2.7. EKF, average absolute altitude, x_1, error, 100 trial average, with measurement interval of 0.5 s and 2 s (measurement frequency of 2 Hz and 0.5 Hz): (a) depicts time versus measurement interval versus error and (b) time versus measurement interval.

Comparison of the three KF–based nonlinear estimators reveals that the sensitivity to measurement frequency is reduced through use of a "more accurate" [11] approximation tech-

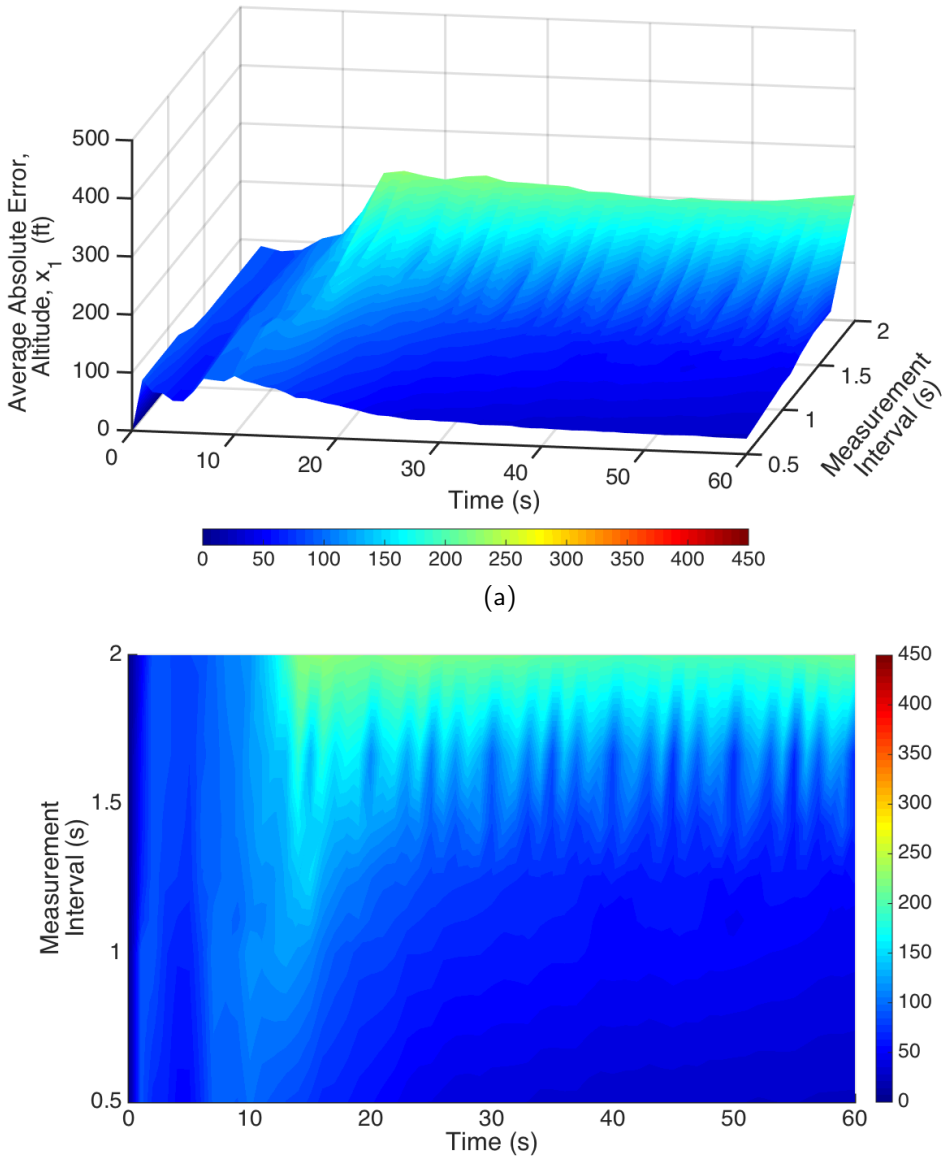

Figure 2.8. EKF2, average absolute altitude, x_1, error, 100 trial average, with measurement interval of 0.5 s and 2 s (measurement frequency of 2 Hz and 0.5 Hz): (a) depicts time versus measurement interval versus error and (b) time versus measurement interval.

nique. However, both the EKF and EKF2 reject information available in the measurements $t = 15$ s as a result of underestimated state covariance.

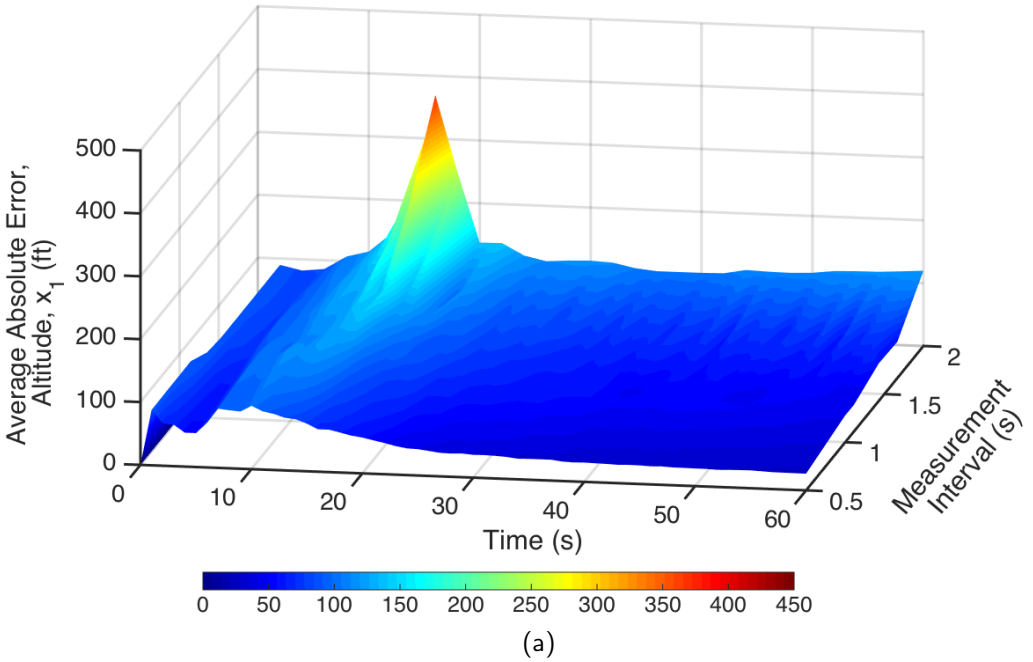

(a)

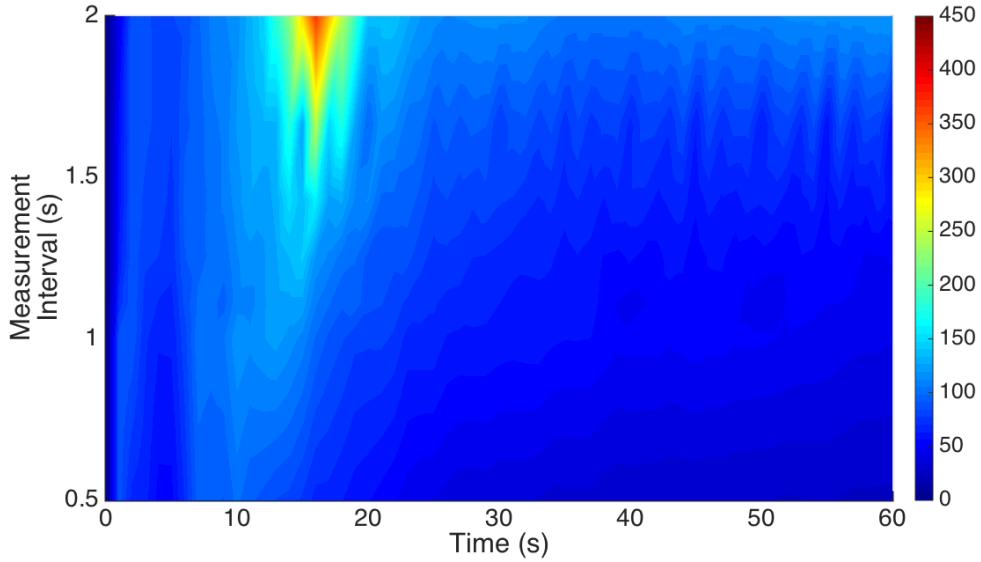

(b)

Figure 2.9. UKF, average absolute altitude, x_1, error, 100 trial average, with measurement interval of 0.5 s and 2 s (measurement frequency of 2 Hz and 0.5 Hz): (a) depicts time versus measurement interval versus error and (b) time versus measurement interval.

2.3.2 A Priori Covariance Estimation

KF–based nonlinear estimators fundamentally differ in the estimation of the *a priori* covariance. As discussed in Section 1.2.3, an accurately propagated covariance is a fundamental assumption in the KF optimal gain selection. The estimators will improperly exclude information available in the measurement if the *a priori* covariance is underestimated. The effect of measurement frequency on the *a priori* covariance estimates can be seen by comparing Figures 2.10 and 2.11.

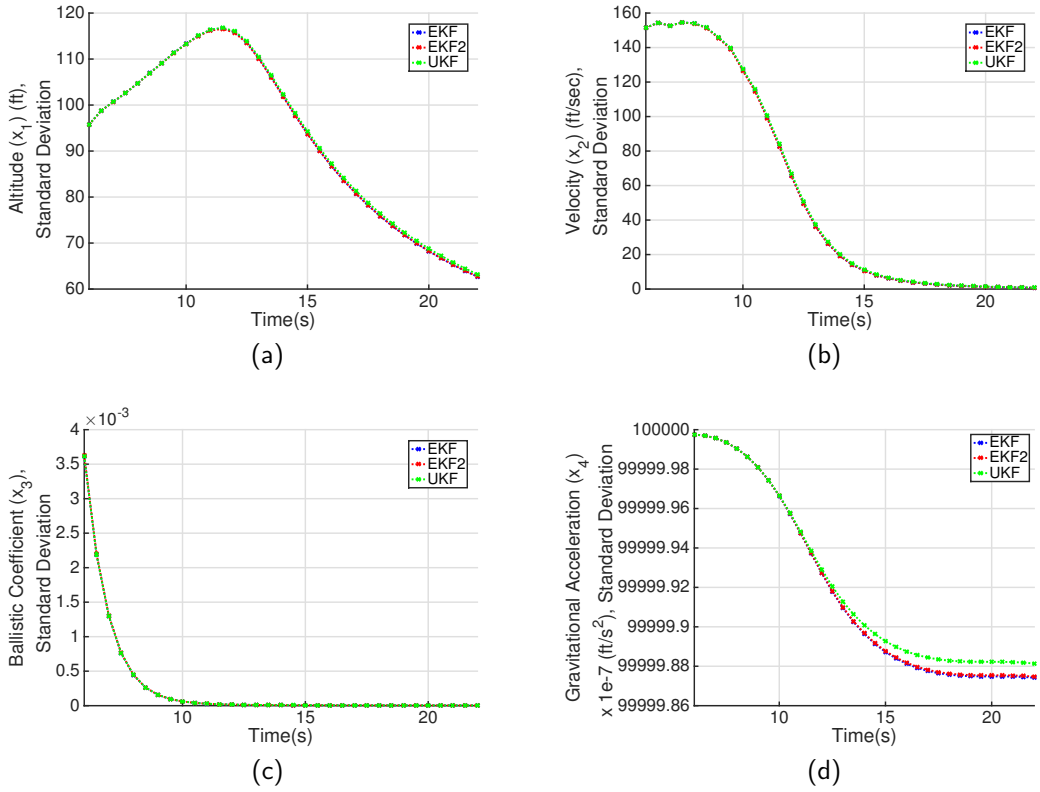

Figure 2.10. Comparison of estimated standard deviation, 100 trial average, 2 Hz measurements: (a) depicts average estimated altitude (x_1) standard deviation, (b) average estimated velocity (x_2) standard deviation, (c) average estimated ballistic coefficient (x_3) standard deviation and (d) average estimated gravitational acceleration (x_4) standard deviation.

The time between $t = 6$ s and $t = 22$ s, the region where the nonlinear effect is most prominent as discussed in Section 2.2 is shown in these figures. The standard deviation associated with each state as estimated by the EKF and EKF2 is smaller than the UKF

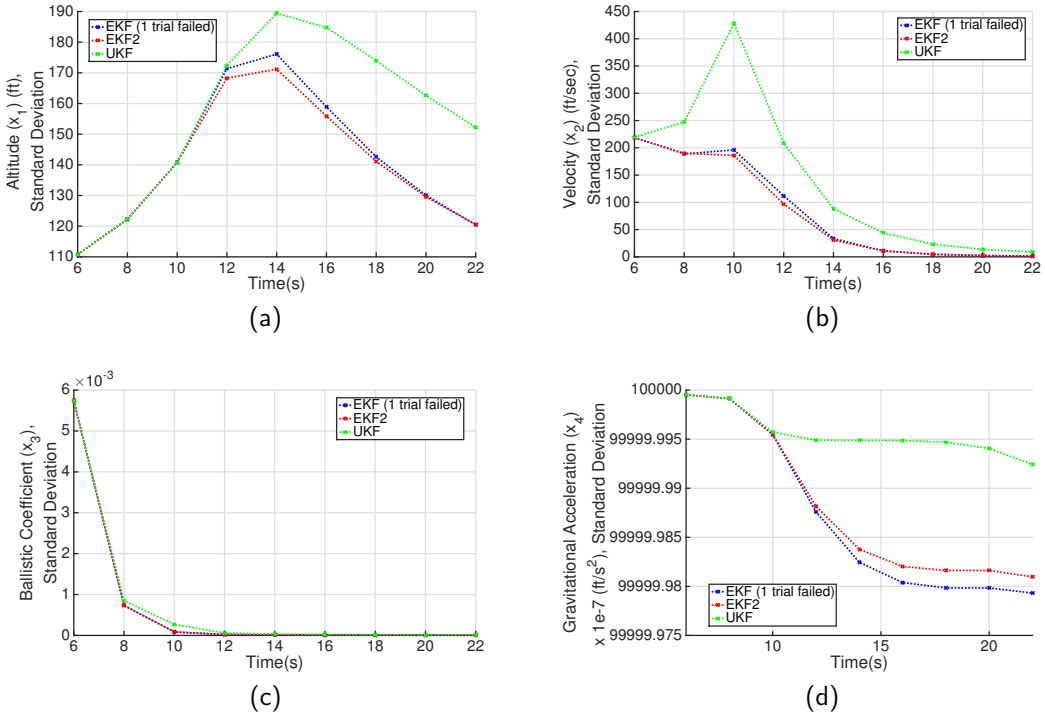

Figure 2.11. Comparison of estimated standard deviation, 100 trial average, 0.5 Hz measurements: (a) depicts average estimated altitude (x_1) standard deviation, (b) average estimated velocity (x_2) standard deviation, (c) average estimated ballistic coefficient (x_3) standard deviation and (d) average estimated gravitational acceleration (x_4) standard deviation.

estimate at 0.5 Hz. The underestimated covariance results in the filter lowering the weight placed upon the innovation; the EKF weights the prediction more than the measurement as a result of underestimating the propagated uncertainty. Julier and Uhlmann [12] note that a consistent covariance estimate, as defined in Equation (2.6), is necessary for filter convergence.

$$P_k^- - \mathbb{E}[(x_k - \bar{x}_k)(x_k - \bar{x}_k)^T] \geq 0 \tag{2.6}$$

The actual *a priori* covariance in Equation (2.6) results from $\mathbb{E}[(x_k - \bar{x}_k)(x_k - \bar{x}_k)^T]$, where x_k is the actual vice estimated state and $\bar{x}_k$ is the actual mean of the state. An optimal estimator requires $P_k^- = \mathbb{E}[(x_k - \bar{x}_k)(x_k - \bar{x}_k)^T]$.

At higher frequencies, as shown in Figure 2.10, the EKF, EKF2, and UKF generate nearly identical *a priori* standard deviation estimates for each state. This results in nearly identical

estimation performance at the 2 Hz measurement frequency seen in Figure 2.6.

2.3.3 Kalman Gain

Information obtained through each measurement is incorporated into the propagated state estimate by weighting the innovation with the Kalman gain, as shown in Equation (1.11). The Kalman gain is calculated for the EKF and the EKF2, as shown in Equations (1.33) and (1.38), respectively. The UKF Kalman gain is calculated, as shown in Equation (1.44). The Kalman gain should become small as the filter converges in steady state since there will be limited new information available in each innovation.

The effect of measurement frequency on the average Kalman gain associated with the altitude, x_1, and velocity, x_2 state estimates at 2 Hz, 1 Hz, and 0.5 Hz is shown for the EKF, EKF2, and UKF in Figure 2.12, Figure 2.13, and Figure 2.14, respectively. Ballistic coefficient, x_3, and gravitational acceleration, x_4, are not shown due to the very small Kalman gain magnitude differences.

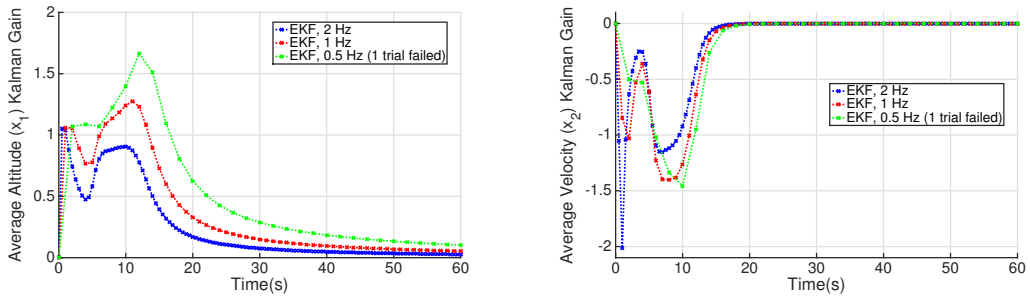

Figure 2.12. Comparison of EKF Kalman gain, 100 trial average, at varied measurement frequency: (a) depicts average altitude (x_1) Kalman gain and (b) average velocity (x_2) Kalman gain.

The estimated *a priori* covariance, P_k^-, the uncertainty associated with the state estimate, is approximated using different techniques in each approach, as discussed in Section 1.2. This can result in a covariance matrix that does not reflect the true uncertainty in the state, as seen in Figure 2.11. The Kalman gain is calculated for the EKF, as shown in Equation (2.7), for this particular problem. $P_{k,ij}^-$ is the *a priori* estimated covariance component with indices i

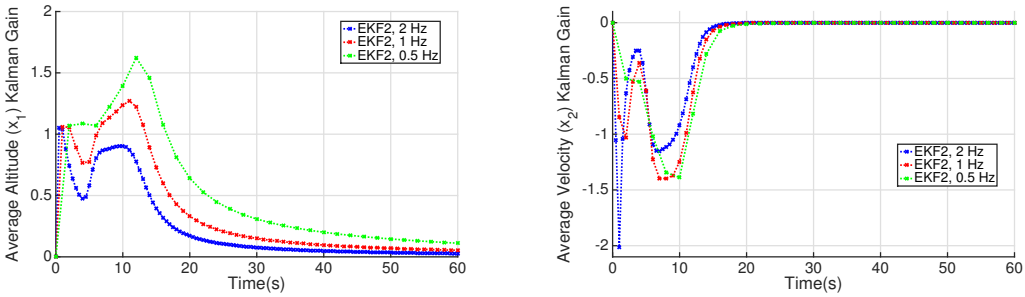

(a) (b)

Figure 2.13. Comparison of EKF2 Kalman gain, 100 trial average, at varied measurement frequency: (a) depicts average altitude (x_1) Kalman gain and (b) average velocity (x_2) Kalman gain.

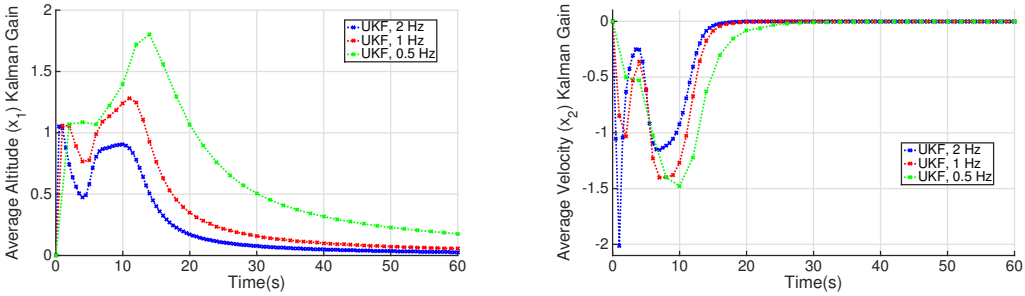

(a) (b)

Figure 2.14. Comparison of UKF Kalman gain, 100 trial average, at varied measurement frequency: (a) depicts average altitude (x_1) Kalman gain and (b) average velocity (x_2) Kalman gain.

and j. $H_{k,ij}$ is the measurement Jacobian at time, k, with indices i and j.

$$K_k = \begin{bmatrix} P^-_{k,11} H_{k,11} \\ P^-_{k,21} H_{k,11} \\ P^-_{k,31} H_{k,11} \\ P^-_{k,41} H_{k,11} \end{bmatrix} \cdot \left(\frac{1}{H_{k,11} P^-_{k,11} H_{k,11} + R_k} \right) \tag{2.7}$$

The value of $H_{k,11}$ will vary depending on the estimated altitude, as shown in Figure 2.15. The value of the measurement Jacobian will scale each state's Kalman gain, as shown in Equation (2.8). The measurement noise, R_k, will have a greater relative effect on the

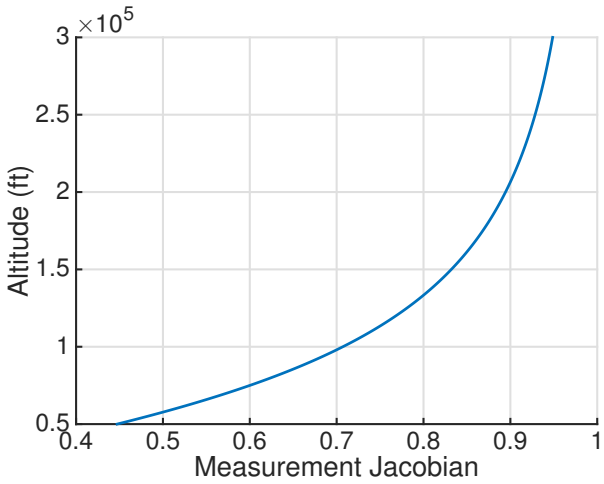

Figure 2.15. Measurement Jacobian (H_{11}) value versus altitude, falling body problem

Kalman gain in comparison with the estimated covariance as altitude decreases.

$$\left(\frac{1}{P_{k,11}^{-} H_{k,11} + \frac{R_k}{H_{k,11}}} \right) \tag{2.8}$$

Comparison between the EKF, EKF2 and UKF 100 trial average Kalman gain magnitude at 2 Hz measurement frequency reveals a similar weighting profile between all approaches, shown in Figure 2.16a. Comparison of the average Kalman gain magnitude at 0.5 Hz measurement frequency reveals a significantly larger weighting for the UKF, as shown in Figure 2.16c. Figure 2.16b is provided for comparison as the common measurement frequency used in the literature. This difference in average magnitude of the Kalman gain in Figure 2.16c results in the UKF incorporating more information from measurements compared to the EKF and EKF2. The plots provided in this section highlight that the EKF and EKF2 are converging, on average, earlier in time than the UKF. Unfortunately, this convergence prevents incorporation of valuable information in the measurements. The Kalman gain difference results in the UKF's reduced steady state convergence error in comparison to the EKF and EKF2.

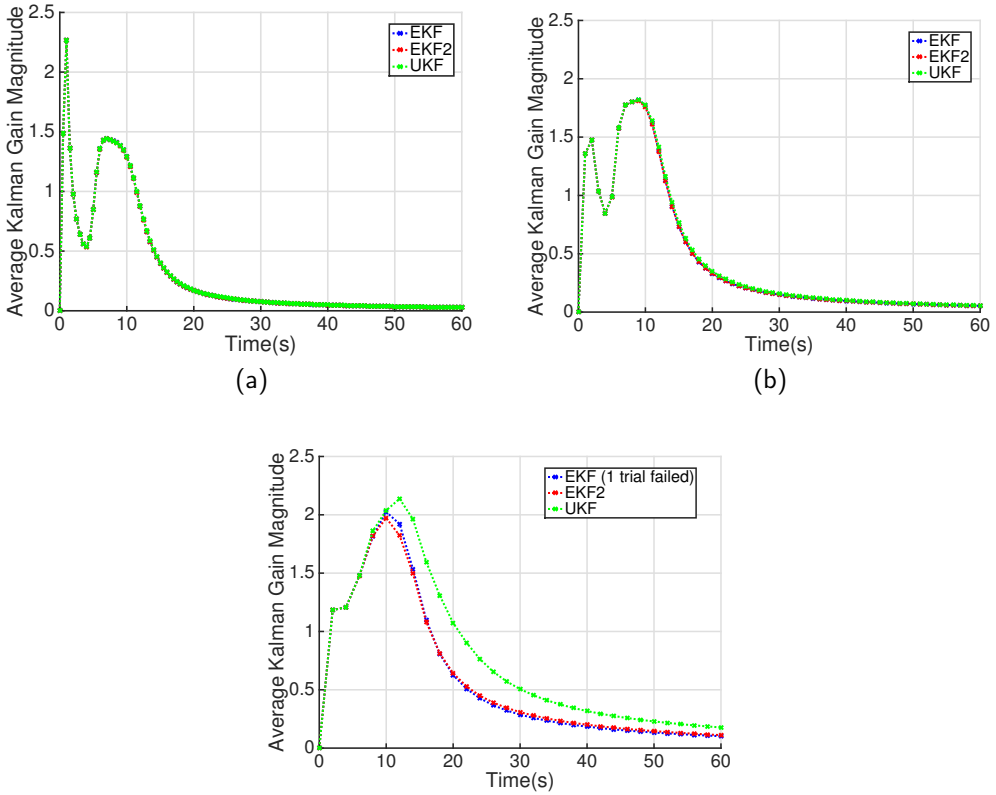

Figure 2.16. Comparison of EKF, EKF2 and UKF average Kalman gain magnitude, 100 trial average, at varied measurement frequencies: (a) depicts average Kalman gain magnitude, 2 Hz measurements, (b) average Kalman gain magnitude, 1 Hz measurements and (c) average Kalman gain magnitude, 0.5 Hz measurements.

2.3.4 Innovations

Additional insight is obtained by considering the innovation, or residuals, $Res(t_k)$, as shown in Equation (2.9).

$$\begin{aligned} Res(t_k) &= \tilde{y}_k - \hat{y}_k \\ &= \tilde{y}_k - h(\hat{x}_{t_k}^-) \\ &= (r(t_k) + v(t_k)) - \sqrt{M^2 + (\hat{x}_1(t_k) - H)^2} \end{aligned} \tag{2.9}$$

The actual radar range at any specified time is a function of the actual state value, as shown in Equation (2.4). The estimated state, $\hat{x}_1(t_k)$, is the actual value of the state, $x_1(t_k)$, plus the error between it and the actual value, $\tilde{x}_1(t_k) = \hat{x}_1(t_k) - x_1(t_k)$. Therefore, the residual can be rewritten, as shown in Equation (2.10).

$$\begin{aligned} Res(t_k) &= \left(\sqrt{M^2 + x_1(t_k)^2} + v(t_k) \right) - \sqrt{M^2 + (x_1(t_k) + \tilde{x}_1(t_k))^2} \\ &= v(t_k) + \left(\sqrt{M^2 + x_1(t_k)^2} - \sqrt{M^2 + x_1(t_k)^2 + 2x_1(t_k)\tilde{x}_1(t_k) + \tilde{x}_1(t_k)^2} \right) \end{aligned} \tag{2.10}$$

The residual will become $v(t_k)$ as $\tilde{x}_1 \to 0$. Maybeck [8] notes that the residual sequence has been shown to be white, and Gaussian for the linear filter. The residual sequence can be monitored to determine if the filter is performing properly. Maybeck also notes that a moving window is the most appropriate way of considering filter performance, as a single large residual does not indicate filter failure. When the filter is performing correctly in steady state, the innovations over time should reflect the noise associated with the measurement.

This approach seeks to determine if the innovation sequence demonstrates a bias or a process strength increase. In other words, the innovations are expected to exhibit a noise profile similar to that shown in Figure 2.3b. Figure 2.17 shows the innovations generated when using the same representative single trial by the EKF, EKF2 and UKF at two different frequencies. As the measurement interval is lengthened, the EKF, EKF2, and UKF innovations appear representative of the measurement noise for this trial.

The 100 trial average innovation for each filter at a given measurement frequency characterizes the filter performance. The average innovation, $\overline{Res}$, is shown in Equation (2.11) and is the expectation of the residual, Equation (2.10).

$$\begin{aligned} \overline{Res} &= \tfrac{1}{N} \sum_{i=1}^{N} Res_i(t_k) \text{ for } k = 0, \Delta t, 2\Delta t, \ldots, t_f \\ \overline{Res}(t_k) &= \mathbb{E}\left[v(t_k) + \left(\sqrt{M^2 + x_1(t_k)^2} - \sqrt{M^2 + x_1(t_k)^2 + 2x_1(t_k)\tilde{x}_1(t_k) + \tilde{x}_1(t_k)^2} \right) \right] \\ &= \mathbb{E}\left[\sqrt{M^2 + x_1(t_k)^2} \right] - \mathbb{E}\left[\sqrt{M^2 + x_1(t_k)^2 + 2x_1(t_k)\tilde{x}_1(t_k) + \tilde{x}_1(t_k)^2} \right] \end{aligned} \tag{2.11}$$

The average residual should disappear as $\tilde{x}_1 \to 0$, as shown in Figure 2.18a. All filters

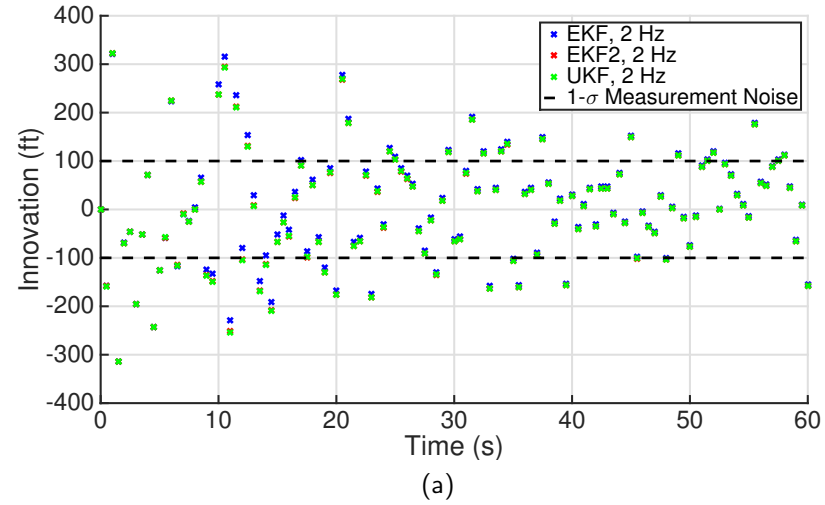

(a)

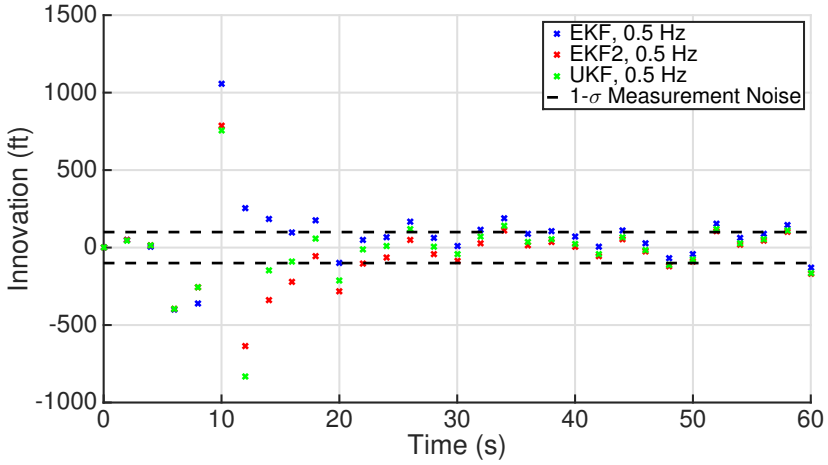

(b)

Figure 2.17. Comparison of EKF, EKF2 and UKF innovations from a single trial: (a) depicts 2 Hz measurements and (b) 0.5 Hz measurements.

display a process model error, as seen in Figure 2.18, during the first 10 seconds since the filter has not yet corrected the error from the ballistic coefficient, x_3, initialization.

Non-random filter error will appear as a deviation from 0, as visible in Figure 2.18b most clearly for the EKF. The effect of measurement frequency of filter performance is clearly seen by comparing the average innovations shown in Figures 2.18a and 2.18c that have the same axes.

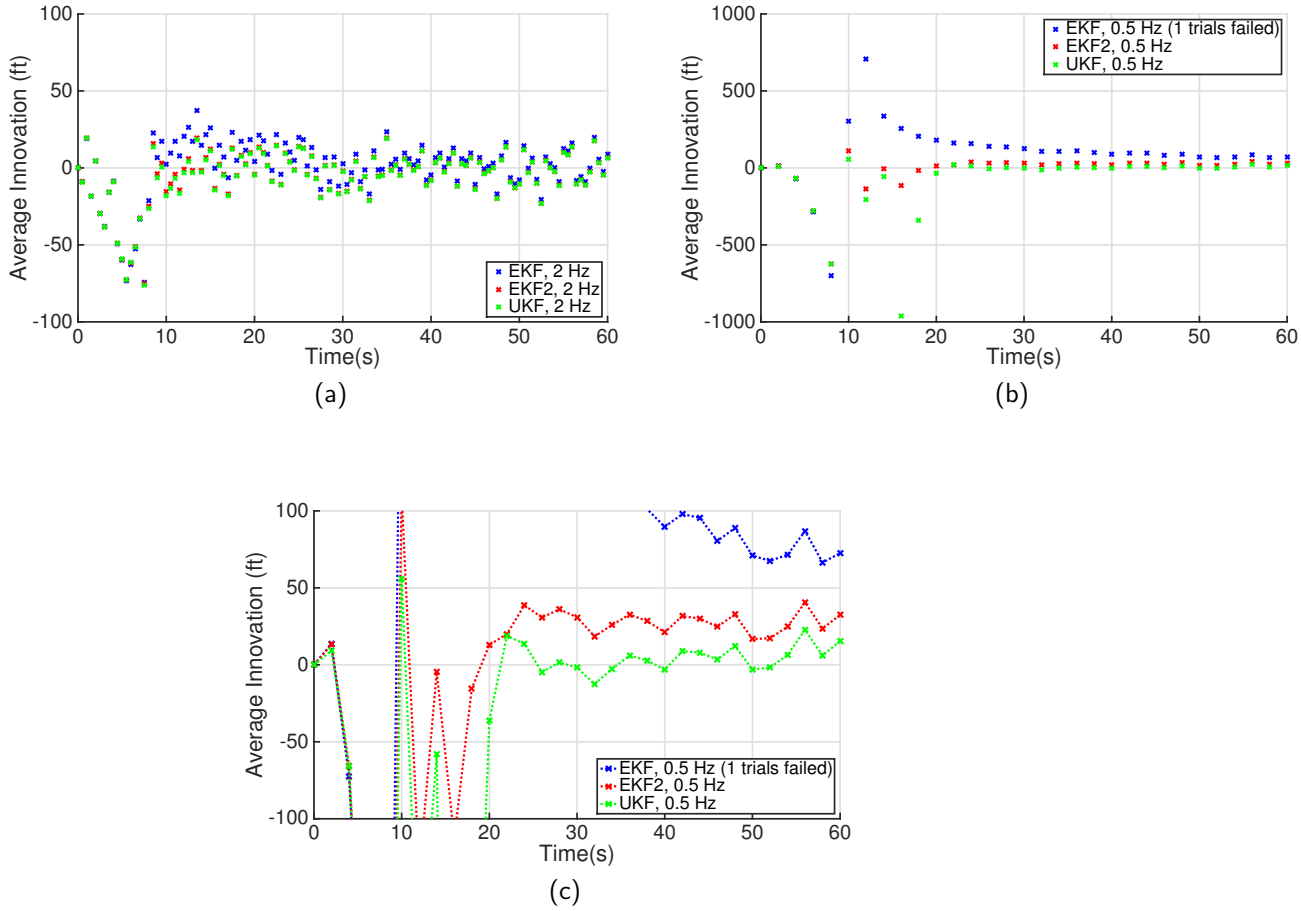

Figure 2.18. Comparison of EKF, EKF2 and UKF 100 trial average innovations: (a) depicts 2 Hz measurements, (b) 0.5 Hz measurements and (c) an expanded view at 0.5 Hz measurements.

2.3.5 Measurement Frequency Less Than 0.5 Hz

Further lowering measurement frequency produces the unexpected results shown in Figure 2.19 —failed UKF execution occurring in conjunction with the partially successful EKF execution. Figure 2.19 reveals that the three filters are unable to converge to a stable steady-state average absolute error. Although the UKF shows better performance than the EKF2 at the 0.5 Hz measurement frequency, as shown in Figure 2.5, the UKF is unable to complete any of the 100 trials at the 0.3 Hz measurement rate. The EKF fails to execute on 75% of the trials and does not converge when it executes. The EKF2 diverges in all cases,

but is able to run for the full simulation duration.

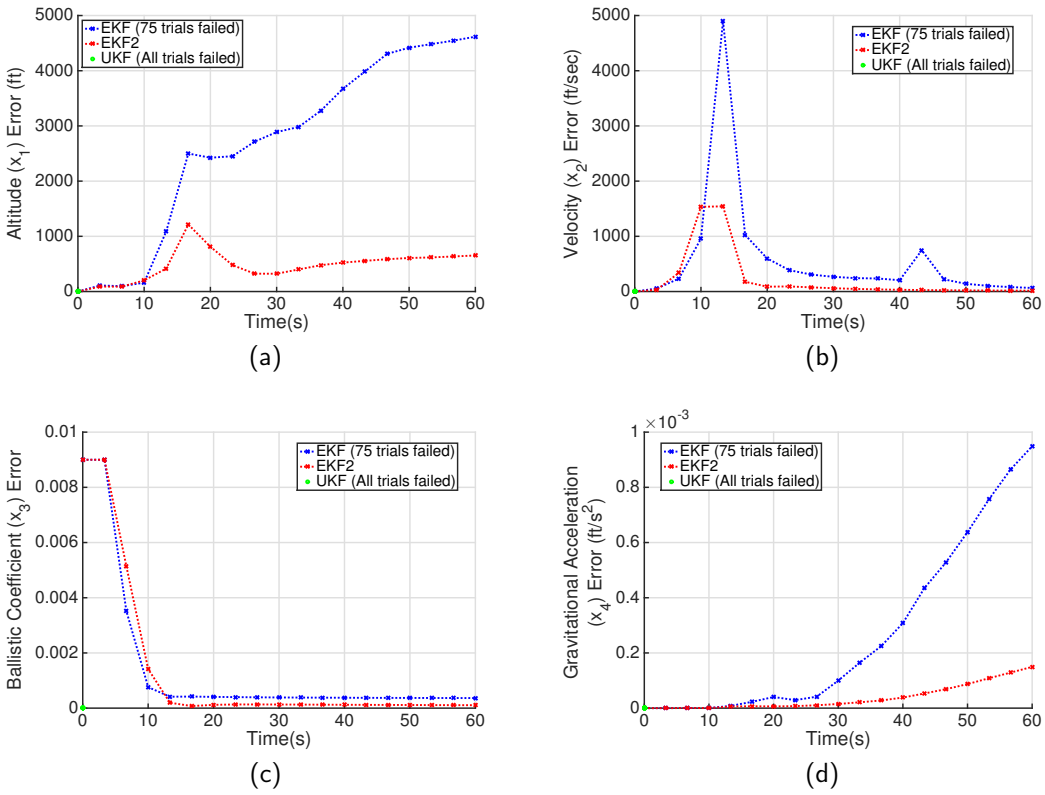

Figure 2.19. Comparison of EKF, EKF2, UKF estimation performance at 0.3Hz measurement frequency, 100 trial average: (a) depicts average absolute altitude (x_1) error, (b) average absolute velocity (x_2) error, (c) average absolute ballistic coefficient (x_3) error and (d) average absolute gravitational acceleration (x_4) error.

This unanticipated result requires a more detailed investigation of each UKF trial to find the cause for the performance failures. Close inspection reveals velocity, x_2, approaches positive infinity in each trial. The object accelerates toward the surface at an increasing rate rather than decelerating as anticipated. This condition is not physically possible given the problem construct shown in Figure 2.1. The acceleration, $\dot{x}_2$, can increase downward only if the ballistic coefficient, x_3, is negative, as shown in Equation (2.2). However, Equation (2.3) demonstrates that x_3 must be positive by definition. This constraint violation suggests a need to consider the individual sigma point vectors that are propagated through the dynamic model between discrete measurements.

Each state has physical limits in this particular problem. Altitude, like the ballistic coefficient, must remain positive since the resistance to the body's motion would be significantly higher below the surface than through the modeled atmosphere. Velocity and the gravitational acceleration both have minimum and maximum physical limits. Velocity magnitude is limited by the physical characteristics of the body, as high speed may lead to disintegration. Similarly, the gravitational acceleration is limited in magnitude. Close inspection of the initial sigma points at $t = 0$, as shown in Table 2.1, reveals that in one instance the ballistic coefficient, or β, x_3 has a negative value. These sigma points are generated using the extended symmetric approach detailed in Section 1.2.4, assuming filter initialization parameters of Section 2.2.

Table 2.1. Falling body example of Section 2.2 initial $2n + 1$ sigma points.

Sigma Points (2n+1)	1	2	3	4	5	6	7	8	9
Weight	0	0.125	0.125	0.125	0.125	0.125	0.125	0.125	0.125
Altitude, x_1 (ft)	300000	302000	300000	300000	300000	298000	300000	300000	300000
Velocity, x_2 (ft/s)	20000	20000	24000	20000	20000	20000	16000	20000	20000
β, x_3 (1/ft)	0.01	0.01	0.01	0.03	0.01	0.01	0.01	-0.01	0.01
g, x_4 (ft/s^2)	32.17405	32.17405	32.17405	32.17405	32.19405	32.17405	32.17405	32.17405	32.15405

Figure 2.20 shows propagation divergence of a single initial sigma point, point number 8 from Table 2.1, violating the state constraints. The divergence occurs after a propagation time longer than 8 seconds, a period of time greatly in excess of the 1 second propagation that occurs for the literature standard 1Hz measurement frequency. However, propagation of this point impacts the *a priori* mean and covariance over any interval; a longer interval makes the physical error's effect more pronounced. Although this initial condition is not the exact cause for the filter divergence seen in Figure 2.19[8], it reveals the fundamental challenge of applying the UKF to physical problems subject to state constraints. The remainder of this chapter will investigate use of the UKF with inequality constraints to allow for extending the time interval between measurements (i.e., extending the maximum measurement interval in excess of 0.5Hz measurement frequency in the falling body problem). Any UKF application with implicitly constrained states may benefit from this analysis.

Julier and Uhlmann [11], [12] noted that the UKF algorithm "naturally lends itself to being used in a 'black box' filtering library." "Appropriately defined inputs and outputs" [11]

[8]Divergence occurs later in the state trajectory.

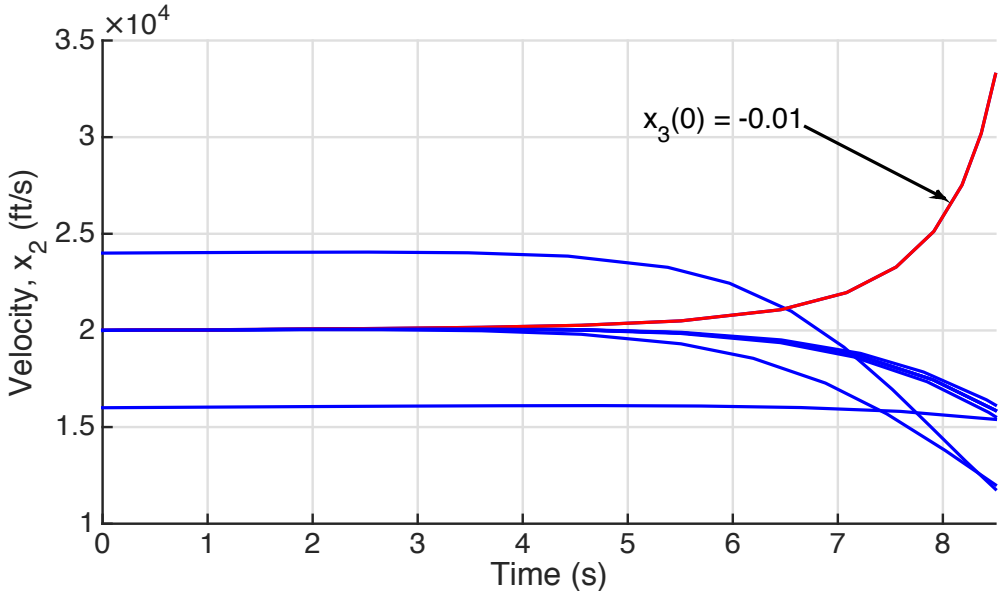

Figure 2.20. Initial sigma point propagation, falling body problem

are necessary, but the UKF algorithm does not enforce state constraints. The effect of a sigma point that contains state values outside of physical limits is not readily apparent in many applications. Relatively short measurement intervals limit the likelihood that a single sigma point violating physical constraints will overwhelm the other sigma points that satisfy the constraints. However, the post-transformation statistics are impacted for even short measurement intervals. The nonlinear function's nature is a significant factor in determining the magnitude of the effect. The magnitude of the estimated velocity that results from integration of the process model in the falling body example is the cause of the UKF failure.

Background on constrained UKF implementation is provided in the following section. Section 2.5 details a novel approach to satisfy state constraints through application of the scaled UT [34] to lengthen the measurement interval. Section 2.5.4 and Section 3.1 demonstrate the UKF-S on the falling body problem and the pendulum problem, respectively.

2.4 Constrained UKF Background

The UKF is known to be a suboptimal estimation technique that approximates the minimum mean square estimate [11]. For this reason, Simon [38] notes, "if there are additional

constraints beyond those explicitly stated in the system model, then the complete system description is different than that assumed by the standard Kalman filter equations," that the KF–based nonlinear estimation techniques may benefit from incorporating constraints. The literature provides methods to enforce both equality and inequality constraints. The following sections describe different approaches to the inequality constrained UKFs in the literature.

Teixeira et al. [39] note that the challenge of incorporating restraints arises in many nonlinear estimation problems but is an intractable challenge for linear systems, as well. Inequality constraints are inherently violated by assuming Gaussian noise in the filter construct [39]. This has led to the development of approximate techniques that seek to produce a state estimate respecting the known constraints. Simon's survey paper [38] presents three approaches; these methods involve projecting the estimate onto the constraints, truncating the PDF, or using a MHE approach involving formulation of a non-recursive constrained quadratic program. Many variations exist into the timing, either *a priori* or *a posteriori*, for applying the first two techniques on sigma points, as discussed in the following sections [38]. One common theme among these approaches is that the estimated mean or the estimated mean and covariance are changed, if necessary, to satisfy the inequality constraints.

2.4.1 Projection

The unconstrained estimate, $\hat{x}_k^+$, results from the application of the KF structure, which does not consider limitations on possible state values. State constraints effectively limit the potential region where the estimate may lie. Therefore, one approach to finding a constrained estimate, $\hat{x}_{k,con}^+$, is to find the minimum constrained estimate that satisfies the constraints as shown in Equation (2.12) [9].

$$\hat{x}_{k,con}^+ = \underset{\hat{x}_{k,con}^+}{\operatorname{argmin}} (\hat{x}_{k,con}^+ - \hat{x})^T W (\hat{x}_{k,con}^+ - \hat{x}) \text{ s.t. } Dx_{con} \leq d \tag{2.12}$$

W is a positive definite weighting matrix that can be selected based on the desired constrained estimate. Equation (2.12) projects the unconstrained estimate into the constrained space. Simon [9] notes that setting W to the identity matrix, I, produces the least mean square constrained estimate. Furthermore, setting W to the inverse of the covariance ma-

trix, P_k^{-1}, produces the minimum variance estimate [9]. The resulting quadratic programming problem seeks to minimize the weighted squared difference between the constrained and unconstrained estimates [9].

Teixeira et al. [39] present the sigma-point interval unscented Kalman filter (SIUKF) as a construct based on the interval unscented Kalman filter (IUKF).[9] This approach uses sigma points that do not violate the state's inequality constraints. This condition is achieved by projecting any violating sigma points onto the constraints as shown geometrically in Figure 2.21. Teixeira et al. [39] note that the sigma points "weighted sample mean and covari-

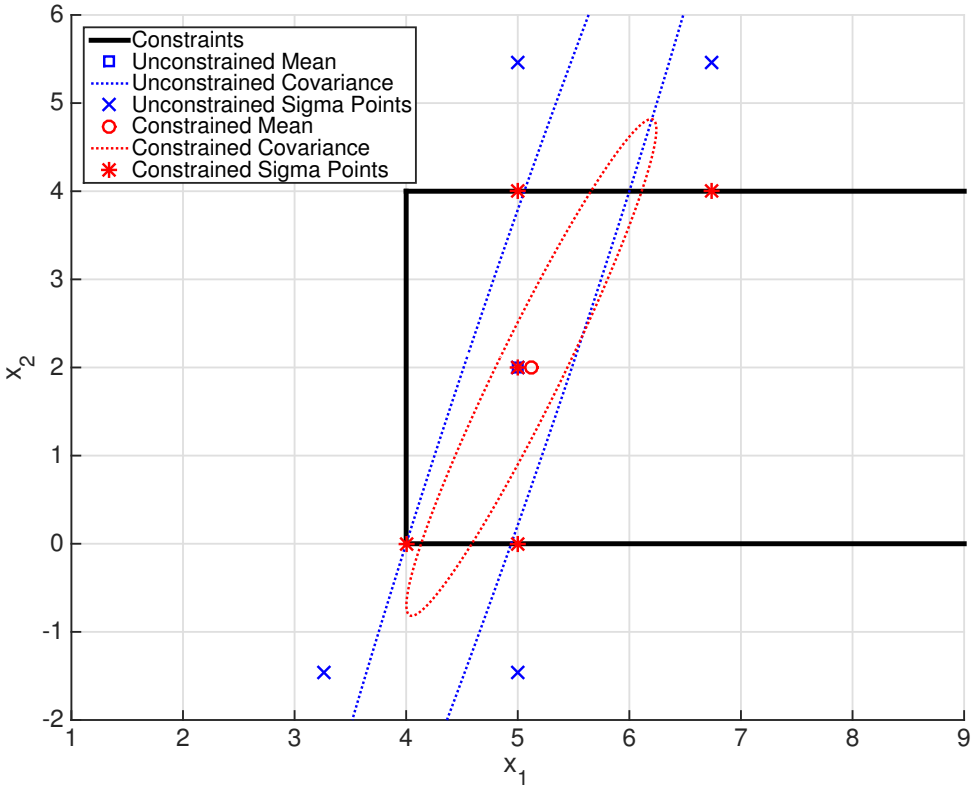

Figure 2.21. Projected sigma points for the mean and covariance shown in Table 2.2

ance may not capture" the *a priori* mean and covariance. This effect is clearly visible in

[9]The IUKF is Teixeira et al.'s name for the sigma point selection approach used in Vachhani et al.'s unscented recursive nonlinear dynamic data reconciliation (URNDDR) detailed in this section [39], [40].

Figure 2.21. Inequality constraints are enforced on individual sigma points at both the prediction and update steps of the UKF algorithm. Other authors [41], [42] proposed similar projection approaches to constrain sigma points.

Teixeira et al. also present the constrained unscented Kalman filter (CUKF) in [39] that combines a normal UT prediction step while enforcing the inequality constraints only on the mean during the update step. The error covariance is not constrained in this algorithm. The constrained interval unscented Kalman filter (CIUKF) uses the prediction step of the SIUKF coupled with the update step of the CUKF [39]. The IUKF uses the prediction step of the SIUKF and CIUKF coupled with the UKF update step [39].

Vachhani et al. [40] present the URNDDR to incorporate constraints on sigma points prior to propagation. This method generates sigma point vectors that are asymmetric and alters the associated weights to account for the asymmetry. Vachhani et al. [40] note that the sigma point vectors of Julier and Uhlmann's extended symmetric set have components that lie a distance of $\sqrt{n+\kappa}$ in the direction $\pm\sqrt{P_{k|k}}$. The URNDDR instead employs sigma point vectors that have components in the same direction, $\pm\sqrt{P_{k|k}}$, but at a different distance, as calculated in Equation (2.13) [40].

$$\begin{aligned} \theta_{ik} &= \min(\sqrt{n+\kappa}, \theta_{1k}, \theta_{2k}) \\ \theta_{1k} &= \min_{j:s_{i,j}>0}(\infty, \chi_{U,j} - \hat{x}_{k|k,j}) \\ \theta_{2k} &= \min_{j:s_{i,j}<0}(\infty, \chi_{L,j} - \hat{x}_{k|k,j}) \end{aligned} \tag{2.13}$$

The associated weights are calculated, as shown in Equation (2.14) [40].

$$\begin{aligned} W_i &= a\theta_i + b, \text{ where} \\ a &= \frac{2\kappa-1}{2(n+\kappa)(S_\theta-(2n+1)(\sqrt{n+\kappa}))} \\ b &= \frac{1}{2(n+\kappa)} - \frac{2\kappa-1}{2\sqrt{n+\kappa}(S_\theta-(2n+1)(\sqrt{n+\kappa}))} \\ S_\theta &= \sum_{i=1}^{2n}\theta_i \end{aligned} \tag{2.14}$$

These constrained sigma points are propagated forward in time, and a constrained optimization problem involving Equations (2.13) and (2.14) is solved for each sigma point.

Each resulting sigma point vector, $\chi_{k+1|k+1,i}$ contain components that satisfy all bounds. This ensures that the estimate is in the allowable region as required to generate the next time step's sigma points using the method shown in Equation (2.13) [40].

2.4.2 Truncated Probability Density Function

Details of implementing a constrained UKF using PDF truncation are found in [9]. This approach centers on the assumption that the PDF is known Gaussian. The estimated covariance matrix is transformed into a diagonal matrix so that constraints can be applied separately to each state. The unconstrained PDF is truncated at each states' constraint boundaries. The state estimate is the centroid of the truncated PDF. The inverse of the transformation is applied to the normalized covariance of the truncated PDF to produce the constrained estimated covariance [9]. This approach assumes that the PDF remains Gaussian despite nonlinear transformation and, therefore, may be subject to significant error.

Teixeira et al. [39] apply this approach to the UKF and IUKF as the truncated unscented Kalman filter (TUKF) and truncated interval unscented Kalman filter (TIUKF), respectively. These approaches are three-step estimators in that the prediction and update step are performed in the usual fashion. A third step, the truncation step, is included to determine the estimated state and covariance. The *a posteriori* mean and covariance are subjected to the inequality constraints such that a new constrained mean and covariance are determined if any constraint is violated [39]. The truncated mean and covariance are then used as the next time step *a priori* mean and covariance [39].

2.4.3 Moving Horizon Estimation

As noted in Chapter 1, the MHE was specifically developed to incorporate state constraints into nonlinear estimators [23]. This approach reformulates the estimator as an optimal control problem with constraints. The key insight was to limit the horizon over which optimization is required by accurately reflecting knowledge prior to the horizon as an arrival cost [23]. This approach cannot be employed with the KF structure.

2.5 Scaled UKF

This section investigates the new idea of using the Julier [34] sigma point scaling technique to achieve filter convergence over longer measurement intervals. The key insight leading to development of the UKF-S is that parameters are often constrained in model formulation. As a result, the improved model accuracy achieved through parameter estimation can be lost if sigma point vectors violate parameter constraints. Scaling is used to ensure that the *a posteriori* estimate and associated sigma points respect inequality constraints.

2.5.1 Scaled Unscented Transform Background

As the dimension of the state space increases, the radius of the hyper-sphere bounding the sigma points also increases. As a result of non local effects, transforms performed using the sigma point set will suffer in accuracy [34]. Julier et al. [43] proposed an approach to reduce the non local effects in the symmetric sigma point set presented in [13]. Julier [34] presents a more general approach, the scaled UT, to alter any sigma point set including the mean vector, $\chi_0 = \mu_x$.[10]. The scaled UT was proposed to minimize sigma point non local effects by reducing the sigma point vector bounding hyper-sphere radius while preserving the first two moments of the set.

Scaling is accomplished using a scale factor, $\alpha \in (0, 1]$, with an affine transformation of the sigma points shown in Equation (2.15).

$$\begin{aligned} \chi'_0 &= \chi_0 \\ \chi'_i &= \chi_0 + \alpha(\chi_i - \chi_0), i = 1, \ldots, 2n \\ W'_0 &= \frac{W_0}{\alpha^2} + (1 - \frac{1}{\alpha^2}) \\ W'_i &= \frac{W_i}{\alpha^2}, i = 1, \ldots, 2n \end{aligned} \tag{2.15}$$

When $\alpha = 1$ the scaled sigma point vectors and weights are equivalent to the unscaled sigma points. Julier [34] noted that, in addition to reducing non local effects, this technique allows for the incorporation of higher order information that can improve the accuracy of the unscented transformation.

[10] Any sigma point set can be extended by including the vector, $\chi_0 = \mu_x$ with $W_0 = \mathbf{0}$.

Figure 2.22 shows the effect of scaling the extended symmetric sigma point set representing, x, a representative two-dimensional Gaussian joint PDF with μ_x and P_x, as shown in Equation (2.16).

$$\mu_x = \begin{bmatrix} 5 \\ 2 \end{bmatrix} \qquad P_x = \begin{bmatrix} 1 & 2 \\ 2 & 8 \end{bmatrix} \tag{2.16}$$

A common scale factor, $\alpha \in \{1, 0.5, 0.1\}$, is applied to demonstrate the effect on sigma point vector location. The mean sigma point vector, χ_0, is not impacted by the scaling.

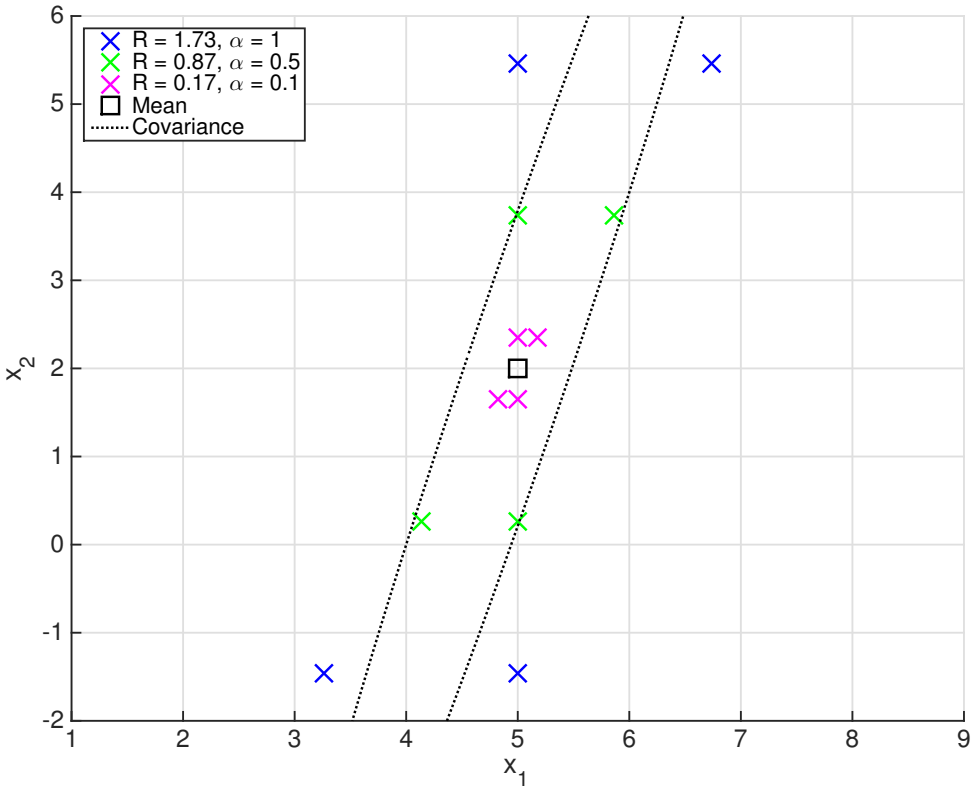

Figure 2.22. Comparison of scaling sigma points representing, x, a two-dimensional Gaussian joint PDF.

Careful inspection of Figure 2.22 reveals that the scaled sigma points are not equidistant about the mean, x_0, but rather are located $x_0 \pm \alpha * \sqrt{n+\kappa} * \sqrt{P}$, where $n = 2$ and $\kappa = 1$ in this example. The $\sqrt{P_x}$ provides the direction along which the bounding hyper-sphere radius, $R = \alpha * \sqrt{n+\kappa}$, extends.

Figure 2.23, when viewed in conjunction with Figure 2.21, shows a geometric representation of the difference between scaling and projecting sigma point vectors to satisfy constraints.

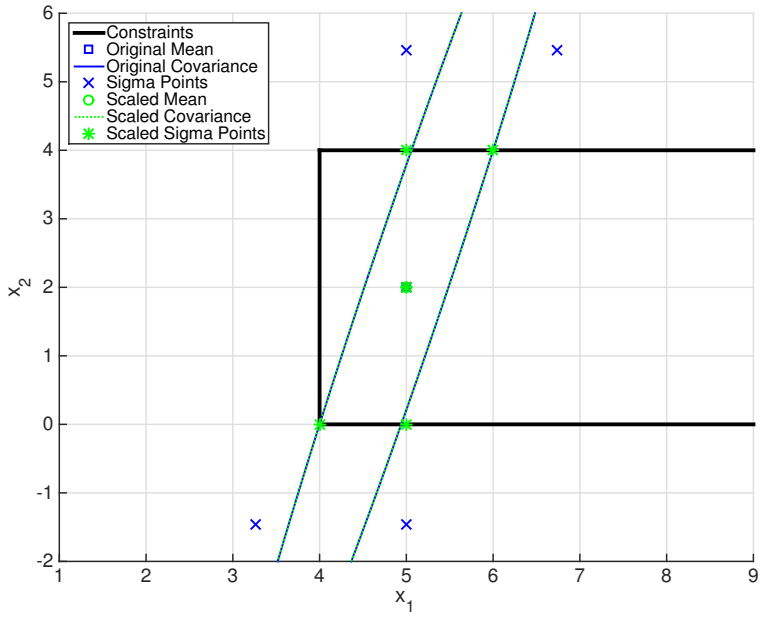

Figure 2.23. Scaled sigma points for the mean and covariance shown in Table 2.2

The projected sigma point vectors are moved over the shortest distance to the constraint boundaries, unlike the scaled sigma point vectors. Although this projection approach ensures that the sigma point vectors respect constraints, the represented first and second moments are altered, as shown in Table 2.2.

The scaled UT preserves the first and second moments of a sigma point set while reducing the radius of the hyper-sphere encompassing the sigma point vectors [34]. The scaled UT also preserves the third moment in this case and scales the fourth moment. Higher-order moments of the sigma point set are altered in exchange for reducing the hyper-sphere radius, as shown in Table 2.2. Since systems with nonlinear dynamic models do not necessarily maintain a Gaussian PDF throughout the entire state trajectory, the potential benefit of matching Gaussian third and higher order moments may be limited in comparison to the benefit of respecting constraints. The following section details an UKF that employs scaled

Table 2.2. Comparison of 2-dimensional example of projected (Figure 2.21) and scaled constrained (Figure 2.23) sigma points.

	1^{st} Moment	2^{nd} Moment	3^{rd} Moment	4^{th} Moment
Original	$\begin{bmatrix}5\\2\end{bmatrix}$	$\begin{bmatrix}1 & 2\\2 & 8\end{bmatrix}$	$\begin{bmatrix}0\\0\end{bmatrix}$	$\begin{bmatrix}15 & 30\\30 & 108\end{bmatrix}$
Constrained (Projected)	$\begin{bmatrix}5.1\\2.0\end{bmatrix}$	$\begin{bmatrix}0.65 & 0.91\\0.91 & 2.67\end{bmatrix}$	$\begin{bmatrix}0.62\\0.44\end{bmatrix}$	$\begin{bmatrix}3.97 & 5.50\\5.50 & 13.25\end{bmatrix}$
Constrained (Scaled)	$\begin{bmatrix}5\\2\end{bmatrix}$	$\begin{bmatrix}1 & 2\\2 & 8\end{bmatrix}$	$\begin{bmatrix}0\\0\end{bmatrix}$	$\begin{bmatrix}5 & 10\\10 & 36\end{bmatrix}$

sigma points to achieve convergence despite long measurement intervals.

2.5.2 Scaled UKF Concept

The UKF-S employs two scale factors to respect parameter constraints. The first scale factor, α, is the common scale factor used in the scaled UT, selected to ensure that all sigma point vectors are located in the allowable region. The allowable region is a space in which all points satisfy the parameter constraints along with an offset to account for a minimum sigma point bounding hyper-sphere radius, R_{min}. The minimum distance ensures that the sigma points will adequately represent the PDF through the transformation process.

Propagation of a Gaussian state through a nonlinear process provides some insight as to the necessity to specify a minimum hyper-sphere radius. The covariance matrix shown in Equation (2.17) is propagated forward for 2 seconds using scaled sigma points.

$$\begin{bmatrix} 1\times10^{6} & 0 & 0 & 0 \\ 0 & 1\times10^{6} & 0 & 0 \\ 0 & 0 & 2.5\times10^{-9} & 0 \\ 0 & 0 & 0 & 1\times10^{-4} \end{bmatrix} \tag{2.17}$$

Propagation commences from state values at the specified t_0 along the falling body state

trajectory to demonstrate the effect sigma point scaling has on covariance transformation. These sigma points do not require scaling to satisfy state constraints. However, transformation of the scaled sigma points demonstrates the impact of reducing the hyper-sphere radius. The scaled UT covariance matrix is compared with a covariance matrix propagated forward 2 sec using a 10,000 trial Monte Carlo. Many approaches to determine matrix similarity exist as summarized by Vemulapalli and Jacobs [44]. The Jensen-Bregman log-det (JBLD) divergence value, shown in Equation (2.18), is particularly useful to compare the covariance matrix similarity [44], [45].

$$\mathcal{J}_{ld} = \sqrt{\log\left(\det\left(\frac{X+Y}{2}\right)\right) - \frac{1}{2}\log\left(\det\left(XY\right)\right)} \tag{2.18}$$

The JBLD technique is a computationally efficient technique applicable to positive definite square matrices [45]. Identical matrices will produce a JBLD divergence value of 0. The JBLD divergence values are used to determine the quality of the different scaled UT propagation. JBLD divergence values presented in Table 2.3 reveal that in regions where the process model is effectively linear, such as at $t_0 = 0$, the scale factor has no impact upon the propagated covariance matrix. However, in regions of the state trajectory that are subject

Table 2.3. Comparison of scaled UT propagated covariance matrices with Monte Carlo propagated covariance.

α	1	0.8	0.6	0.4	0.2
$t_0 = 0$ s	1.2998×10^{-2}	1.2998×10^{-2}	1.2998×10^{-2}	1.2998×10^{-2}	1.2998×10^{-2}
$t_0 = 8$ s	1.5271×10^{-2}	1.5102×10^{-2}	$1.492\,91 \times 10^{-2}$	1.4855×10^{-2}	1.4841×10^{-2}
$t_0 = 10$ s	1.1009×10^{-2}	1.2348×10^{-2}	1.5065×10^{-2}	1.6645×10^{-2}	1.6949×10^{-2}
$t_0 = 12$ s	2.0880×10^{-2}	2.3343×10^{-2}	2.8994×10^{-2}	3.2350×10^{-2}	3.2999×10^{-2}

to significant nonlinearity, such as at $t_0 = 12$, the similarity of the propagated covariance matrix is less for smaller scale factors. Equivalently, smaller bounding hyper-sphere radii have greater impact on the quality of the propagated covariance.

The effect of the bounding hyper-sphere radius is also visible through comparing the error along the covariance matrix main diagonal. The percent of covariance propagation error between the different scaled UT propagation and the Monte Carlo propagation is shown

in Figure 2.24. The covariance of each state is represented by the respective covariance matrix main diagonal term.

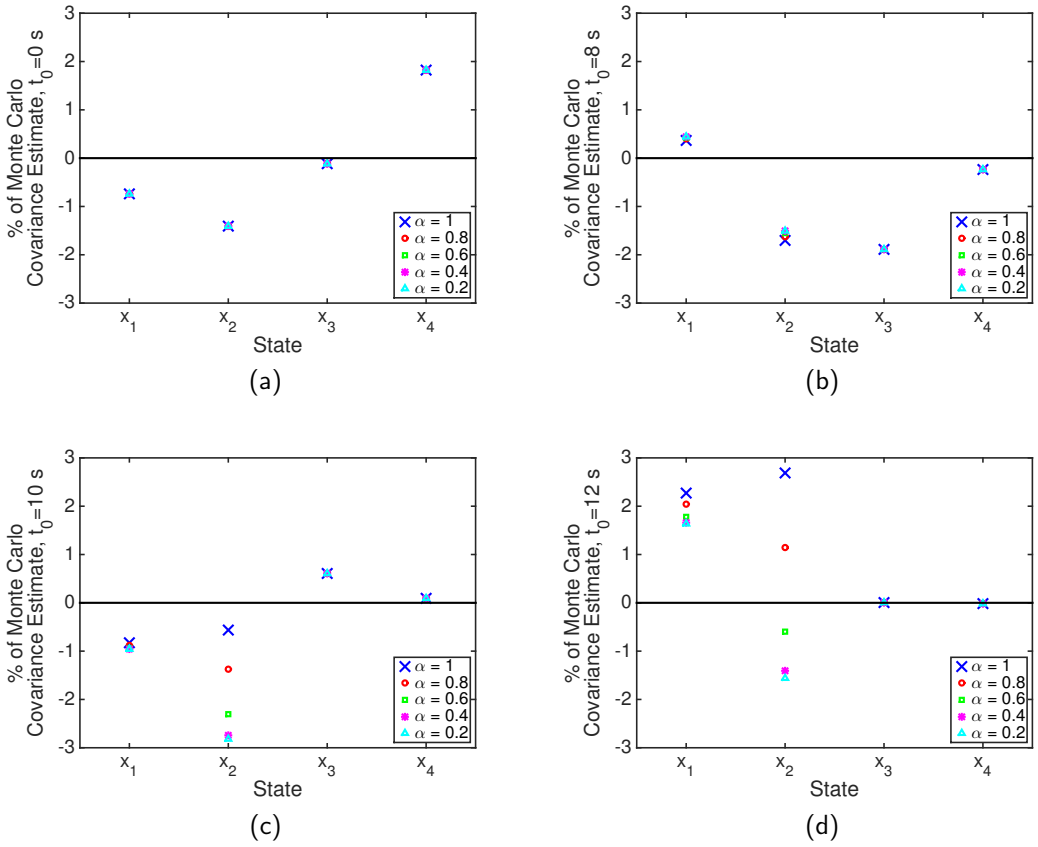

Figure 2.24. Arbitrary covariance (Equation (2.17)) 2 sec propagation from the specified t_0 falling body truth trajectory starting point: (a) depicts the % error comparison, $t_0 = 0$ s, (b) the % error comparison, $t_0 = 8$ s, (c) the % error comparison, $t_0 = 10$ s, and (d) the% error comparison, $t_0 = 12$ s.

The scale factor, α, is conceptually determined by finding the maximum radius, R_{max}, of a hyper-sphere centered on the estimate that will satisfy all constraints.[11] The state estimate must be relocated into the allowable region if the maximum hyper-sphere radius satisfying all constraints is shorter than the minimum allowable, R_{min}. The minimum bounding hyper-sphere radius, R_{min}, can be a constant, as demonstrated later in Section 2.5.4, or vary along the state trajectory.

[11]State estimates located outside of the allowable region have $R_{max} = 0$.

The required sigma point scale factor is known if $R_{max} \leq R_{min}$ (i.e., state estimate relocation is required), $\alpha = \alpha_{min}$. Additionally, the scale factor, $\alpha = 1$, is known if no scaling is required as occurs if $R_{max} \geq \sqrt{n+\kappa}$.[12] In these instances, no sigma point scaling is required to satisfy constraints. The scale factor must be calculated in instances when $R_{min} < R_{max} < \sqrt{n+\kappa}$ using Equation (2.19).

$$\alpha = \frac{R_{max}}{\sqrt{n+\kappa}} \tag{2.19}$$

The URNDDR sigma point selection method, detailed in Equations (2.13) and (2.14), could conceptually be employed in the UKF-S instead of the scaled UT. However, it is not used due to the greater complexity required to select the associated weights, as shown in Equation (2.14). Additionally, the weights generated for a given common scale factor are not consistent with those of the scaled UT sigma point approach. Further review reveals that the URNDDR approach does not produce a sigma point set that exactly matches the covariance if a symmetric bounding hyper-sphere is used. Rather, the URNDDR sigma point set for a symmetric bounding hyper-sphere matches a scaled covariance, as shown in Equation (2.20), which has negative implications for the quality of the post-transformation covariance.

$$P_{URNDDR} = \left(\frac{\alpha^2 \left(\alpha + 2\kappa + 2n - 2\alpha\kappa - 2\alpha n \right)}{2n - 2\alpha n + 1} \right) P_x \tag{2.20}$$

A second common scale factor, K_s, is used to relocate the state estimate into the allowable region when performing the UKF update, if necessary. The *a posteriori* state estimate, $\hat{x}_k^+$, of the UKF-S is formed, as shown in Equation (2.21).

$$\hat{x}_k^+ = \hat{x}_k^- + K_{s,k} K_k \left(\tilde{y}_k - \hat{y}_k \right) \tag{2.21}$$

The Kalman gain, K_k, is scaled by $K_{s,k}$, the minimum magnitude deviation from $K_{s,k} = 1$ necessary, to locate the state estimate, $\hat{x}_k^+$, in the allowable region. $K_{s,k} = 1$ if scaling is not required (i.e., the *a posteriori* state estimate, $\hat{x}_k^+$, is found in the same manner as the UKF shown in Equation (1.45)). The variance of the state estimate is determined, as shown in

[12] The threshold, $\sqrt{n+\kappa}$, applies for the extended symmetric sigma point set. The threshold is the radius of a bounding hyper-sphere encompassing all sigma points in a set.

Equation (2.22), using the same common scale factor, $K_{s,k}$, for the mean and covariance.

$$P_k^+ = P_k^- - (K_{s,k}K_k)P_y(K_{s,k}K_k)^T \tag{2.22}$$

Kalman gain scaling does not necessarily reduce the optimality of the estimate since the UKF is known to be a suboptimal estimator for nonlinear estimation.

2.5.3 Scaled UKF Implementation

The scaled UT demonstrated in Section 2.5.4 is implemented without determination of the maximum allowable bounding hyper-sphere, R_{max}. This approach avoids the need to perform the computationally intensive nonlinear estimation problem to calculate R_{max} each update step. The allowable region is instead defined as the space bounded by the parameter constraints and an additional specified offset from the constraints referred to as a "guard band". The guard band is established to ensure that the sigma point scaling will not result in a scale factor, $\alpha < \alpha_{min}$. This approach can only be applied if the mean itself is in the allowable region as discussed in Section 2.5.2. The *a posteriori* mean is positioned, if necessary, into the allowable region through use of the Kalman gain scaling discussed in Section 2.5.2.

The scaling factor, α_i, is selected, as shown in Equation (2.23), $\forall\ i = 1, \ldots, N$ where N is the number of sigma point vectors, and j is the constrained state.

$$\alpha_i = \frac{\text{Constraint} - \chi_{0,j}}{\chi_{i,j} - \chi_{0,j}} \tag{2.23}$$

Scaling occurs if any $\alpha_i \in (0, 1]$. The smallest α_i, is used for the scaling of Equation (2.15) as a common scale factor to ensure all sigma points remain within the constraints. If all $\alpha_i \geq 1$, scaling is not necessary to satisfy the state constraints. This approach maintains the symmetry of sigma points about the mean. The affine transformation of the original sigma points and weights, shown in Equation (2.15), ensures that the mean and covariance of the scaled sigma point set is not altered, as discussed in Section 2.5.2. Figure 2.25 graphically shows the UKF-S scale factor selection process.

The scaled UT can be applied to calculate the UKF *a priori* estimate using Equation (1.41). Parameters will remain within constraints throughout the prediction step since they do not

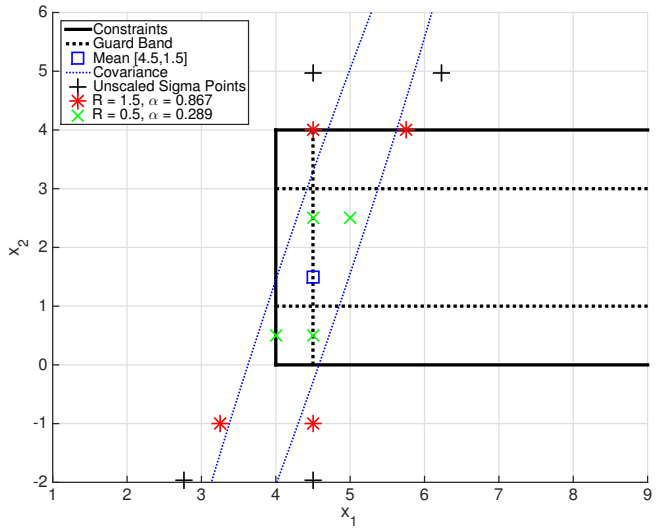

Figure 2.25. Two-dimensional example of UKF-S scaling. $\alpha = 0.289$ required for all sigma points to satisfy the constraints.

have process dynamics. Integration of state process dynamics can still lead to state constraint violation during propagation to the measurement time. The scaled UT can also be applied to calculate the predicted measurement using Equation (1.42), if necessary.

2.5.4 Simulation Results

The results presented in this section include adaptive scaling that maintains all sigma points $x_3 > 0$ but does not enforce the physical limits of the other states. A $x_{3,Con}$ constraint, $x_3 > 1 \times 10^{-5}$, is employed to enforce the physical limit. Additionally, a x_3 guard band, $x_{3,Guard} = 1 \times 10^{-5}$, to allow for the propagation of the sigma points as described in the previous section. Table 2.4 presents the sigma points of Table 2.1 following scaling to respect the ballistic coefficient, x_3, physical constraint. Table 2.4 is generated assuming filter initialization parameters of Section 2.2. The weighted mean and covariance of both sets of initial sigma points are equivalent. The higher order moments associated with each set differ.

Figure 2.26 presents the results of a 100-trial Monte Carlo study, comparing the EKF2, UKF, and UKF-S using the same measurements as Section 2.3 sampled at the specified frequencies. The UKF-S adaptive scaling technique improves UKF robustness while ap-

Table 2.4. Falling body example of Section 2.2 $2n+1$ scaled ($\alpha = 0.4995$) sigma point set at $t = 0$.

Sigma Points (2n+1)	1	2	3	4	5	6	7	8	9
Weight	0	0.125	0.125	0.125	0.125	0.125	0.125	0.125	0.125
Altitude, x_1 (ft)	300000	300999	300000	300000	300000	299001	300000	300000	300000
Velocity, x_2 (ft/s)	20000	20000	21998	20000	20000	20000	18002	20000	20000
β, x_3 (1/ft)	0.01	0.01	0.01	0.01999	0.01	0.01	0.01	1.00×10^{-5}	0.01
g, x_4 (ft/s^2)	32.17405	32.17405	32.17405	32.17405	32.18404	32.17405	32.17405	32.17405	32.16406

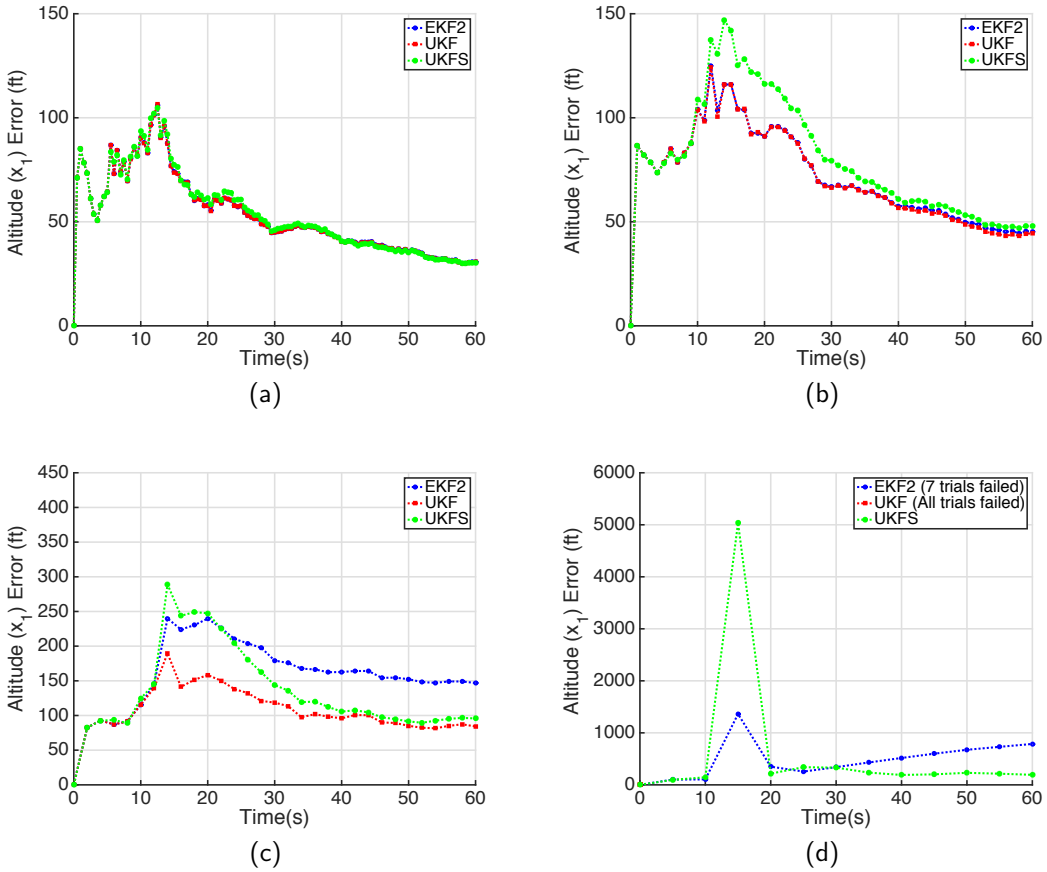

Figure 2.26. Comparison of EKF2, UKF, and UKF-S estimation performance, 100 trial average: (a) depicts average absolute altitude (x_1) error, 2 Hz measurements, (b), average absolute altitude (x_1) error, 1 Hz measurements, (c), average absolute altitude (x_1) error, 0.5 Hz measurements, and (d) average absolute altitude (x_1) error, 0.2 Hz measurements.

parently slowing the convergence rate at higher measurement frequencies. The UKF-S performs nearly identical to the EKF, EKF2, and UKF at the sufficiently fast measurement rate of 2 Hz. Sigma point scaling is required at the first 8 propagation intervals for 1 Hz measurements, the first 5 propagation intervals for 0.5 Hz measurements, and the first 3 propagation intervals for 0.2 Hz measurements. Kalman gain scaling is not necessary for this example since the state estimate for the ballistic coefficient, x_3, remains in the allowable region.

Tuning may be required as selection of different lower bound and guard bands may improve performance. The UKF-S converges at the 0.2 Hz measurement rate, Figure 2.26d, but fails to converge at longer intervals. Inspection of the sigma points at longer measurement intervals reveals that while x_3 remains within bounds, other states violate their respective physical limits. Additional state constraints can be incorporated into selecting the common scaling factor to ensure that sigma points respect physical bounds prior to propagation.

2.6 Conclusions

The literature contains numerous comparisons between EKF and UKF performance in application. Some authors have noted that the EKF and UKF often produce similar results and recommend use of the EKF based on reduced computation requirements. Their analyses do not account for the potential effect of measurement interval on estimator performance. As demonstrated in this chapter, the length of the measurement interval can impact estimator performance. While performance may be similar between the EKF and UKF at sufficiently high measurement frequencies, the UKF demonstrates greater tolerance to lengthened measurement intervals in the single-dimension falling body problem considered here.

Differences in the KF approximation techniques employed by the EKF and UKF is masked at relatively fast measurement rates. The impact of the approximation method is most obvious in instances when the covariance is significantly underestimated and the measurement interval is lengthened. This occurrence leads to the filter rejecting information from successive measurements. Once this occurs, the estimate tracks the predicted estimate, rejecting information from the measurements, and resulting in filter divergence. Process noise can reduce this effect by offsetting the covariance underestimation at the expense of reducing filter effectiveness. In instances when the covariance is overestimated, the filters do not

diverge, but will track the measurement, reducing filter effectiveness.

Sufficiently fast measurements lead to nearly identical performance between EKF, EKF2, and UKF implementations in the single dimension falling body problem considered in this chapter. However, the UKF is shown to outperform the EKF with sparse temporal measurements in this example. The difference in performance results from the propagation of the estimated covariance.

The UKF's failure when subjected to measurement frequencies less than 0.5 Hz, as detailed in Section 2.3.5, required consideration of a constrained UKF. A novel constrained UKF, the UKF-S, was presented in Section 2.5 to employ the scaled UT to increase the interval between measurements while using the UKF. This approach demonstrated the ability to lengthen the measurement interval in the example considered by using a constrained nonlinear estimator.

Chapter 3 will seek to confirm the results of this chapter through experimentation by considering another nonlinear estimation problem, a simple pendulum.

THIS PAGE INTENTIONALLY LEFT BLANK

CHAPTER 3:
Experimental Investigation

A simple pendulum problem is used to explore the effect of measurement frequency on KF–based nonlinear estimators through concurrent experiment and simulation. Section 3.1 provides a detailed description of the simple pendulum problem that is studied through simulation and experimentation. The experimental setup is described in detail in Section 3.2. The simulation is described in detail in Section 3.3. Results from simulation, Section 3.4, and experiment, Section 3.5, are presented for comparison to determine if measurement frequency impacts estimator performance in this problem and provide experimental validation of the simulation. Conclusions are presented in Section 3.6.

3.1 Pendulum Example

The pendulum system shown in Figure 3.1 is investigated to determine the impact of measurement frequency on the performance of KF–based nonlinear estimation algorithms. This

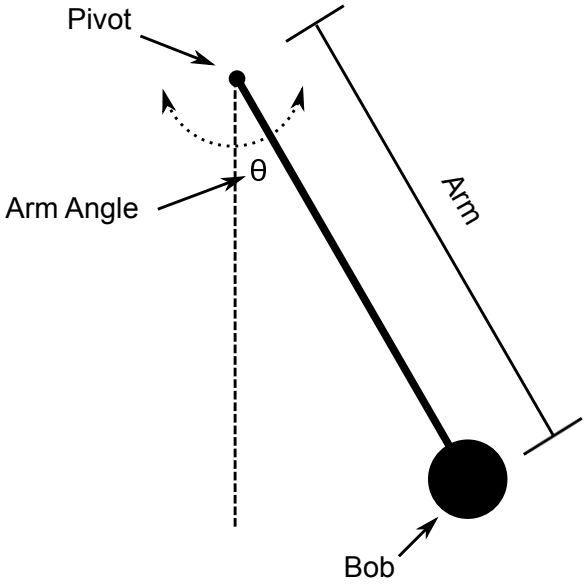

Figure 3.1. Schematic of simple pendulum

example was selected for two reasons. First, it is a periodic nonlinear system that has a well-understood model. Second, it allows for the setup of a simple laboratory experiment

for validation of the effect of measurement frequency on filter performance. The system is described by first-order ordinary differential equations with a two-dimensional state space, as shown in Equations (3.1) and (3.2) [46]. The pendulum arm angle, θ (rad), and the pendulum arm angular velocity, ω (rad/s), form the state space used to describe motion of the pendulum bob. An ideal, or mass-less arm, pendulum model is initially considered for simulation.

$$x = \begin{bmatrix} \theta \\ \omega \end{bmatrix} \tag{3.1}$$

$$\dot{x} = \begin{bmatrix} x_2 \\ \dfrac{-(lm)\, g \sin(x_1) - \beta x_2}{I_{Bob} + ml^2} \end{bmatrix} + \begin{bmatrix} 0 \\ w_2 \sim \mathcal{N}(0, Q_2) \end{bmatrix} \tag{3.2}$$

The pendulum arm length, l (m), the pendulum bob mass, m (kg), and gravitational acceleration, g (m/s^2), can be measured rather accurately while the system is stationary. The bob's moment of inertia, I_{Bob} (kg m^2), and the system damping ratio, β (kg m^2/s), may be challenging to directly measure. These terms can introduce significant model error resulting in poor estimation of the system state. All damping forces to include sliding friction at the pendulum pivot, air resistance, etc. are represented by β. The moment of inertia and damping coefficient are expected to remain constant during the interval between measurements and are treated as parameters. The state space can be augmented with these estimated parameters, as shown in Equation (3.3), to enhance the model fidelity.

$$x = \begin{bmatrix} \theta \\ \omega \\ I_{Bob} \\ \beta \end{bmatrix} \tag{3.3}$$

The resulting system dynamics are represented by Equation (3.4). The additive process noise included in this equation is used to account for any anticipated model inaccuracy. The noise associated with x_2 and the estimated parameter, x_4, are uncorrelated since w_2 only accounts for the inaccuracy resulting from the parameters (l, m, and g) that are not estimated along with additional modeling inaccuracies not accounted for by the estimated parameters. The x_3 parameter, I_{Bob}, does not have any noise associated with it since it

is not expected to change during the interval of interest. The x_4 parameter, the damping coefficient, may change during the interval of interest, hence the addition of the process noise term, w_4.

$$\begin{bmatrix} \dot{x}_1 \\ \dot{x}_2 \\ \dot{x}_3 \\ \dot{x}_4 \end{bmatrix} = f(x(t)) = \begin{bmatrix} x_2 \\ \dfrac{-(lm)\, g \sin(x_1) - x_4 x_2}{x_3 + ml^2} \\ 0 \\ 0 \end{bmatrix} + \begin{bmatrix} 0 \\ w_2 \sim \mathcal{N}(0, Q_2) \\ 0 \\ w_4 \sim \mathcal{N}(0, Q_4) \end{bmatrix} \tag{3.4}$$

The measurement model is linear and discrete in this example, as shown in Equation (3.5).

$$y(t_k) = \begin{bmatrix} 1 & 0 & 0 & 0 \end{bmatrix} \begin{bmatrix} x_1(t_k) \\ x_2(t_k) \\ x_3(t_k) \\ x_4(t_k) \end{bmatrix} + \begin{bmatrix} v_1(t_k) \sim \mathcal{N}(0, R_1) \\ 0 \\ 0 \\ 0 \end{bmatrix} \tag{3.5}$$

Measurements are assumed to include an additive noise, $v_1(t_k)$, that is Gaussian and uncorrelated with any process noise. The measurement model satisfies the linearity requirements of the KF. The process model, however, is nonlinear; therefore, the estimate is not optimal when using the KF structure.

A second model, the physical pendulum, shown in Equation (3.6), is also considered to better reflect the experimental setup where the pendulum arm has mass and therefore affects the system dynamics [46]. The pendulum arm is considered a cylindrical tube allowing application of the standard equation, $I_{Arm} = I_{Cylinder} = \frac{m}{12}\left(3r^2 + h^2\right)$ where m is the mass of the tube, $r = r_{Arm}$ is the pendulum arm radius, and $h = h_{Arm}$ is the length of the

pendulum arm from the top of the bob to the pendulum pivot [47].

$$\dot{x} = \begin{bmatrix} x_2 \\ \dfrac{-\left(lm_{Bob} + \left(\dfrac{h_{Arm}}{2}\right)m_{Arm}\right)g\sin(x_1) - x_4x_2}{x_3 + m_{Bob}l^2 + I_{Arm} + m_{Arm}\left(\frac{h_{Arm}}{2}\right)^2} \\ 0 \\ 0 \end{bmatrix} + \begin{bmatrix} 0 \\ w_2 \sim \mathcal{N}(0, Q_2) \\ 0 \\ w_4 \sim \mathcal{N}(0, Q_4) \end{bmatrix} \tag{3.6}$$

The following simulations assume that the filter is initialized to an estimate that reflects the actual state, as shown in Equation (3.7). x_1 is the arm angle at $t = 0$ s. An initial deflection of approximately 0.698 rad (40 deg) is selected so that the pendulum is not in an equilibrium position and that a small angle approximation for $sin(x_1)$ is a poor assumption. The pendulum is assumed stationary at $t = 0$, $\omega(t_0) = 0$ rad/s. x_3 is the calculated bob moment of inertia, 2.758×10^{-3} kgm^2, assuming the parameters from Table 3.1. The bob is assumed to be a cylinder of uniform density allowing the application of the standard equation, $I_{Bob} = I_{Cylinder} = \frac{m}{12}\left(3r^2 + h^2\right)$, where m is the mass of the bob, r is the bob's radius, and h is the bob's height [47]. x_4 is estimated as $\beta_0 = 0.015$ kg m^2/s, 150% of the value obtained by experimentation, as discussed in Section 3.2.

$$x(t_0) = \begin{bmatrix} \theta(t_0) \\ 0 \\ I_{Bob} \\ \beta_0 \end{bmatrix} \tag{3.7}$$

The initial covariance matrix, $P(t_0)$, shown in Equation (3.8) is selected to reflect uncertainty in the initial state estimate. Despite appearing identical, the variance of the parameters, x_3 and x_4, is relatively larger than that of the angle and angular velocity due to the respective units and reflects the inherent uncertainty in the calculated initial estimate. The

same variance is used for all filters in simulation and experimental comparisons.

$$P(t_0) = \begin{bmatrix} 1 \times 10^{-4} & 0 & 0 & 0 \\ 0 & 1 \times 10^{-4} & 0 & 0 \\ 0 & 0 & 1 \times 10^{-4} & 0 \\ 0 & 0 & 0 & 1 \times 10^{-4} \end{bmatrix} \tag{3.8}$$

3.2 Experimental Setup Details

The pendulum experimental setup is shown in Figure 3.2. Experiment parameters are presented in Table 3.1. This data was obtained by measuring the physical parameters associ-

Table 3.1. Measured pendulum experiment physical parameters.

Parameter	Value
l	405.0 mm
r_{Bob}	46.0 mm
h_{Bob}	65.0 mm
r_{Arm}	6.3 mm
m_{Bob}	3.13 kg
m_{Arm}	322.6 g

ated with the pendulum experiment. Length measurements less than 200 mm was obtained using calipers with accuracy of ±0.03 mm. Length measurements in excess of 200 mm was obtained using a tape measure with accuracy of ±0.5 mm. Mass was obtained using a scale with accuracy of ±1 g.

An optical encoder and a potentiometer sense pendulum arm angle simultaneously. The encoder data is an accurate, essentially noiseless measurement signal. The potentiometer data provides a noisier measurement for comparison.

Data is acquired using an Arduino Uno board and Mayhew Engineering 16-Bit Extended Analog-to-Digital Shield, shown in Figure 3.3, to perform the potentiometer analog to digital conversion. It also transmits the digital encoder and potentiometer output via a serial connection to a computer for storage and offline estimation. As noted in Section 3.3,

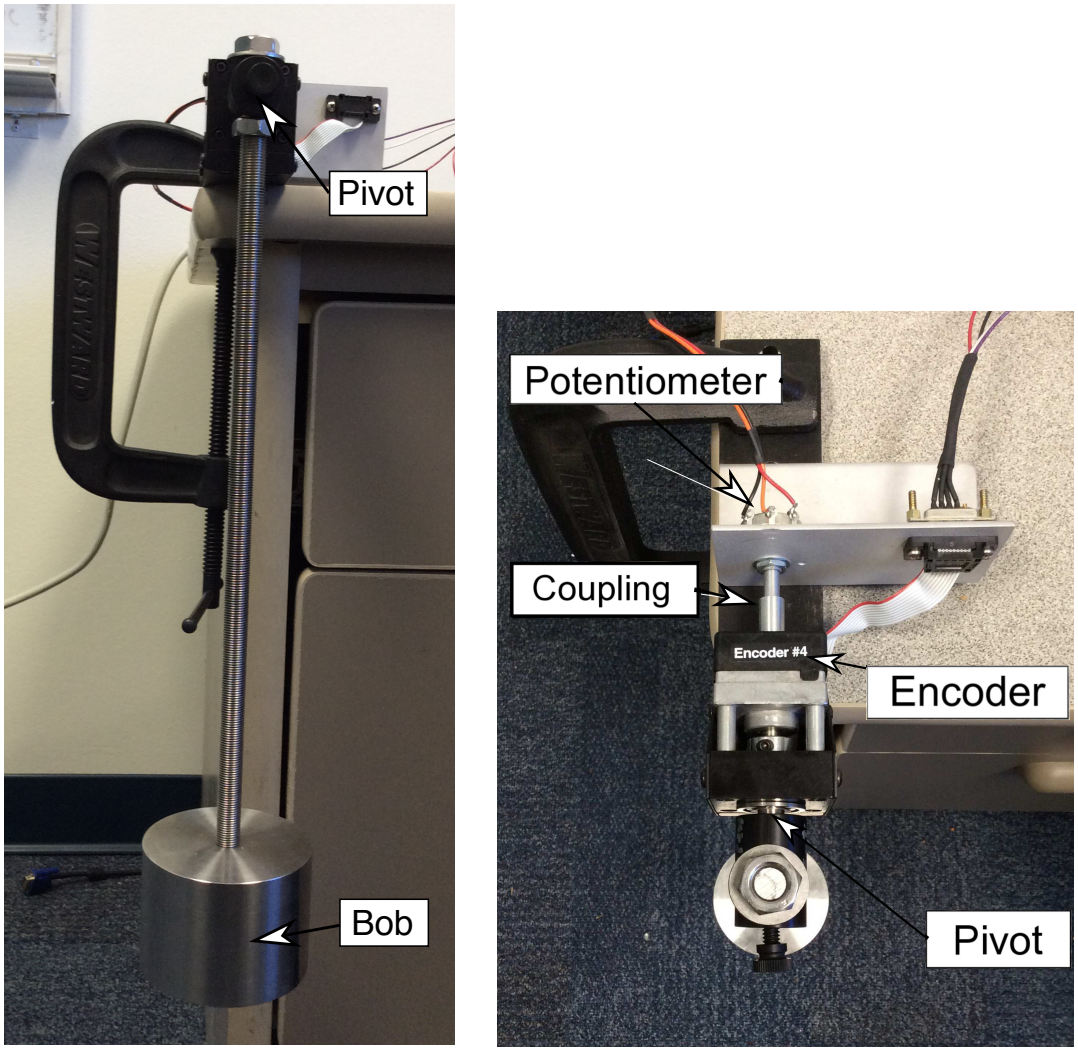

(a) (b)

Figure 3.2. Pendulum experimental set-up: (a) depicts the pendulum experiment, front view, and (b) the pendulum experiment, top view.

these two sensors are selected to provide an accurate measurement of the pendulum arm angle along with a less accurate measure. Additionally, these sensors provide representative angle measurements that are commonly available for control systems.

The optical encoder is a Computer Optical Products, Inc. CP-350-4096 digital incremental optical encoder. It has 16,384 counts per revolution producing a resolution of 3.835×10^{-4} rad/count (2.197×10^{-2} deg/count).

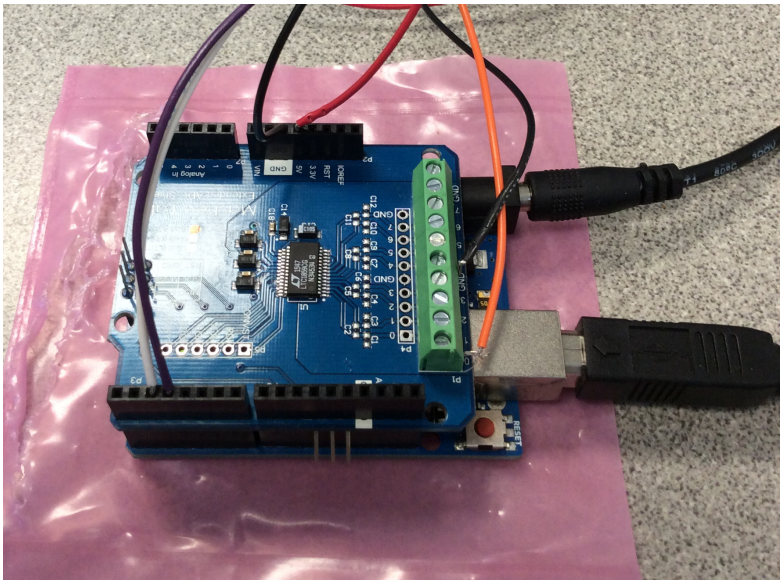

Figure 3.3. Arduino Uno with Mayhew Engineering 16-Bit Extended Analog-to-Digital Shield

The potentiometer is a RadioShack 5 kΩ ± 20% linear-taper potentiometer with a nominal total rotation of 300 ± 5 deg. This potentiometer has an actual resistance of 4.54 kΩ. The potentiometer is connected to the Arduino Uno's 5 V power supply. The 16-bit analog to digital converter has 65,356 counts. This results in a theoretical resolution of 7.99×10^{-5} rad/count (4.58×10^{-3} deg/count) when used with a 5 V power supply, nearly an order of magnitude better resolution than the encoder. The potentiometer was rotated 50 times from hanging stationary through 90 deg of travel as measured in encoder counts (4096 counts). This data is used to determine the radian per potentiometer count conversion to allow for comparison between the potentiometer and encoder. A resolution of 6.95×10^{-5} rad/count (3.98×10^{-3} deg/count) is obtained.

The potentiometer measurement is corrupted by both electrical and mechanical noise. Electrical noise associated with the potentiometer signal was determined using an oscilloscope, as shown in Figure 3.4. The signal displayed random noise with a standard deviation of approximately 1 mV while the potentiometer is stationary. This equates to a standard deviation of 9.10×10^{-4} rad (5.22×10^{-2} deg). This noise level requires a 16-bit analog to digital converter to provide resolution necessary for sensing the Gaussian noise signal.

The potentiometer is subject to hysteresis from the slotted coupling connecting the poten-

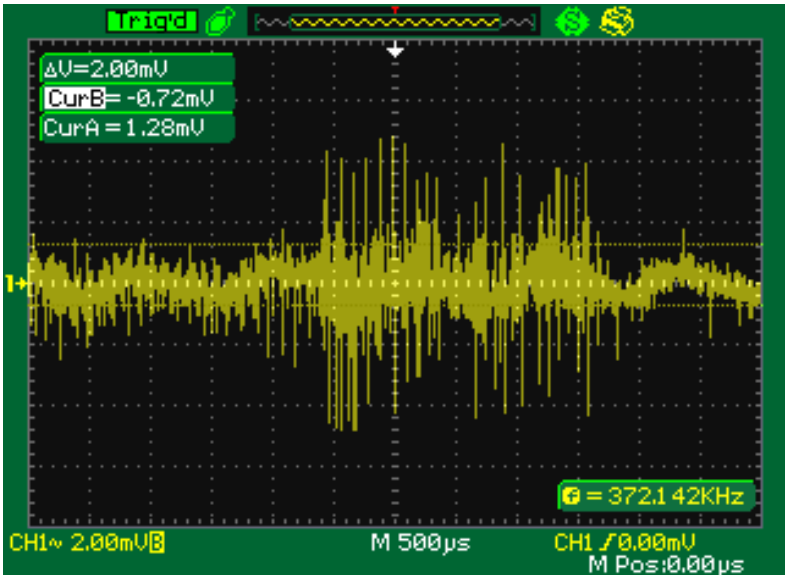

Figure 3.4. Electrical noise in potentiometer voltage output detected using an oscilloscope.

tiometer wiper to the pendulum pivot. Additionally, the wiper is subject to static friction that must be overcome before angular change is detected. Figure 3.5 shows an example of the data collected using this experimental set-up. A standard deviation of 159.05 counts over the 50 trial runs, approximately 1.11×10^{-2} rad (6.33×10^{-1} deg), was observed when the potentiometer is connected to the 5 V power supply. This value includes mechanical noise in addition to the electrical noise.

The angle measurement is calibrated by zeroing the angle measurement with the pendulum motionless, hanging down in the lower equilibrium position. This calibration method ensures gravitational acceleration is acting in the direction of the pendulum arm with a 0 rad arm angle as assumed in the modeling process.

Angle data is recorded off of the serial bus in a continuous stream at 250000 baud with the message containing a time stamp, encoder counts, and potentiometer counts. This data collection system produces an average 947 Hz measurement signal. The measurement frequency is irregular and varies from 880 Hz to 1147 Hz. The stored measurement stream is sampled offline at the average desired frequency to investigate filter performance at lower measurement frequencies. Sampling is performed by using the measurement nearest to the desired time vice using interpolation. This approach allows studying the impact of sparse

temporal measurements while maintaining measurement independence.

The gravitational acceleration constant is assumed to be equal 9.81 m/s^2. The data from Figure 3.5 is used to determine an approximate damping coefficient for initialization purposes. The damping coefficient, x_3, is approximated as 0.01 $\text{kg m}^2\text{/s}$ by using Figure 3.5a in conjunction with the physical pendulum model to match the angle amplitude lost during each period.

Figure 3.5b reveals substantial hysteresis in the potentiometer signal. This effect is not accounted for in the linear measurement model specified in Section 3.1. The potentiometer hysteresis must be accounted for by either altering the model or increasing the measurement noise in order to use the potentiometer information in the EKF or UKF.

A single trial of the experiment is conducted to collect the sensor data. The encoder angle information is used as accurate measurement information since it is subject to significantly less noise than the potentiometer signal. The desired measurement frequency is obtained by sampling the sensor data at intervals that average to the specified frequency while running the filters offline. This approach results in irregular measurement intervals. All filters are initialized using the initial encoder angle from the experimental data and an initial angular velocity, $x_2(t_0) = 0$ rad/sec. An initial angle of approximately 0.6 rad (35 deg) is used to ensure a nonlinear model is required to model the system state.

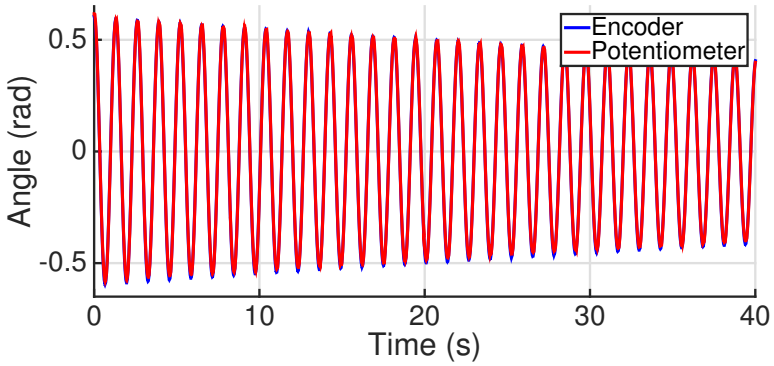

(a) Pendulum angle measurements

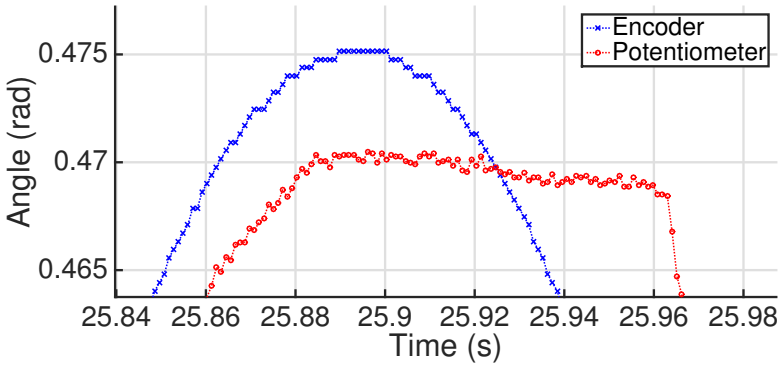

(b) Pendulum angle measurements, expanded view

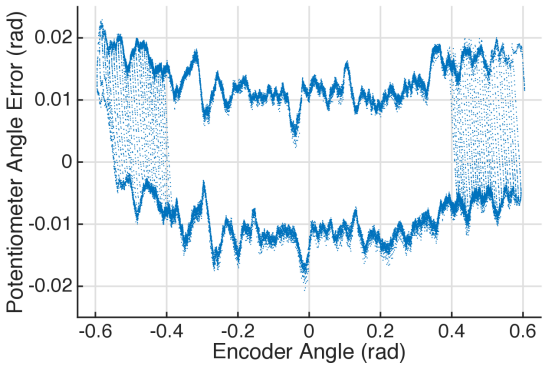

(c) Encoder vs. potentiometer error

Figure 3.5. Representative trial comparing simultaneous encoder and potentiometer pendulum angle measurements: (a) depicts pendulum angle measurements (rad), (b) an expanded view of pendulum angle measurements, (rad), and (c) encoder versus potentiometer error pendulum angle measurements.

3.3 Simulation Details

A simulation of the simple pendulum is performed to determine the measurement frequency at which estimator performance is affected. The system of equations shown in Equation (3.9) is propagated in time to generate a truth model using MATLAB's *ode*45 function.

$$\dot{x} = \begin{bmatrix} x_2 \\ \dfrac{-\left(l m_{Bob} + \dfrac{l - h_{Bob}}{2} m_{Arm}\right) g \sin(x_1) - \beta x_2}{I_{Total}} \end{bmatrix} \tag{3.9}$$

The total system moment of inertia, I_{Total}, is calculated using Equation (3.10) with the data from Table 3.1, 5.31×10^{-1} kg m^2; β is set at 0.01 kg m^2/s as experimentally approximated in Section 3.2. Assumed initial conditions are $x_1 = 0.873$ rad; $x_2 = 0$ rad/s. Figure 3.6 shows the truth model for all simulations of this example.

$$I_{Total} = I_{Bob} + ml^2 + I_{Arm} + m\left(\frac{l - h_{Bob}}{2}\right)^2 \tag{3.10}$$

The simulation is based on the physical pendulum model to more closely approximate the experimental setup, facilitating validation of the simulation results. Although the ideal pendulum model produces a very similar path, as seen in Figure 3.7a, the two models are actually out of phase as a result of the physical pendulum model's larger total moment of inertia altering the period of oscillation. The model difference results in significant angular position differences that are shown in Figure 3.7b. This illustration should be considered when analyzing the performance of the filtering algorithms in practical applications as demonstrated in Section 3.5.

The generated true angle data, shown in Figure 3.6a, is corrupted with an additive random noise to generate noisy measurements. Noisy measurements for the accurate position information used in Section 3.4 are generated using an additive Gaussian noise, $\sim \mathcal{N}(0 \text{ rad}, 1.324 \times 10^{-6} \text{ rad}^2)$. The noise strength is selected to account for noise 3 times the resolution of the encoder used in the experimental setup (3.835×10^{-4} rad/count). Noisy measurements for the poor position information shown in Section 3.4 are generated

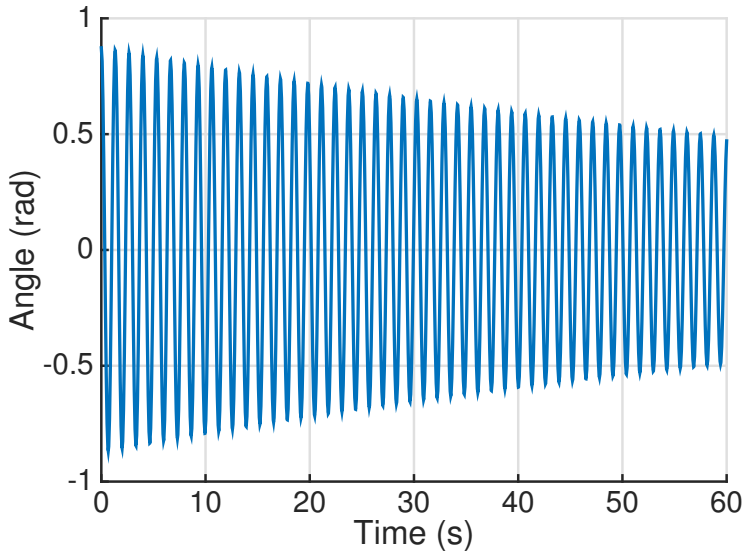

(a)

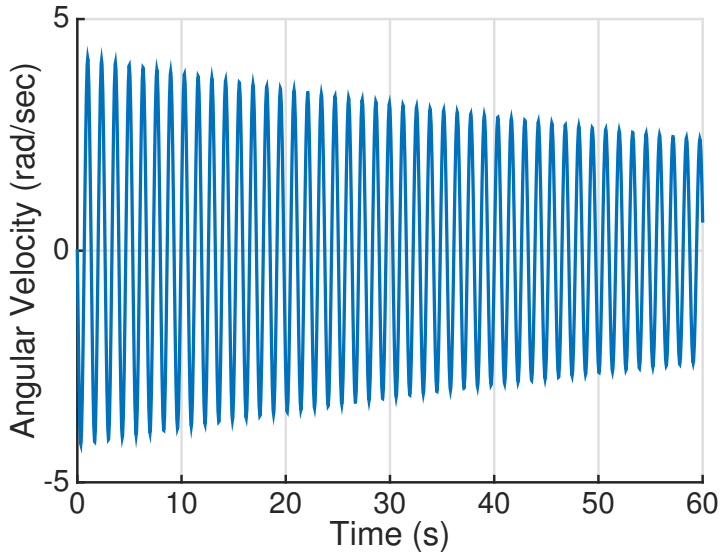

(b)

Figure 3.6. Pendulum problem, truth generated by propagating initial conditions: (a) depicts angle (x_1) and (b) angular velocity (x_2).

using an additive Gaussian noise, $\sim \mathcal{N}(0 \text{ rad}, 1.000 \times 10^{-4} \text{ rad}^2)$. The variance information calculated in Section 3.2 for the potentiometer, using 5 V input and applied as noise in simulation, does not replicate the hysteresis and lag visible in Figure 3.5b. It does, how-

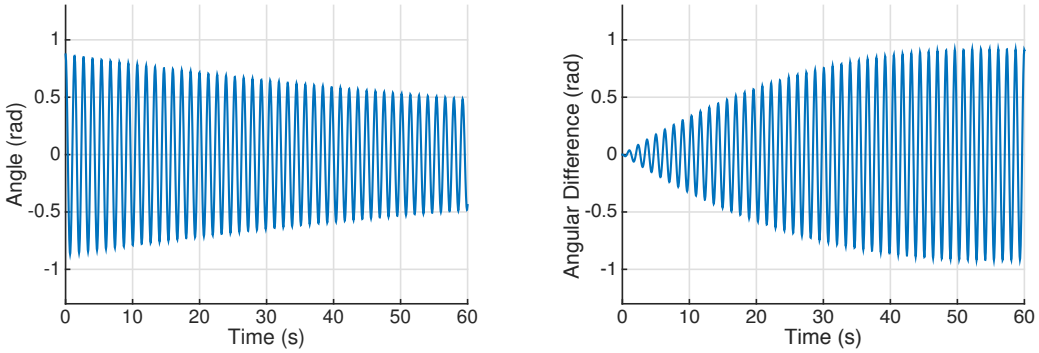

(a) (b)

Figure 3.7. Comparison of truth generated by propagating initial conditions using the ideal versus physical pendulum models: (a) depicts the ideal model angle, x_1 (rad) and (b) physical and ideal pendulum models, angular difference (rad).

ever, provide some sense of filter convergence with noisy measurement information. Two levels of measurement noise are considered since noisier measurements place a greater burden on the model to more accurately predict covariance in order to properly weight poor measurements.

A 100 trial Monte Carlo study is conducted using a set of 100 independent trials of both accurate and poor measurement information. Each trial has a unique measurement signal corrupted by uncorrelated noise. Each measurement signal is generated at 1000Hz to allow sampling at varied measurement frequencies. Figures 3.8a and 3.8b noisy measurements sampled at 100 Hz are a representative example of the measurement error used within each individual trial. Each filter is tested using the same set of 100 trials to allow for meaningful performance comparison.

The different measurement frequencies investigated are produced through sampling the 1000Hz noisy measurement data at the desired rate. Three filters are compared; the EKF, EKF2, and UKF are each initialized using the same values as in Section 3.2. Process noise is not included in Section 3.4 since the physical process model was used to generate the truth plot for these simulations. Average absolute error in the state estimate is used to compare filter performance.

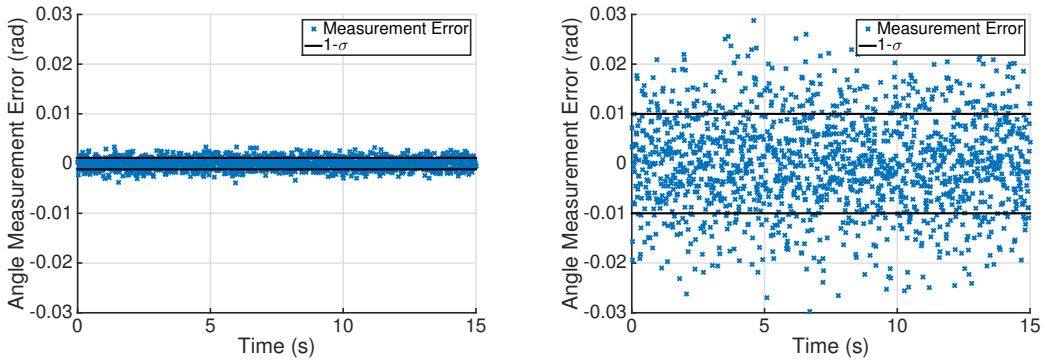

Figure 3.8. Representative noisy measurement error: (a) depicts accurate noisy measurement error, 100 Hz and (b) poor noisy measurement error, 100 Hz.

3.4 Simulation Results

Simulation results presented in this section are generated with the EKF, EKF2, and UKF assuming the physical pendulum truth model shown in Equation (3.6). Process noise, w_2 and w_4, is not added since the truth model and the assumed filter model are identical. Results are presented at two frequencies, 100 Hz and 1 Hz, to determine if the measurement frequency effect seen in the falling body problem is present in the pendulum system. The 1 Hz frequency is presented to ensure that the pendulum motion is sampled at least once each period.

3.4.1 Accurate Measurements

These results are produced using measurements with Gaussian noise, $\sim \mathcal{N}(0 \text{ rad}, 1.324 \times 10^{-6} \text{ rad}^2)$, representing optical encoder measurement noise. The average absolute error plots shown in Figures 3.9 and 3.10 reveal that in contrast to the falling body problem in Section 2.3, the three filtering techniques generated nearly identical results at both frequencies tested.

Additionally, the average estimated covariance remains nearly identical for all three filters as shown in Figure 3.11 by the average estimated angle, x_1, standard deviation. The magnitude of the average estimated standard deviation is smaller at the higher measurement frequency since the filters are receiving information from measurements 100 times more

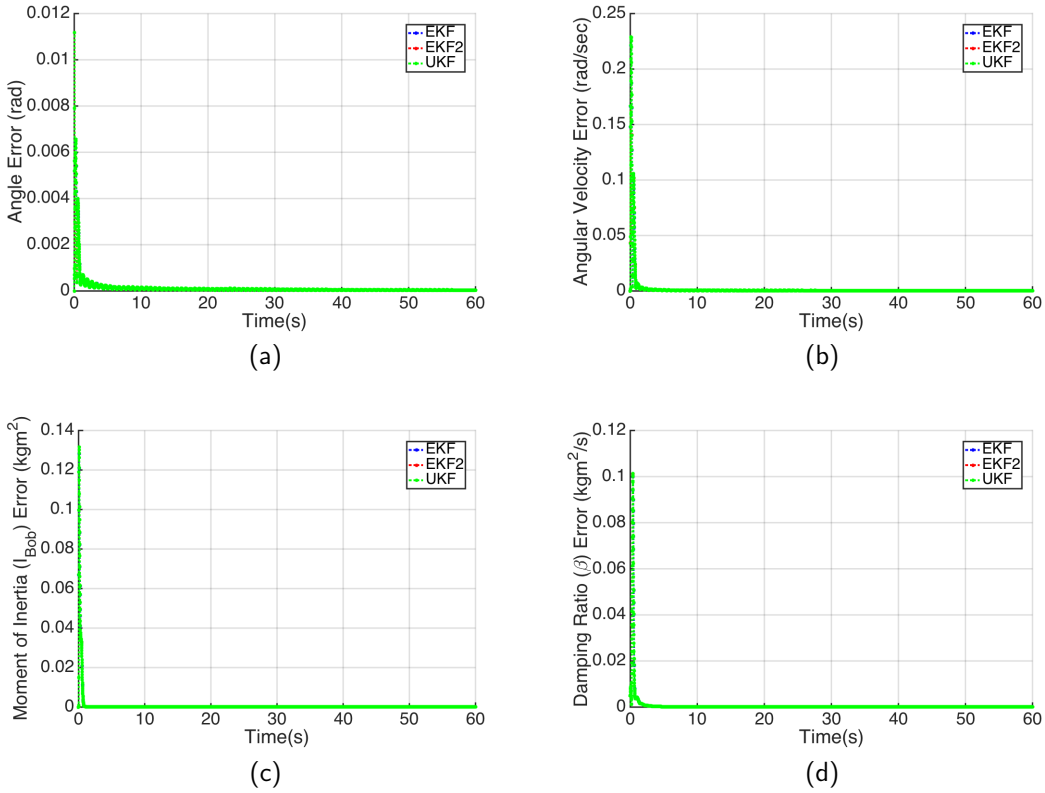

Figure 3.9. Comparison of EKF, EKF2, UKF estimation performance using a physical pendulum process model with accurate 100Hz measurements, 100 trial average: (a) depicts average absolute angle (x_1) error, (b) average absolute angular velocity (x_2) error, (c) average absolute I_{Bob} (x_3) error and (d) average absolute damping ratio, β, (x_4) error.

frequently.

The average innovation shown in Figure 3.12 provides an additional measure of filter performance. A pattern exists in the average innovation plots at both frequencies as a result of the model mismatch caused by the damping ratio, x_4, initialization error. Each estimation algorithm corrects the model by adjusting the damping ratio, resulting in random innovations occurring as anticipated in steady-state.

A representative single trial's innovations are presented in Figure 3.13 for comparison with the experimental results shown later in Figure 3.18 of Section 3.5.

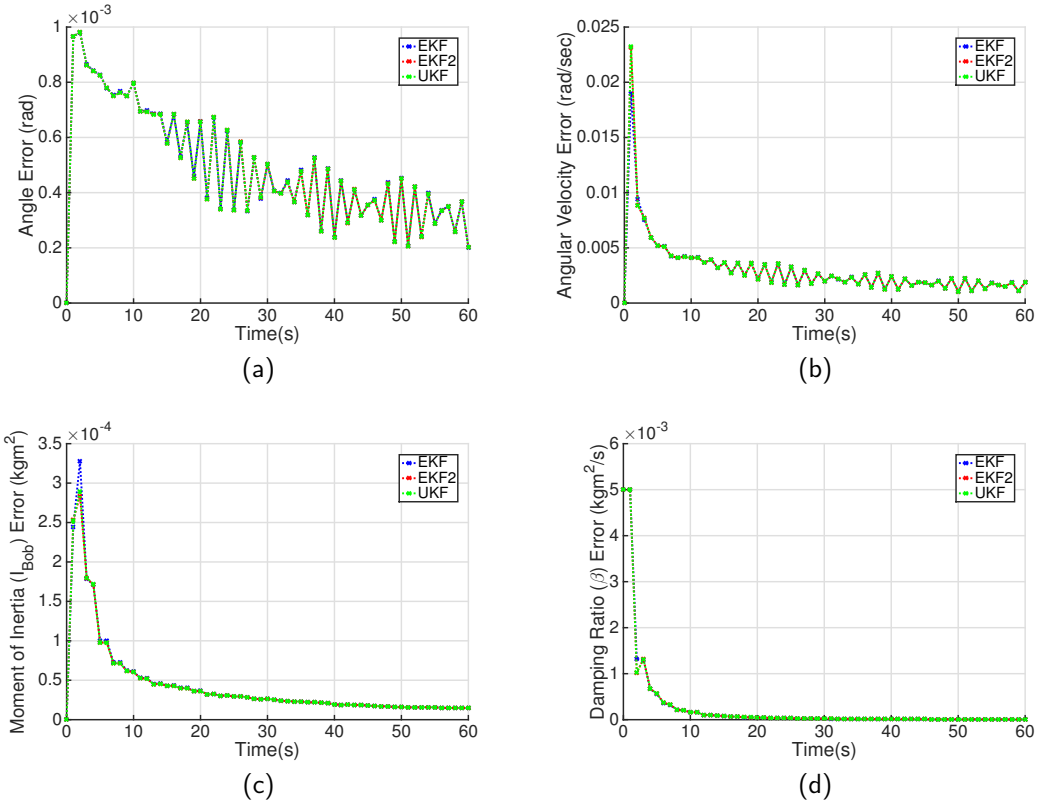

Figure 3.10. Comparison of EKF, EKF2, UKF estimation performance using a physical pendulum process model with accurate 1Hz measurements, 100 trial average: (a) depicts average absolute angle (x_1) error, (b) average absolute angular velocity (x_2) error, (c) average absolute I_{Bob} (x_3) error and (d) average absolute damping ratio, β, (x_4) error.

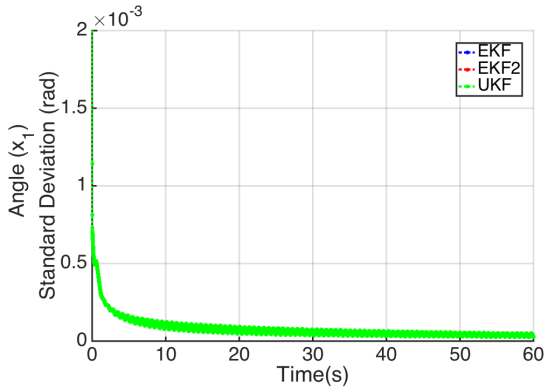

(a)

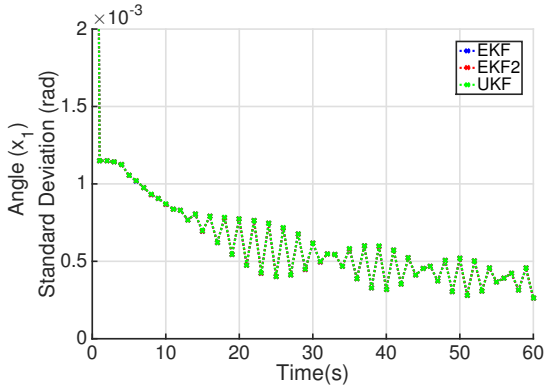

(b)

Figure 3.11. Comparison of EKF, EKF2 and UKF 100 trial average estimated angle (x_1) standard deviation, physical pendulum process model with accurate measurements: (a) depicts 100 Hz measurements and (b) 1 Hz measurements.

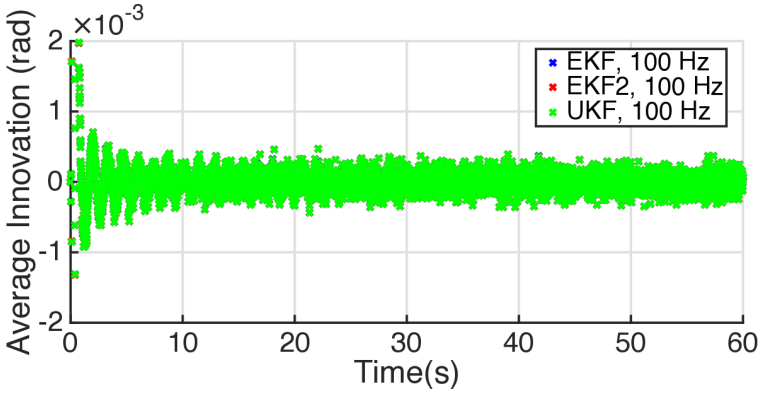

(a)

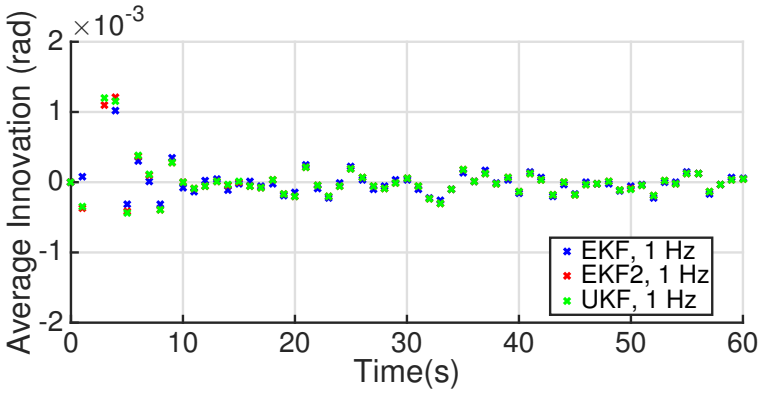

(b)

Figure 3.12. Comparison of EKF, EKF2 and UKF 100 trial average innovations, physical pendulum process model with accurate measurements: (a) depicts 100 Hz measurements and (b) 1 Hz measurements.

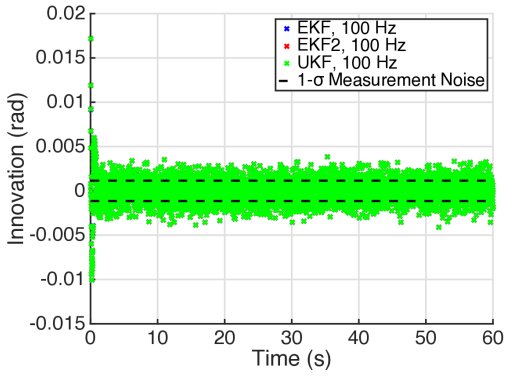

(a)

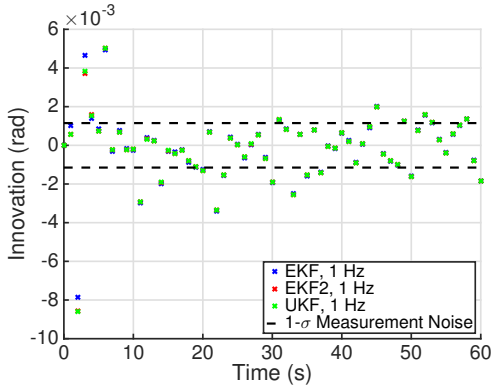

(b)

Figure 3.13. Comparison of EKF, EKF2 and UKF representative single trial innovations, physical pendulum process model with accurate measurements: (a) depicts 100 Hz measurements and (b) 1 Hz measurements.

3.4.2 Poor Measurements

The results shown in Figures 3.14 and 3.15 are produced using measurements with Gaussian noise, $\sim \mathcal{N}(0 \text{ rad}, 1.0 \times 10^{-4} \text{ rad}^2)$, representing potentiometer measurement noise. They are presented to demonstrate that the frequency effect on filter performance is not a result of the measurement noise level, but rather is a direct result of the covariance propagation. The average error is greater than when using more accurate measurements at both frequencies due to the lower quality measurement information. Comparison of Figures 3.9 and 3.14 at 100Hz and Figures 3.10 and 3.15 at 1Hz, respectively, demonstrates the effect that measurement quality has on the average error.

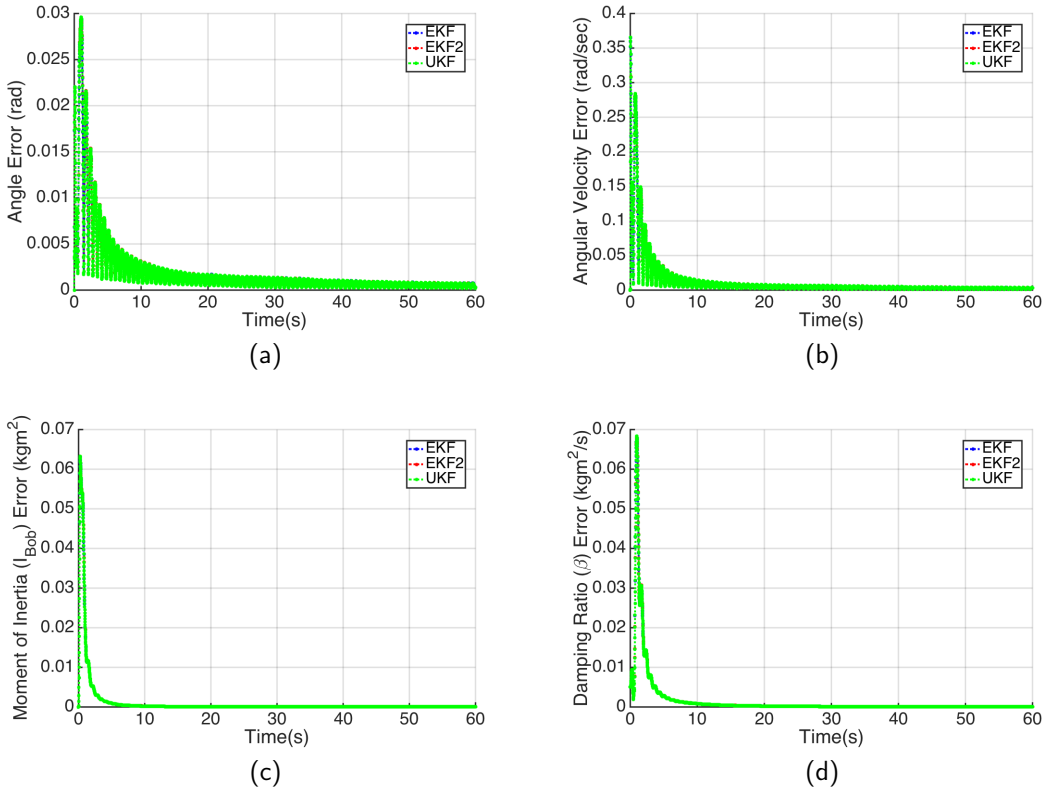

Figure 3.14. Comparison of EKF, EKF2, UKF estimation performance using a physical pendulum process model with poor 100Hz measurements, 100 trial average: (a) depicts average absolute angle (x_1) error, (b) average absolute angular velocity (x_2) error, (c) average absolute I_{Bob} (x_3) error and (d) average absolute damping ratio, β, (x_4) error.

The average innovation should reflect the measurement noise when the estimator is per-

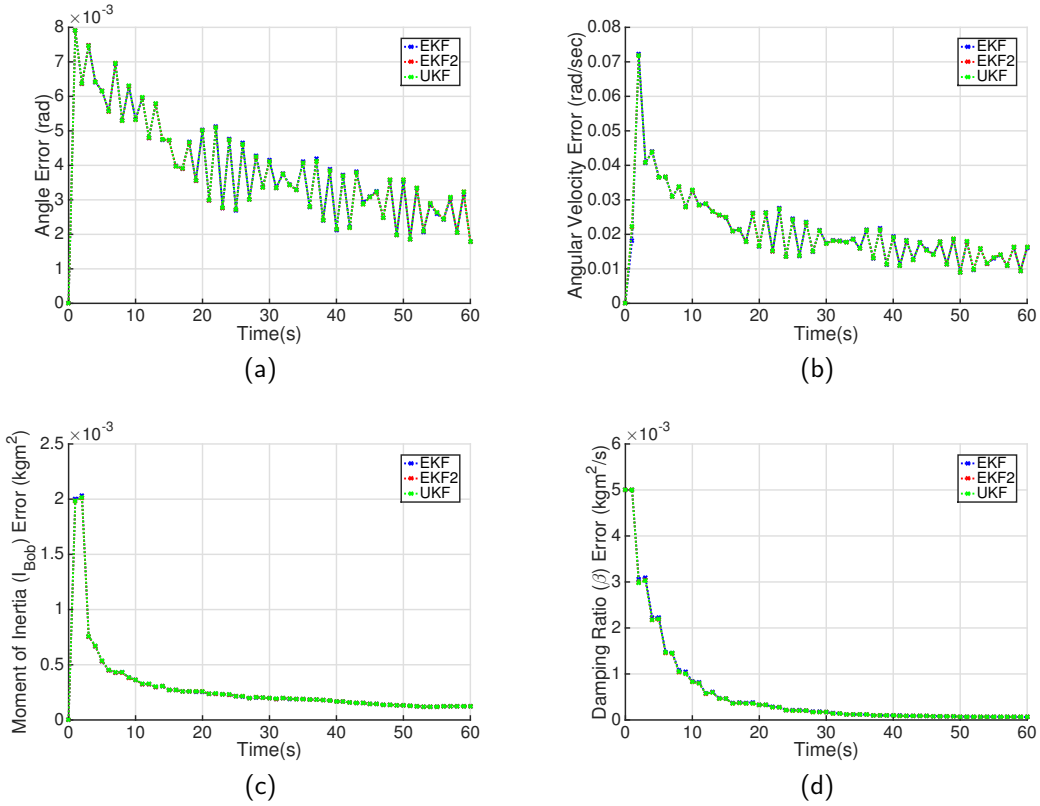

Figure 3.15. Comparison of EKF, EKF2, UKF estimation performance using a physical pendulum process model with poor 1Hz measurements, 100 trial average: (a) depicts average absolute angle (x_1) error, (b) average absolute angular velocity (x_2) error, (c) average absolute I_{Bob} (x_3) error and (d) average absolute damping ratio, β, (x_4) error.

forming as designed in steady state. The average innovations shown in Figure 3.16 demonstrate that the filters operate as anticipated in steady-state, but as a result of the poor measurement information, steady-state is not obtained at the same time as in Figure 3.12.

A representative single trial's innovations are presented in Figure 3.17 for comparison with the experimental results shown later in Figure 3.23.

The simple pendulum simulation reveals that estimator performance is not impacted despite using a measurement frequency, 1 Hz, approximately equivalent the pendulum's period, 0.8 Hz. These results do not preclude EKF sensitivity to lower measurement rates, such as 0.1 Hz, that have measurement intervals spanning multiple periods.

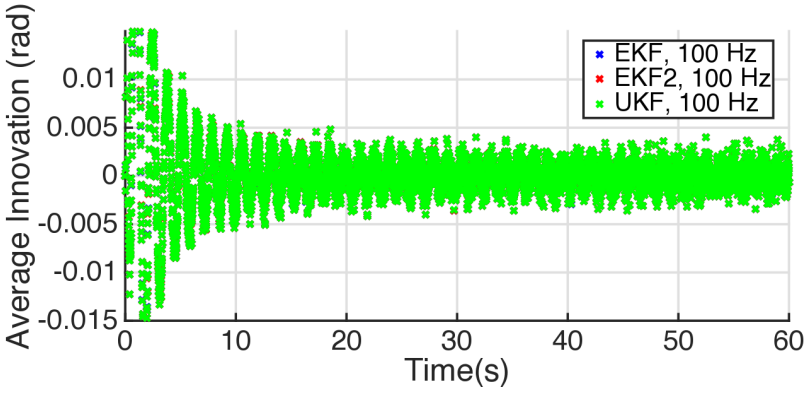

(a)

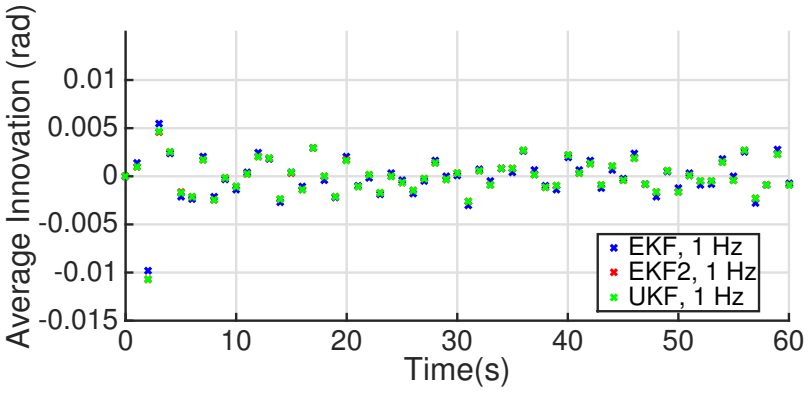

(b)

Figure 3.16. Comparison of EKF, EKF2 and UKF 100 trial average innovations, physical pendulum process model with poor measurements: (a) depicts 100 Hz measurements and (b) 1 Hz measurements.

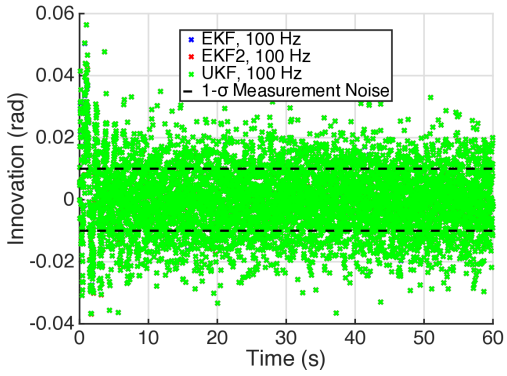

(a)

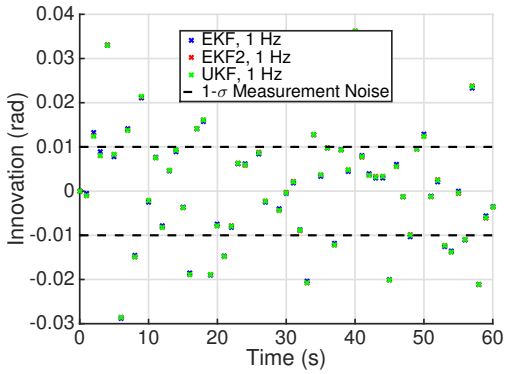

(b)

Figure 3.17. Comparison of EKF, EKF2 and UKF representative single trial innovations, physical pendulum process model with poor measurements: (a) depicts 100 Hz measurements and (b) 1 Hz measurements.

3.5 Experimental Results

A single trial of the pendulum experiment is conducted using the data collection system described in Section 3.2. The experiment is performed to verify that the EKF, EKF2, and UKF respond to varied measurement frequency in the same manner in practical application and simulation. An assumption of Gaussian noise is made despite the encoder and potentiometer displaying quantization noise in Figure 3.5.

The measurement interval is irregular since the data is collected at the fastest possible rate for the system. Results presented as 100 Hz are sampled at an average frequency of 100 Hz, but include data sampled as slow as 90 Hz and as fast as 189 Hz. Results presented as 1 Hz are sampled at an average frequency of 1.002 Hz, but include data sampled as slow as 0.999 Hz and as fast as 1.068 Hz.

3.5.1 Accurate Measurements

Figure 3.18 show bias in the innovations indicative of the challenges associated with applying a filter without process noise in application. Despite the process model mismatch that is visible in the form of the structured innovations, all three estimators converge after approximately $t = 5$ s at the 100 Hz measurement frequency. Figure 3.19 shows I_{Bob}, x_3, and damping coefficient, x_4, attain a steady-state result around which their values oscillate after this time. All estimators produce nearly identical results; only the UKF, which is plotted last, is visible. Figure 3.20 shows that all estimators also converge in I_{Bob}, x_3, and damping coefficient, x_4 after approximately $t = 5$ s at the 1 Hz measurement frequency. Interestingly, the damping coefficient is estimated to be negative in the dynamic response when using the 100 Hz measurement frequency. A negative damping coefficient has the effect of adding energy into the pendulum system contrary to the experiment set-up. All estimators maintain a positive damping coefficient when using the 1 Hz measurement frequency.

The estimators produce nearly identical results at both measurement frequencies as clearly seen in Figures 3.21b and 3.22b. The experiment confirms the simulation results presented in Figures 3.9 and 3.10. Measurement frequency does not impact the EKF performance at lower measurement frequencies as seen in the falling body problem.

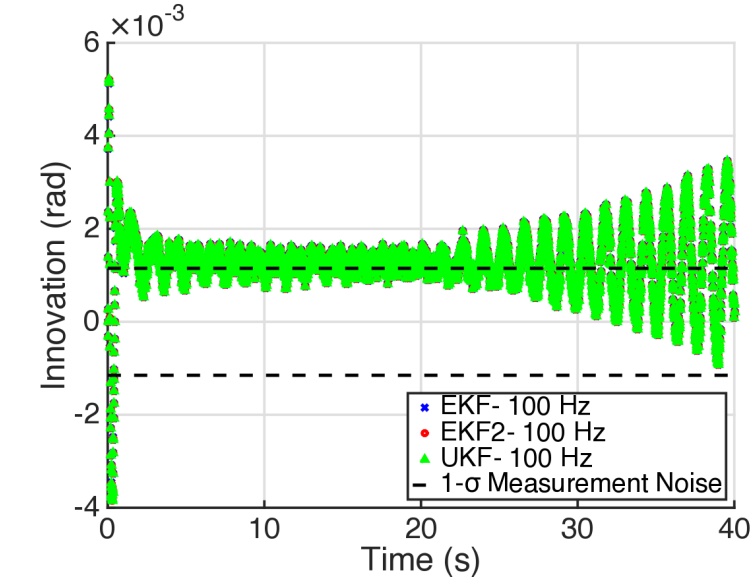

(a)

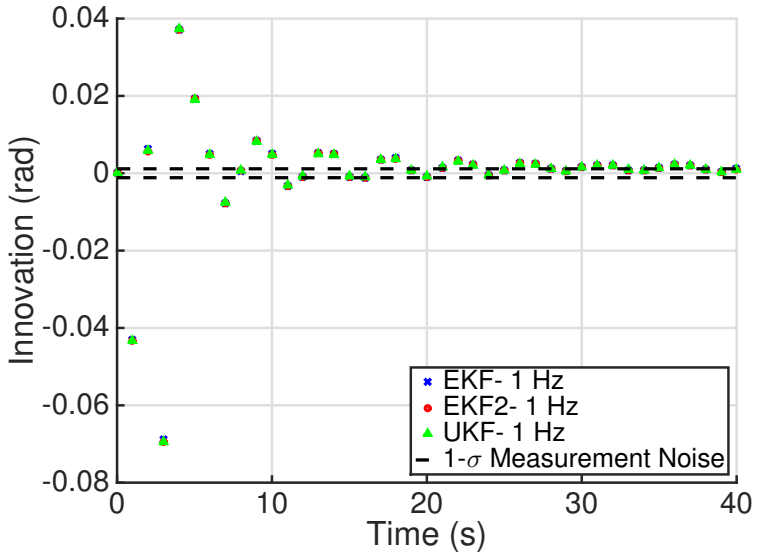

(b)

Figure 3.18. Comparison of EKF, EKF2 and UKF innovations, pendulum experiment single trial, with accurate measurements: (a) depicts 100 Hz measurements and (b) 1 Hz measurements.

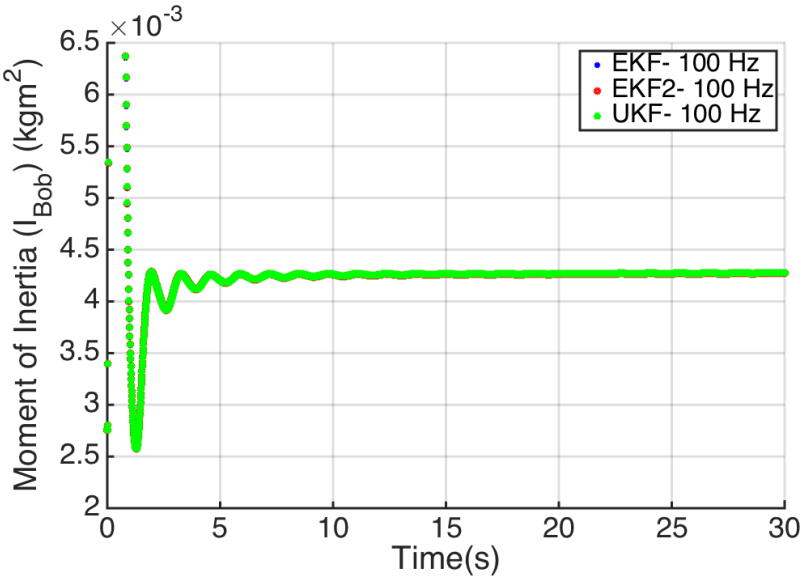

(a)

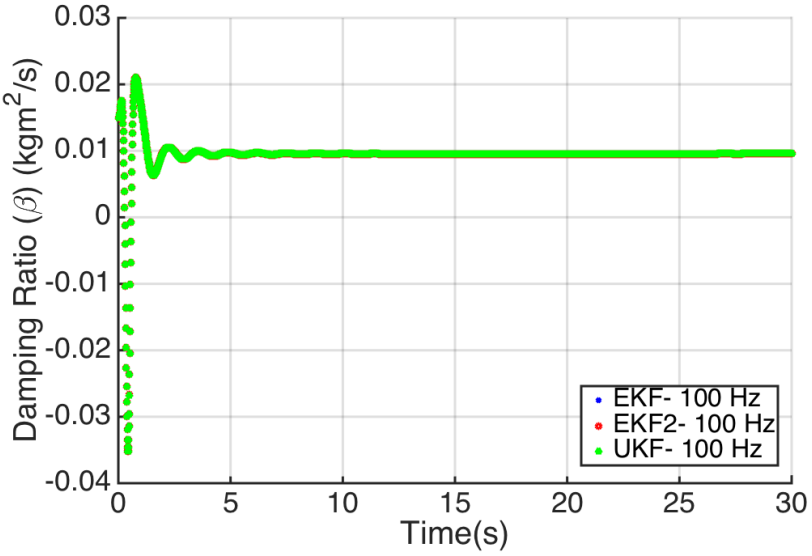

(b)

Figure 3.19. Comparison of EKF, EKF2 and UKF performance, pendulum experiment single trial, with 100 Hz accurate measurements: (a) depicts I_{Bob} (x_3) and (b) damping ratio, β (x_4).

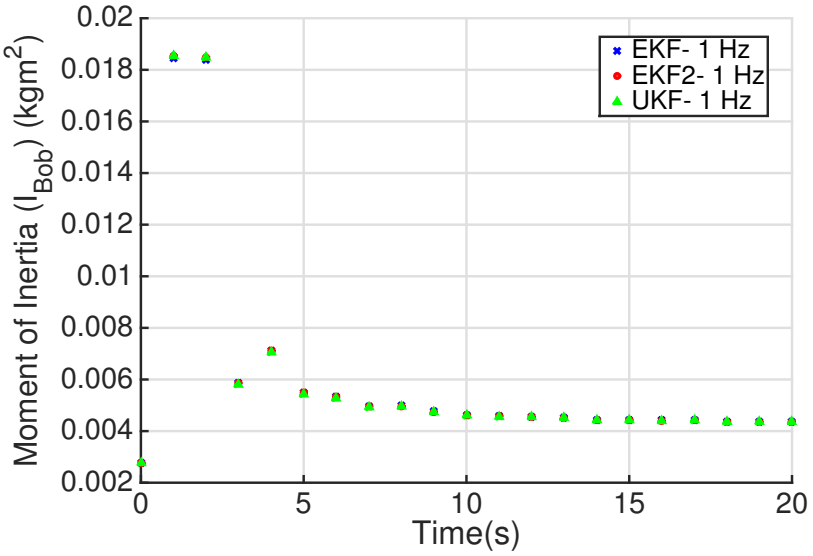

(a)

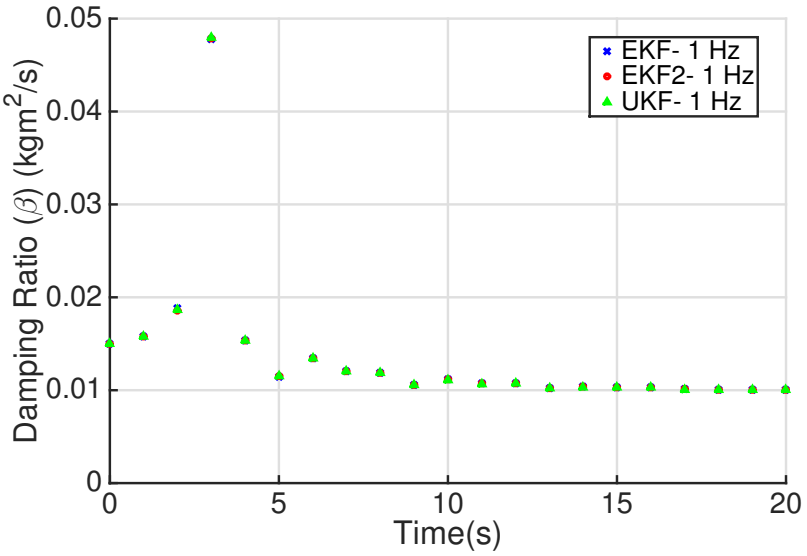

(b)

Figure 3.20. Comparison of EKF, EKF2 and UKF performance, pendulum experiment single trial, with 1 Hz accurate measurements: (a) depicts I_{Bob} (x_3) and (b) damping ratio, β (x_4).

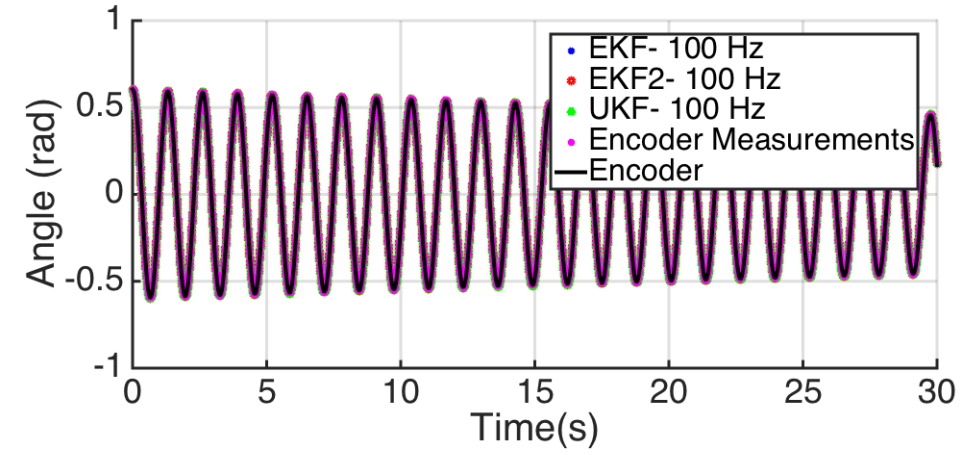

(a)

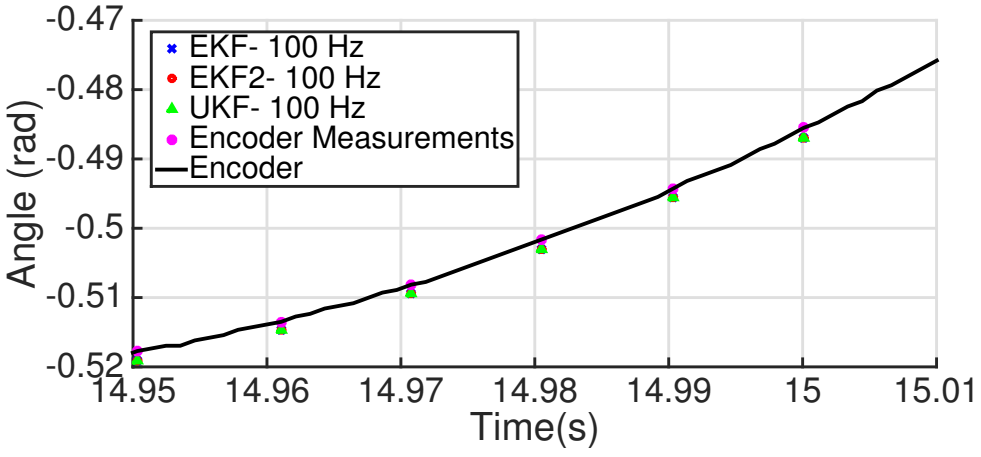

(b)

Figure 3.21. Comparison of EKF, EKF2 and UKF performance, pendulum experiment single trial, with 100 Hz accurate measurements: (a) depicts angle (x_1) and (b) angle (x_1), expanded view.

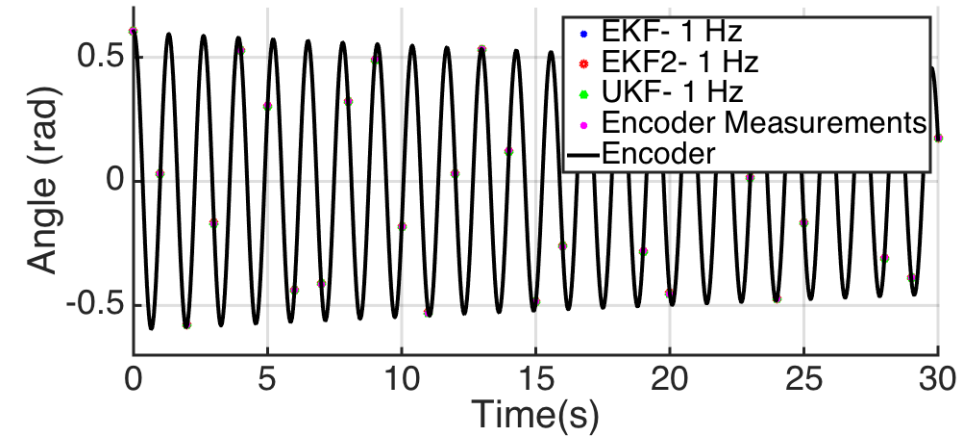

(a)

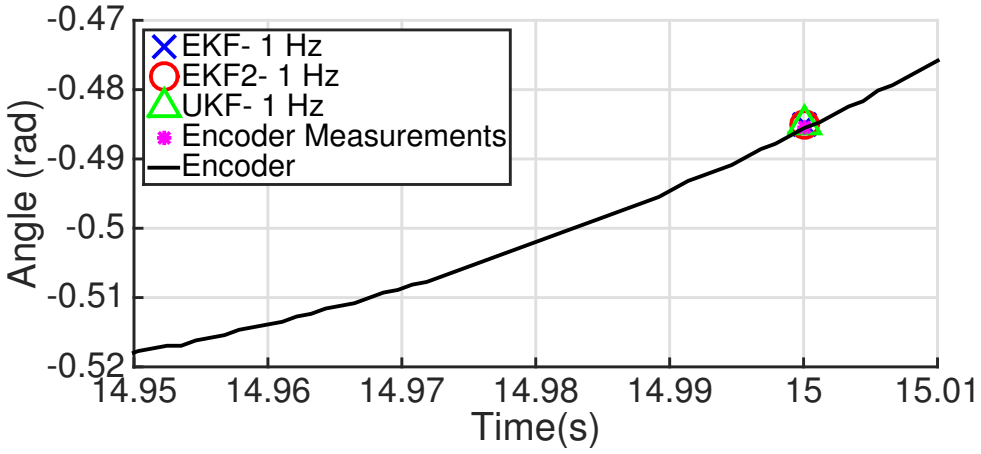

(b)

Figure 3.22. Comparison of EKF, EKF2 and UKF performance, pendulum experiment single trial, with 1 Hz accurate measurements: (a) depicts angle (x_1) and (b) angle (x_1), expanded view.

3.5.2 Poor Measurements

Estimator convergence properties are most clearly revealed through innovations shown in Figure 3.23. The innovations are biased at both frequencies. The effects of process model

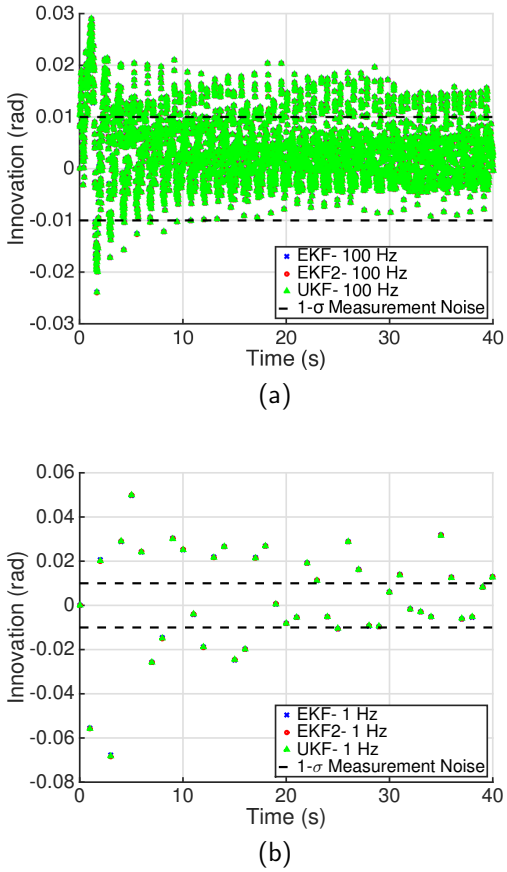

Figure 3.23. Comparison of EKF, EKF2 and UKF innovations, pendulum experiment single trial, with poor measurements: (a) depicts 100 Hz measurements and (b) 1 Hz measurements.

and measurement model errors result in the innovations failing to display Gaussian noise characteristics.

Figure 3.24 shows that all estimators reach steady-state in I_{Bob}, x_3, and damping coefficient, x_4 after approximately $t = 15$ s at the measurement 100 Hz frequency. Close inspection of Figure 3.24 reveals that the measurement model error, the potentiometer hysteresis, prevents the full convergence that exists in simulation. All estimators produce nearly identical

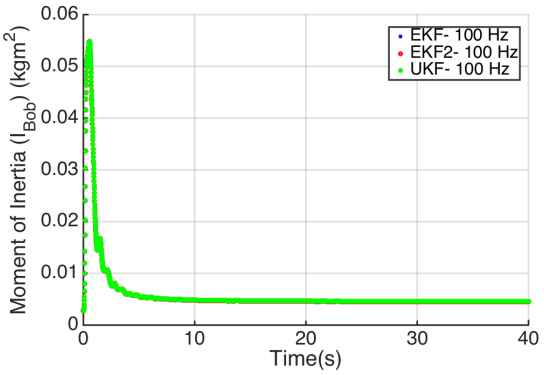

(a)

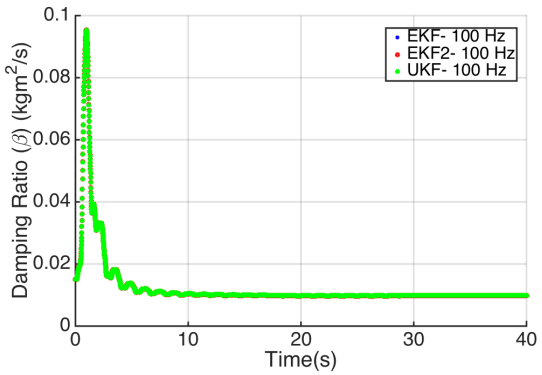

(b)

Figure 3.24. Comparison of EKF, EKF2 and UKF performance, pendulum experiment single trial, with 100 Hz poor measurements: (a) depicts I_{Bob} (x_3) and (b) damping ratio, β (x_4).

results; only the UKF, which is plotted last, is visible. Figure 3.25 shows that all estimators fail to converge in I_{Bob}, x_3, and damping coefficient, x_4 prior to $t = 40$ s at the 1 Hz measurement frequency. The initial dynamic response is less than half the magnitude of the 100 Hz measurement frequency. All estimators maintain a positive damping coefficient at both measurement frequencies in contrast to the use of encoder measurements at 100 Hz.

The estimators produce nearly identical results as can be clearly seen in Figures 3.26b and 3.27b at both measurement frequencies. The experiment confirms the simulation results presented in Figures 3.14 and 3.15. Measurement frequency does not impact the EKF performance at lower 1 Hz measurement frequencies as seen in the falling body problem.

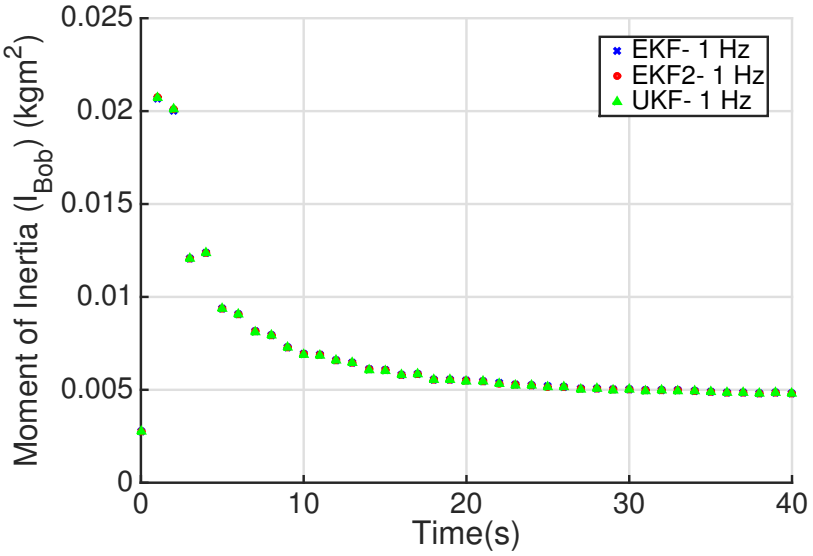

(a)

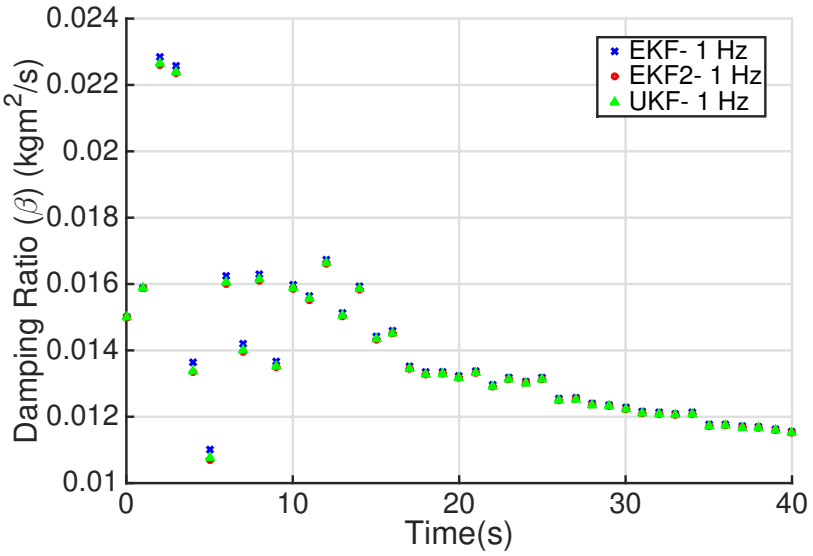

(b)

Figure 3.25. Comparison of EKF, EKF2 and UKF performance, pendulum experiment single trial, with 1 Hz poor measurements: (a) depicts I_{Bob} (x_3) and (b) damping ratio, β (x_4).

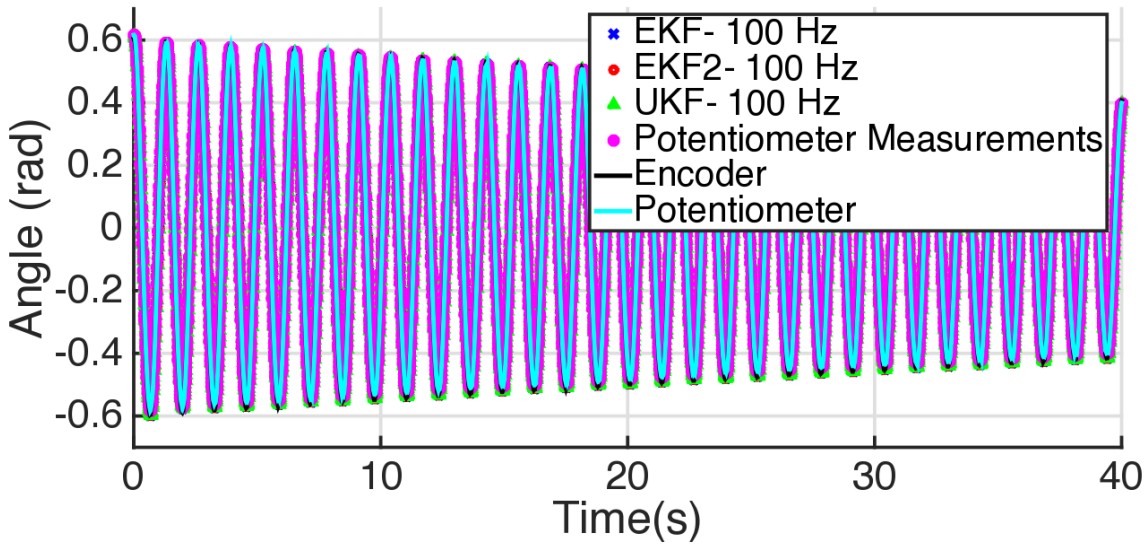

(a)

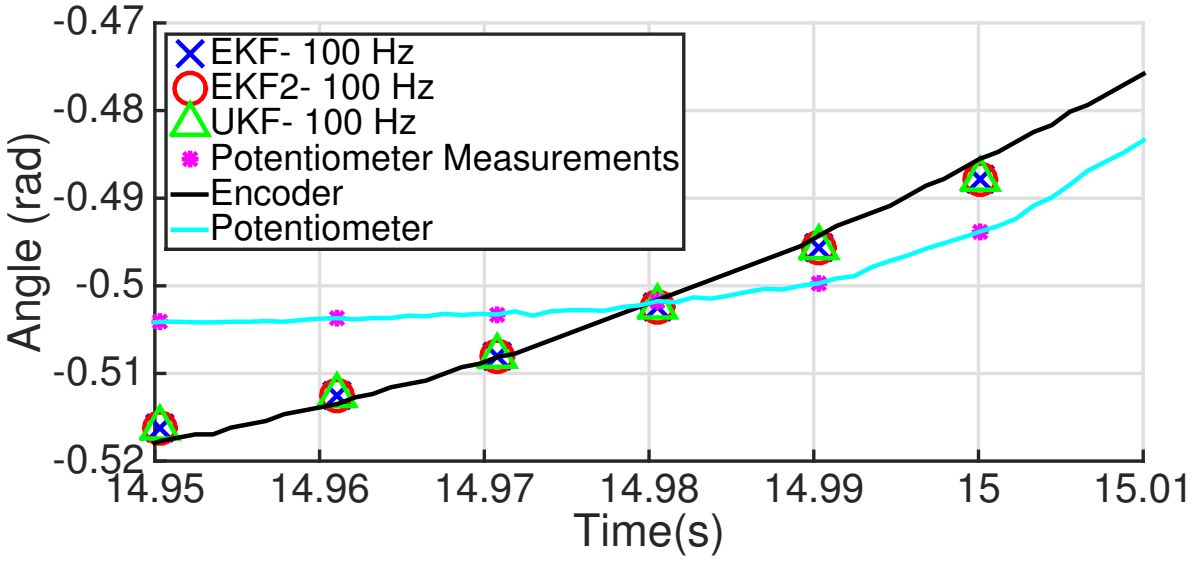

(b)

Figure 3.26. Comparison of EKF, EKF2 and UKF performance, pendulum experiment single trial, with 100 Hz poor measurements: (a) depicts angle (x_1) and (b) angle (x_1), expanded view.

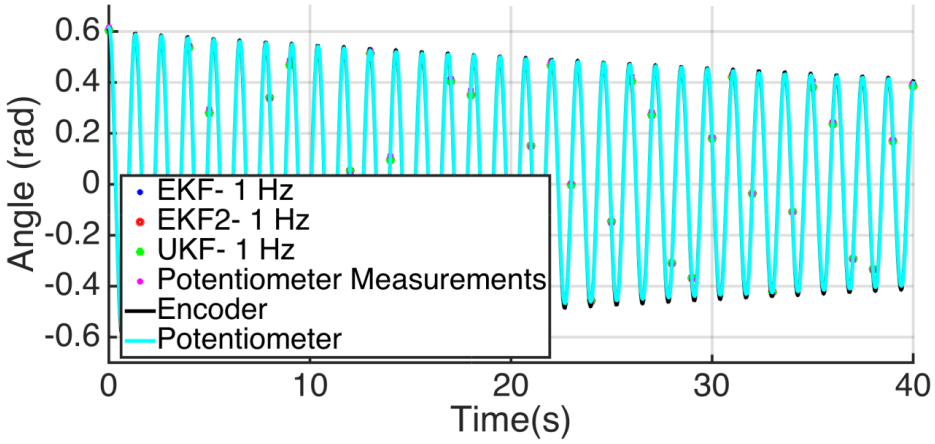

(a)

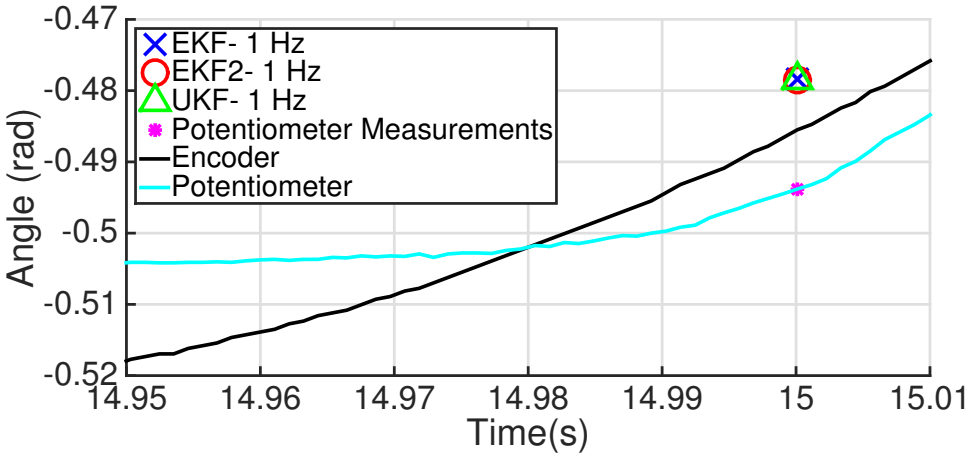

(b)

Figure 3.27. Comparison of EKF, EKF2 and UKF performance, pendulum experiment single trial, with 1 Hz poor measurements: (a) depicts angle (x_1) and (b) angle (x_1), expanded view.

3.6 Conclusions

The experimental results of Section 3.5 validate the results obtained through simulation in Section 3.4. Although only a single experimental trial is presented in this dissertation, multiple experimental trials were conducted that produced near identical EKF and UKF estimator performance. The experimental confirmation of the simulation provides confidence that the results of a sufficiently large Monte Carlo study of another problem should produce results that would be experimentally confirmed.

Additionally, the simple pendulum problem studied in this chapter reveals the effect of measurement frequency on EKF performance is not visible in all nonlinear estimation problems. While the UKF demonstrated superior performance at low measurement frequencies in comparison to the EKF for the single-dimension falling body problem of Chapter 2, both the EKF and UKF displayed nearly identical performance when using relatively sparse measurements in estimating pendulum parameters. This result, when viewed in conjunction with the Chapter 2 results, helps to explain the conflicting views regarding KF–based nonlinear estimator performance present in the literature.

Chapter 4 seeks to provide tools to help determine whether measurement frequency will impact EKF or UKF performance. The single-dimension falling body and pendulum problems provide examples to develop concepts for determining sensitivity to sparse measurements in other nonlinear estimation applications.

THIS PAGE INTENTIONALLY LEFT BLANK

CHAPTER 4:
Predicting Estimator Sensitivity to Sparse Temporal Measurements

The measurement frequency sensitivity present in the falling body problem (Chapter 2) is not seen in the pendulum problem (Chapter 3). The EKF and UKF estimate the *a priori* covariance using different approximations that may affect estimator performance in some applications. This chapter presents an approach to predict the sensitivity of KF–based nonlinear estimators to sparse temporal measurements.

The primary difference between the UKF and EKF is the approximation used to allow application of the KF structure. As noted in Chapter 1, an approximation is necessary to apply the KF structure to a problem with a nonlinear process or measurement model. The UT approximates the estimated state's PDF whereas the EKF approximates the nonlinear transformation. Section 4.1 considers analysis of covariance propagation using the different approximations to determine estimator sensitivity to measurement frequency.

Analysis of the covariance propagation over an entire trajectory is challenging and would provide little value in problems that are highly nonlinear over only limited portions of the state trajectory (i.e., the falling body problem considered in Chapter 2). Therefore, Section 4.2 investigates the impact of the EKF approximation through consideration of the process model linearization that occurs in the EKF. The Jacobian and covariance propagation analysis techniques are applied to the falling body and pendulum problems in Section 4.3. Conclusions are provided in Section 4.4.

4.1 Covariance Propagation Analysis

The KF structure produces a state estimate that is a linear combination of a predicted state estimate and the scaled difference of the actual and predicted measurements [3]. The scaling factor, or Kalman gain, is determined from the *a priori*, or propagated, covariance, as shown in Equation (1.12). As a result, the information available in the measurement is only properly incorporated if the *a priori* covariance is computed accurately. The measurement information is not properly used if the covariance is underestimated. In this case, the esti-

mator "trusts" the prediction and rejects the measurement information update. Maybeck [8] notes that underestimating covariance leads to filter divergence. In instances when the covariance is overestimated, the filter "trusts" the measurement more, and the predicted state is unnecessarily updated and filter effectiveness is reduced.

The response of the nonlinear KF–based estimators is similarly responsive to covariance estimation errors. Thus, propagation of an arbitrary covariance matrix through a specified nonlinear transformation over a varied time interval provides insight into each filter's performance. Propagation by the Monte Carlo technique using a sufficiently large number of trials provides an asymptotically close approximation of the true propagated covariance matrix. This result can be compared with propagation performed using the first-order Taylor series linearization (EKF) and the UT (UKF) to determine predicted filter performance over different measurement intervals.

There are many different approaches to compare the EKF and UKF covariance matrix propagation with the Monte Carlo propagation. Similarity of the EKF and UKF covariance matrices, respectively, with the Monte Carlo propagation provides one useful measure. The JBLD divergence value, detailed in Equation (2.18), is used as a measure of covariance matrix similarity.

Additionally, a comparison of each term along the main diagonal of the covariance matrices can provide insight. This comparison is used to gain a sense of whether the covariance associated with each state is correctly estimated, underestimated, or overestimated. Relative estimation performance is useful to predict whether the filter will be unnecessarily rejecting or improperly incorporating measurement information.

The JBLD divergence value similarity comparison and the main diagonal analysis approaches are applied to the falling body problem in Section 4.3.1 and the pendulum problem in Section 4.3.2.

4.2 Jacobian Analysis

The EKF uses the state transition matrix to propagate the estimated covariance as shown in Equation (1.32). The state transition matrix shown in Equation (4.1) [5] is integrated to

produce a state transition matrix that spans the integration interval.

$$\frac{d\Phi_{t_{k+1},t_k}}{dt} = \Phi \tag{4.1}$$

where, $\Phi = \left.\frac{\partial f(x,t)}{\partial x}\right|_{x=\hat{x}^-}$. The linearization point in the EKF is the *a posteriori* state estimate. Therefore, the distance from the linearization point at the time of the next measurement increases as the measurement interval increases. An integration interval shorter than the measurement interval can be employed to reduce linearization error by dividing the measurement interval propagation into shorter integration steps [20]. The state transition matrix is assumed to be the identity matrix at the start of the integration interval.[13]

While relatively small integration time steps will reduce the numerical linearization error, systems may experience a rapid change in the Jacobian such that linearization error from the EKF algorithm becomes apparent when the measurement interval is relatively long. The process model Jacobian, the partial derivative of the dynamic model, provides insight as to the effect that measurement frequency will have in a given problem.

The Jacobian is multi-dimensional and time varying in most practical applications prohibiting determination of the linearization error through inspection. A time varying metric is needed to locate regions along the trajectory where EKF performance may be degraded over longer measurement intervals. The Frobenius norm is one such metric that is suitable for this application. The Frobenius norm of the Jacobian reduces the required analysis of the multi-dimensional matrix to consideration of a time-varying scalar. The time varying Frobenius norm can further be differentiated to provide insight as to the Jacobian rate of change along the state trajectory.

This approach is applied to the falling body problem in Section 4.3.1 and the pendulum problem in Section 4.3.2 to demonstrate that the Frobenius norm of the Jacobian is useful in determining regions of the state trajectory that require additional inspection using the techniques of Section 4.1.

[13]The initial state transition matrix is the identity matrix because the state does not change spontaneously.

4.3 Analysis Application Examples

The concepts presented in Sections 4.1 and 4.2 are applied to two problems, the single-dimension falling body of Chapter 2 and the simple pendulum of Chapter 3, to demonstrate their value in helping to predict the KF–based nonlinear estimator sensitivity to sparse temporal measurements.

4.3.1 Falling Body Problem

Equation (4.2) shows the process model Jacobian for the falling body problem.

$$F(x,t) = \frac{\partial f(x,t)}{\partial x} = \begin{bmatrix} 0 & -1 & 0 & 0 \\ \gamma \exp(-\gamma x_1) x_2^2 x_3 & -2\exp(-\gamma x_1) x_2 x_3 & -\exp(-\gamma x_1) x_2^2 & 1 \\ 0 & 0 & 0 & 0 \\ 0 & 0 & 0 & 0 \end{bmatrix} \tag{4.2}$$

The Frobenius norm of the Jacobian is shown in Equation (4.3). This value provides a metric to study the change in the Jacobian with respect to time. High rates of change in the Jacobian indicate regions of the state trajectory that may be subject to increased linearization error, as discussed in Section 4.2.

$$\|F(x,t)\|_F = \sqrt{\exp(-1 \times 10^{-4} x_1) \left(x_2^4 + 4(x_2 x_3)^2 + 2.5 \times 10^{-9} (x_2^4 x_3^2) \right) + 2} \tag{4.3}$$

Figure 4.1 shows the Frobenius norm of the Jacobian evaluated along the simulation truth trajectory. The rate of change of the Frobenius norm of the Jacobian provides some insight into the impact of measurement interval on the propagation of covariance. Figure 4.1b shows the change in the Jacobian with respect to time for the truth model. The rather large magnitude change in the Frobenius norm of the Jacobian can translate into error in the estimated covariance. This effect may be addressed by reducing the integration time step during the measurement interval to avoid significant numerical linearization errors, but it cannot overcome the error resulting from the state being a large distance away from the linearization point in this portion of the trajectory.

This analysis technique fails to provide insight as to the specific state that will be most impacted, but points to a significant challenge to the EKF's underlying assumptions. The UKF is not impacted by this specific approximation error. However, it is susceptible to

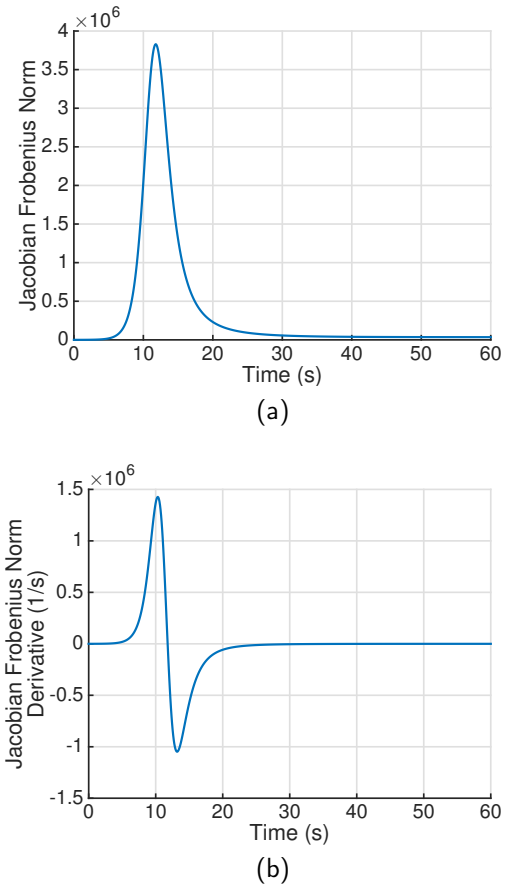

Figure 4.1. Falling body process model Jacobian Frobenius norm, along simulation truth trajectory: (a) depicts the process model Jacobian Frobenius norm and (b) the derivative of the process model Jacobian Frobenius norm.

mismatches between the actual state PDF versus the PDF represented by the sigma points. Higher-order moment mismatch is more visible in the covariance estimate than the state estimate [19].

Additional insight is obtained by propagating the state for both 0.5 and 2 second intervals with an arbitrarily assumed covariance starting at different points in the state trajectory. Propagation is performed using the Monte Carlo technique with 10,000 random points to generate an approximation of the true covariance propagation. This value is compared with covariance propagation via the state transition matrix used in the EKF and the unscented transform used in the UKF.

The covariance shown in Equation (4.4) is propagated for a 2 second interval assuming the state value at 8 seconds, 10 seconds, and 12 seconds.

$$P_0 = \begin{bmatrix} 1 \times 10^6 & 0 & 0 & 0 \\ 0 & 1 \times 10^6 & 0 & 0 \\ 0 & 0 & 2.5 \times 10^{-9} & 0 \\ 0 & 0 & 0 & 1 \times 10^{-4} \end{bmatrix} \tag{4.4}$$

Covariance propagation commencing at 0 seconds is provided for comparison as the results shown in Section 2.3.2 reflect similar initial EKF and UKF estimation performance in spite of the longer measurement interval. Results from each starting time are shown in Table 4.1. The state transition and UT approaches generate the identical JBLD divergence value for

Table 4.1. JBLD divergence value comparison of the state transition matrix and UT propagated covariance similarity with Monte Carlo propagated covariance, falling body problem, 2 second propagation.

t_0	0 (s)	8 (s)	10 (s)	12 (s)
State Transition	1.6118×10^{-2}	1.6360×10^{-2}	1.5734×10^{-2}	3.1684×10^{-2}
UT	1.6118×10^{-2}	1.5745×10^{-2}	1.1009×10^{-2}	2.0880×10^{-2}

the 0 second starting time. The UT produces a covariance matrix that is more similar to the Monte Carlo at the 8, 10, and 12 second starting points. The difference between the state transition matrix and UT divergence values is largest at the 12 second starting point.

The percent of covariance propagation error between the state transition and UT techniques and the Monte Carlo propagation is shown in Figure 4.2. The covariance of each state is represented by the respective covariance matrix main diagonal term.

These results demonstrate that propagation of covariance internal to the EKF predictor step underestimates the velocity covariance by approximately 2.5% for the time interval from 10 to 12 seconds. While additional factors also effect EKF performance, this is the root cause for the estimator being unable to take proper advantage of further measurement information. The UKF also underestimates the velocity covariance by approximately 0.6%, but it continues to function.

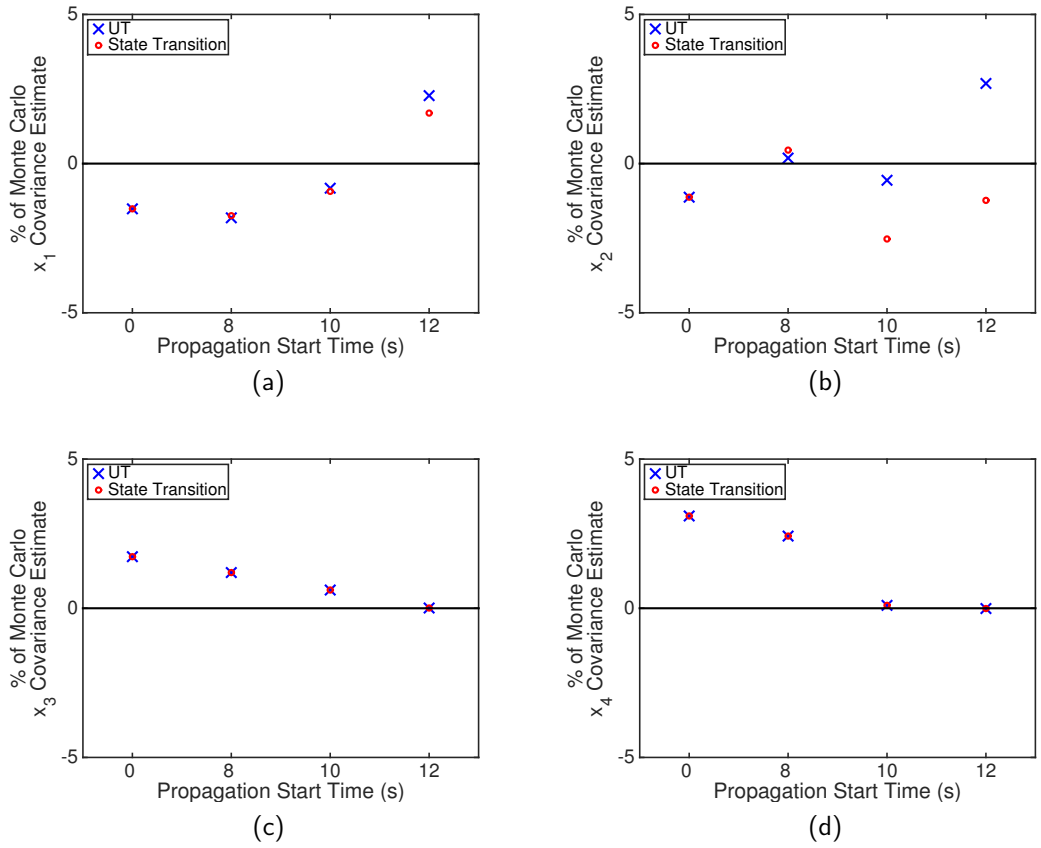

Figure 4.2. Arbitrary 2 sec covariance propagation from the specified falling body truth trajectory starting point: (a) depicts altitude, x_1, covariance % error, (b) velocity, x_2, covariance % error, (c) ballistic coefficient, x_3, covariance % error, and (d) gravitational acceleration, x_4, covariance % error.

Figure 4.2 also shows that the propagation of covariance internal to the UKF predictor step overestimates the altitude covariance by approximately 2.3% and the velocity covariance by approximately 2.7% for the time interval from 12 to 14 seconds. This overestimation results in the large altitude estimation error seen in Figure 2.9. This analysis does not account for a potential PDF mismatch in that the initial PDF is assumed to be Gaussian for each propagation.

Covariance propagation for 0.5 seconds, the propagation interval equivalent with the 2 HZ measurement frequency, is shown in Figure 4.3. The EKF and UKF propagation approx-

imation techniques produce covariance results nearly identical to one another with the magnitude of the greatest difference less than 0.01%. This explains the nearly identical performance between the methods as seen in Figure 2.6.

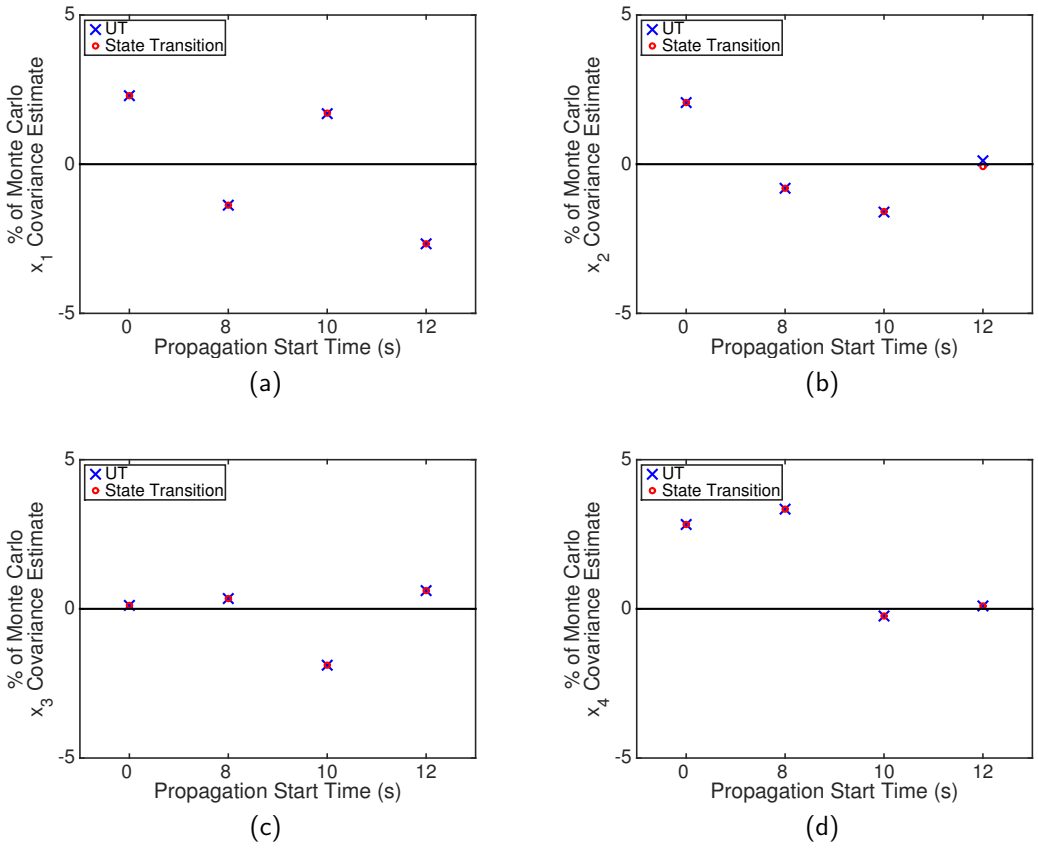

Figure 4.3. Arbitrary 0.5 sec covariance propagation from the specified falling body truth trajectory starting point: (a) depicts altitude, x_1, covariance % error, (b) velocity, x_2, covariance % error, (c) ballistic coefficient, x_3, covariance % error, and (d) gravitational acceleration, x_4, covariance % error.

JBLD divergence values are shown in Table 4.2. These values demonstrate that the propagated covariance matrices are nearly identical starting at the four different points along the state trajectory at the 2 Hz measurement frequency. The similar accuracy of the propagated covariance is reflected in similar performance achieved by the EKF and UKF using 2 Hz measurements.

Table 4.2. JBLD divergence value comparison of the state transition matrix and UT propagated covariance similarity with Monte Carlo propagated covariance, falling body problem, 0.5 second propagation.

t_0	0 (s)	8 (s)	10 (s)	12 (s)
State Transition	1.9468×10^{-2}	1.8545×10^{-2}	1.5307×10^{-2}	1.2719×10^{-2}
UT	1.9468×10^{-2}	1.8547×10^{-2}	1.5318×10^{-2}	1.2728×10^{-2}

4.3.2 Pendulum Problem

Sparse temporal measurements do not produce a similar effect on the EKF steady-state performance in the pendulum problem as seen in Section 2.3. However, analysis of this problem helps to predict when a measurement frequency induced difference in steady-state estimation error would not occur in other problems.

Equation (4.5) shows the process model Jacobian for the pendulum problem.

$$F(x,t) = \frac{\partial f(x,t)}{\partial x} = \begin{bmatrix} 0 & 1 & 0 & 0 \\ -\frac{MLg\cos(x_1)}{x_3+I} & \frac{-x_4}{x_3+I} & \frac{MLg\sin(x_1)+x_2x_4}{(x_3+I)^2} & \frac{-x_2}{x_3+I} \\ 0 & 0 & 0 & 0 \\ 0 & 0 & 0 & 0 \end{bmatrix} \tag{4.5}$$

The Frobenius norm of the Jacobian, shown in Equation (4.6), is considered for comparison with the falling body problem.

$$\begin{aligned} \|F(x,t)\|_F = \; & \left(\frac{1}{(x_3+0.0159)^2}\right) \cdot \Big(\left(x_2^2 + x_4^2 + 0.1982\left(\cos(x_1)\right)^2\right)(x_3+0.0159)^2 + \\ & (0.4452\sin(x_1) + x_2x_4)^2 + (x_3+0.0159)^4 \Big)^{\frac{1}{2}} \end{aligned} \tag{4.6}$$

Figure 4.4 shows the Frobenius norm of the Jacobian evaluated along the simulation truth trajectory. The rate of change of the Frobenius norm of the Jacobian is shown in Figure 4.4b. The magnitude and rate of change decrease as the magnitude of the pendulum oscillation is damped. The largest rate of change in the Jacobian occurs at the start of the trajectory, in contrast to the falling body problem, as shown in Figure 4.4b.

An arbitrary covariance matrix, Equation (4.7), is propagated forward in a similar fashion

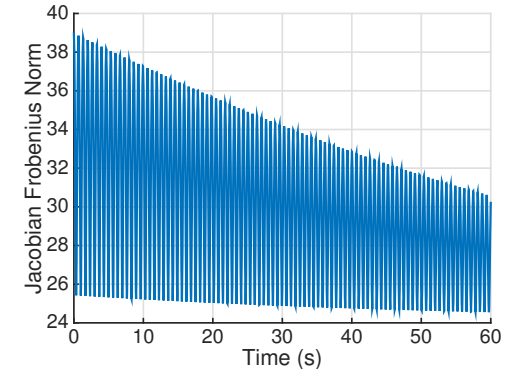

(a)

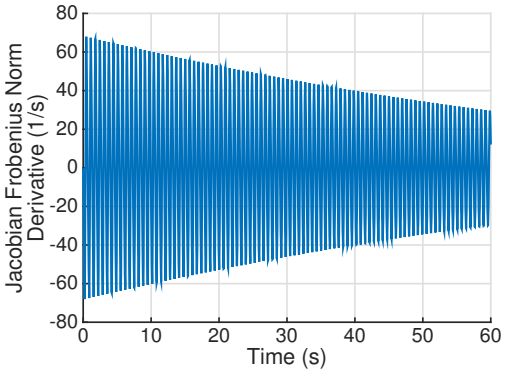

(b)

Figure 4.4. Pendulum process model Jacobian Frobenius norm, along simulation truth trajectory: (a) depicts the process model Jacobian Frobenius norm and (b) the derivative of the process model Jacobian Frobenius norm.

to the analysis performed in Section 4.3.1.

$$\begin{bmatrix} 1\times10^{-4} & 0 & 0 & 0 \\ 0 & 1\times10^{-4} & 0 & 0 \\ 0 & 0 & 1\times10^{-8} & 0 \\ 0 & 0 & 0 & 1\times10^{-6} \end{bmatrix} \tag{4.7}$$

The state transition and UT propagated covariance matrices for propagation intervals of 0.01, 1, 2, and 10 seconds are compared with covariance matrices propagated using a 10,000 point Monte Carlo. All propagation commences at $t = 0$ seconds, the point in the state trajectory corresponding with the largest rate of change of the Jacobian. JBLD di-

vergence values are shown in Table 4.3. These divergence values characterize the effect the

Table 4.3. JBLD divergence value comparison of the state transition matrix and UT propagated covariance similarity with Monte Carlo propagated covariance, pendulum problem, varied propagation interval.

Propagation Interval	0.01 (s)	1 (s)	2 (s)	10 (s)
State transition	1.5413×10^{-2}	1.5679×10^{-2}	1.7018×10^{-2}	8.4330×10^{-1}
UT	1.5410×10^{-2}	1.4887×10^{-2}	1.4348×10^{-2}	1.5430×10^{-2}

different propagation approaches have on the covariance matrices. Propagation intervals representative of 100 Hz and 1 Hz demonstrate small differences between the state transition and UT covariance propagation. However, the UT covariance propagation remains substantially more like the Monte Carlo propagated covariance as the propagation interval lengthens in excess of one pendulum period.

As discussed in Section 4.3.1, the JBLD divergence value information is complemented by the comparison of propagated covariance through the % error of the main diagonal terms. These values are shown in Figure 4.5 and stand in contrast to the falling body problem comparison shown in Figure 4.2. The covariance propagation is nearly identical over the intervals associated with the measurement frequencies presented. Exceptionally long measurement time intervals, on the order of 10 seconds, are necessary to demonstrate the difference in propagation approaches.

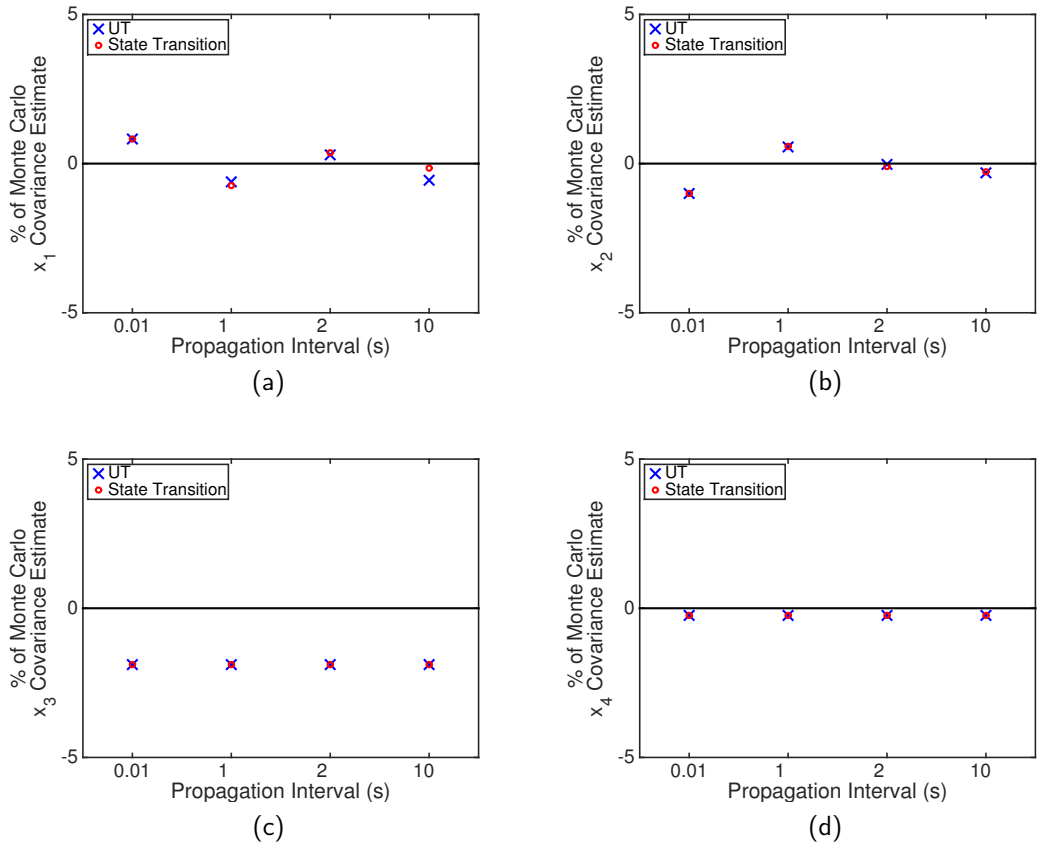

Figure 4.5. Comparison of covariance propagation from $x(t = 0)$: (a) depicts angle, x_1, covariance % error, (b) angular velocity, x_2, covariance % error, (c) I_{Bob}, x_3, covariance % error, and (d) damping coefficient, x_4, covariance % error.

4.4 Conclusions

This chapter presents an analysis approach to determine if sparse temporal measurements are expected to impact KF–based nonlinear estimator performance. The nonlinearity of the process model can be characterized through the rate of change of the Frobenius norm of the Jacobian evaluated along the state trajectory. The Frobenius norm of the Jacobian is used to provide a scalar metric for comparison. This approach highlights regions of interest where a linearized approximation of the nonlinear transformation may result in significant approximation error.

Insight into estimator performance can be gained through propagation of an arbitrary co-

variance over the measurement interval. Details of this approach are discussed in Section 4.1. Comparison of covariance propagation using the state transition matrix and the UT, respectively, with a Monte Carlo propagation reveals the quality of the covariance estimate. The single-dimension falling body problem and the simple pendulum are analyzed using the proposed approach. The analysis method confirms that the falling body EKF estimator is susceptible to deteriorating performance as the measurement interval lengthens. The EKF estimator for the pendulum problem is shown not impacted by measurement intervals considered in Chapter 3.

THIS PAGE INTENTIONALLY LEFT BLANK

CHAPTER 5:
Conclusions and Future Work

5.1 Conclusions

This dissertation investigates the effect of measurement frequency on KF–based nonlinear estimators. The EKF and UKF employ fundamentally different approximation techniques to the challenging nonlinear estimation problem. Details of each filter's construction are presented in Chapter 1. The KF requires propagation of both the state's mean and covariance between measurement intervals. Propagation is necessary to generate a predicted state, as the mean and covariance at the measurement time are required to describe the state. The predicted state is corrected through a weighted linear combination of the difference between the measurement and the predicted measurement.

Julier and Uhlmann [11] note that the UKF's approximation technique is more accurate than the first order Taylor series linearization used by the EKF. This view leads to an expectation that the UKF should outperform the EKF in steady-state in instances with a lengthy measurement interval. Conversely, one would expect that the filters should perform similarly over sufficiently short measurement intervals. The same measurement frequency, and its associated propagation interval, may be sufficiently fast in one problem while relatively slow in another.

This hypothesis is validated through the use of two example problems, the single dimension falling body of Chapter 2 and a simple pendulum investigated in Chapter 3. The measurement frequency is shown to significantly alter the relative performance of the EKF and UKF in the first problem, but has minimal impact in the second. Further analysis is presented in Chapter 4 demonstrating use of the Frobenius norm of the Jacobian matrix along the state trajectory to characterize system nonlinearity. Characterization allows for targeted investigation of covariance propagation with different approximation techniques.

Covariance overestimation leads to poor estimator performance, but does not lead to complete estimator failure. However, filter divergence occurs when the covariance is underestimated and must be avoided. Covariance propagation interval length can greatly impact both

the relative quality and direction of estimation error. This error can be described through use of a similarity comparison between the covariance matrices generated by different approximation approaches and a Monte Carlo propagated covariance matrix. This analysis provides a sense of the propagation quality. Determination of the direction of estimation error, either under or over, is shown through comparison of propagated covariance matrices main diagonal components.

Lengthened measurement intervals reveal undocumented challenges with UKF implementation. All sigma point vectors components should satisfy constraints to ensure valid propagation of the state estimate. Chapter 2 demonstrates that initialization can lead to sigma point vectors that violate constraints. While the UKF may still function, it can produce unpredictable results depending upon the specific system dynamics. This aspect should alter the manner in which a UKF is initialized.

Chapter 2 presents a novel approach to constraining sigma points. The scaled UT, initially created to minimize non local effects and match higher-order moments, is demonstrated to improve the UKF's robustness by altering the sigma point vectors without changing the represented mean and covariance. Application of the scaled UT for the purpose of respecting state constraints requires the mean to be located in the allowable region. This can be achieved in the UKF construct through enforcement of the constraints on the *a posteriori* state estimate. The UKF-S presented in Chapter 2 uses adaptive scaling of the Kalman gain to ensure that the *a posteriori* state estimate respects constraints. Kalman gain scaling and the scaled UT are applied only as necessary to respect parameter constraints.

5.2 Future Work

The addition of process noise can be used to mask the effect of measurement frequency. This can be particularly effective approach to improve estimator robustness at the expense of estimation accuracy. Application of an UKF-S without the use of process noise may demonstrate robust performance without the expense of reducing estimator accuracy.

As noted, UKF-S performance may be improved by altering the size of the minimum hypersphere radius along the state trajectory. The effect of sigma points located in close proximity to the mean is significantly reduced in regions that are approximately linear. The results presented in Chapter 2 suggest that the guard band size may be altered to limit the negative

effect of the smaller hyper-sphere radius in the more nonlinear region of the trajectory.

Further work is needed to verify the applicability of the presented measurement frequency analysis on more complex dynamic systems such as those implemented in inertial navigation systems. Additionally, high-order moment-matched sigma points, such as the CUT or HS points briefly mentioned in Chapter 1 may improve covariance propagation in nonlinear transformations in which the higher-order moments have a greater impact. A constrained UKF may benefit from representing process and measurement noise with a bounded vice Gaussian PDF.

THIS PAGE INTENTIONALLY LEFT BLANK

List of References

[1] Bowditch, N., *The American Practical Navigator: An Epitome of Navigation*, Defense Mapping Agency Hydrographic/Topographic Center, Bethesda, MD, 1995.

[2] Titterton, D. H. and Weston, J. L., *Strapdown Inertial Navigation Technology*, IEE Radar, Sonar, Navigation, and Avionics Series, Institution of Electrical Engineers, 2nd ed., 2004.

[3] Kalman, R. E., "A New Approach to Linear Filtering and Prediction Problems," *Journal of Fluids Engineering*, Vol. 82, No. 1, 1960, pp. 35–45.

[4] Sorenson, H. W., "Least-squares estimation: From Gauss to Kalman," *IEEE Spectrum*, Vol. 7, No. 7, 1970, pp. 63–68.

[5] Gelb, A., editor, *Applied Optimal Estimation*, M.I.T. Press, Cambridge, Mass, 1974.

[6] Whittle, P., *Probability via Expectation*, Springer Science & Business Media, 4th ed., Dec. 2012.

[7] Crassidis, J. L. and Junkins, J. L., *Optimal Estimation of Dynamic Systems*, Chapman & Hall/CRC Applied Mathematics and Nonlinear Science Series, Chapman & Hall/CRC, 2004.

[8] Maybeck, P. S., *Stochastic Models, Estimation, and Control Volume 1*, Vol. 141-1 of *Mathematics in Science and Engineering*, Academic Press, Inc., Orlando, FL, 1979.

[9] Simon, D., *Optimal State Estimation: Kalman, H∞ and Nonlinear Approaches*, Wiley-Interscience, Hoboken, N.J., 2006.

[10] Hand, D. J., *Statistics: A Very Short Introduction*, Oxford University Press, New York, 2008.

[11] Julier, S. and Uhlmann, J., "Unscented Filtering and Nonlinear Estimation," *Proceedings of the IEEE*, Vol. 92, No. 3, March 2004, pp. 401–422.

[12] Julier, S. J. and Uhlmann, J. K., "New Extension of the Kalman Filter to Nonlinear Systems," *AeroSense 1997*, Vol. 3068, International Society for Optics and Photonics, Orlando, FL, 1997, pp. 182–193.

[13] Julier, S. J., Uhlmann, J. K., and Durrant-Whyte, H. F., "A New Approach for Filtering Nonlinear Systems," *Proceedings of the 1995 American Control Conference*, Vol. 3, IEEE, 1995, pp. 1628–1632.

[14] Julier, S. J. and Uhlmann, J. K., "Reduced Sigma Point Filters for the Propagation of Means and Covariances Through Nonlinear Transformations," *Proceedings of the 2002 American Control Conference*, Vol. 2, IEEE, 2002, pp. 887–892.

[15] Julier, S., "The Spherical Simplex Unscented Transformation," *Proceedings of the 2003 American Control Conference*, Vol. 3, June 2003, pp. 2430–2434.

[16] Gustafsson, F. and Hendeby, G., "Some Relations Between Extended and Unscented Kalman Filters," *IEEE Transactions on Signal Processing*, Vol. 60, No. 2, 2012, pp. 545–555.

[17] Adurthi, N., Singla, P., and Singh, T., "The Conjugate Unscented Transform—An Approach to Evaluate Multi-dimensional Expectation Integrals," *Proceedings of the 2012 American Control Conference*, IEEE, 2012, pp. 5556–5561.

[18] Ross, I. M., Proulx, R. J., Karpenko, M., and Gong, Q., "Riemann–Stieltjes Optimal Control Problems for Uncertain Dynamic Systems," *Journal of Guidance, Control, and Dynamics*, Vol. 38, No. 7, July 2015, pp. 1251–1263.

[19] Frontera, P. J., Proulx, R. J., Karpenko, M., and Ross, I. M., "Analysis of Hyper-pseudospectral Transformation of Random Variables," *Proceedings of the 2015 AAS/AIAA Astrodynamic Specialists Conference*, AIAA, Vail, CO, Aug. 2015.

[20] Maybeck, P. S., *Stochastic Models, Estimation, and Control Volume 2*, Vol. 141-2 of *Mathematics in Science and Engineering*, Academic Press, Inc., New York, Aug. 1982.

[21] Challa, S. and Bar-Shalom, Y., "Nonlinear Filter Design Using Fokker-Planck-Kolmogorov Probability Density Evolutions," *IEEE Transactions on Aerospace and Electronic Systems*, Vol. 36, No. 1, 2000, pp. 309–315.

[22] Daum, F., "Nonlinear Filters: Beyond the Kalman Filter," *IEEE Aerospace and Electronic Systems Magazine*, Vol. 20, No. 8, Aug. 2005, pp. 57–69.

[23] Rao, C., Rawlings, J., and Mayne, D., "Constrained State Estimation for Nonlinear Discrete-time Systems: Stability and Moving Horizon Approximations," *IEEE Transactions on Automatic Control*, Vol. 48, No. 2, Feb. 2003, pp. 246–258.

[24] Patwardhan, S. C., Narasimhan, S., Jagadeesan, P., Gopaluni, B., and L. Shah, S., "Nonlinear Bayesian State Estimation: A Review of Recent Developments," *Control Engineering Practice*, Vol. 20, No. 10, Oct. 2012, pp. 933–953.

[25] Athans, M., Wishner, R., and Bertolini, A., "Suboptimal State Estimation for Continuous-time Nonlinear Systems from Discrete Noisy Measurements," *IEEE Transactions on Automatic Control*, Vol. 13, No. 5, Oct. 1968, pp. 504–514.

[26] Kailath, T., *Lectures on Wiener and Kalman Filtering*, No. 140 in Courses and Lectures, Springer Verlag, 1981.

[27] Kurt-Yavuz, Z. and Yavuz, S., "A Comparison of EKF, UKF, FastSLAM2. 0, and UKF-Based FastSLAM Algorithms," *Proceedings of the 16th International Conference on Intelligent Engineering Systems (INES), 2012*, IEEE, 2012, pp. 37–43.

[28] Ristic, B., Farina, A., Benvenuti, D., and Arulampalam, M., "Performance Bounds and Comparison of Nonlinear Filters for Tracking a Ballistic Object on Re-entry," *IEE Proceedings - Radar, Sonar and Navigation*, Vol. 150, No. 2, 2003, pp. 65.

[29] Crassidis, J. L., "Sigma-point Kalman filtering for integrated GPS and inertial navigation," *Aerospace and Electronic Systems, IEEE Transactions on*, Vol. 42, No. 2, 2006, pp. 750–756.

[30] Giannitrapani, A., Ceccarelli, N., Scortecci, F., and Garulli, A., "Comparison of EKF and UKF for Spacecraft Localization via Angle Measurements," *IEEE Transactions on Aerospace and Electronic Systems*, Vol. 47, No. 1, 2011, pp. 75–84.

[31] Allotta, B., Chisci, L., Costanzi, R., Fanelli, F., Fantacci, C., Meli, E., Ridolfi, A., Caiti, A., Di Corato, F., and Fenucci, D., "A comparison between EKF-based and UKF-based navigation algorithms for AUVs localization," *OCEANS 2015-Genova*, IEEE, 2015, pp. 1–5.

[32] Rhudy, M., Gu, Y., and R., M., "An Analytical Approach for Comparing Linearization Methods in EKF and UKF," *International Journal of Advanced Robotic Systems*, 2013, pp. 1.

[33] LaViola, J., "A Comparison of Unscented and Extended Kalman Filtering for Estimating Quaternion Motion," *Proceedings of the 2003 American Control Conference*, Vol. 3, June 2003, pp. 2435–2440 vol.3.

[34] Julier, S. J., "The Scaled Unscented Transformation," *Proceedings of the 2002 American Control Conference*, Vol. 6, IEEE, 2002, pp. 4555–4559.

[35] NøRgaard, M., Poulsen, N. K., and Ravn, O., "New Developments in State Estimation for Nonlinear Systems," *Automatica*, Vol. 36, No. 11, 2000, pp. 1627–1638.

[36] Alfriend, K. T. and Lee, D.-J., "Nonlinear Bayesian Filtering for State and Parameter Estimation," *Proceedings of the Sixth US/Russian Space Surveillance Workshop: August 22-26, 2005*, Central Astronomical Observatory at Pulkovo, Russian Academy of Sciences, 2005, p. 199.

[37] Vittaldev, V., Russell, R. P., Arora, N., and Gaylor, D., "Second-order Kalman Filters Using Multi-complex Step Derivatives," *American Astronomical Society*, Vol. 204, 2012.

[38] Simon, D., "Kalman Filtering with State Constraints: A Survey of Linear and Nonlinear Algorithms," *IET Control Theory & Applications*, Vol. 4, No. 8, Aug. 2010, pp. 1303–1318.

[39] Teixeira, B. O. S., Tôrres, L. A., Aguirre, L. A., and Bernstein, D. S., "Unscented Filtering for Interval-Constrained Nonlinear Systems," *CDC*, 2008, pp. 5116–5121.

[40] Vachhani, P., Narasimhan, S., and Rengaswamy, R., "Robust and Reliable Estimation via Unscented Recursive Nonlinear Dynamic Data Reconciliation," *Journal of Process Control*, Vol. 16, No. 10, Dec. 2006, pp. 1075–1086.

[41] Kandepu, R., Foss, B., and Imsland, L., "Applying the Unscented Kalman Filter for Nonlinear State Estimation," *Journal of Process Control*, Vol. 18, No. 7, 2008, pp. 753–768.

[42] Kolås, S., Foss, B., and Schei, T., "Constrained Nonlinear State Estimation Based on the UKF Approach," *Computers & Chemical Engineering*, Vol. 33, No. 8, Aug. 2009, pp. 1386–1401.

[43] Julier, S., Uhlmann, J., and Durrant-Whyte, H. F., "A New Method for the Nonlinear Transformation of Means and Covariances in Filters and Estimators," *IEEE Transactions on Automatic Control*, Vol. 45, No. 3, 2000, pp. 477.

[44] Vemulapalli, R. and Jacobs, D. W., "Riemannian Metric Learning for Symmetric Positive Definite Matrices," *arXiv preprint arXiv:1501.02393*, 2015.

[45] Cherian, A., Sra, S., Banerjee, A., and Papanikolopoulos, N., "Efficient Similarity Search for Covariance Matrices via the Jensen-Bregman LogDet Divergence," *2011 International Conference on Computer Vision*, IEEE, 2011, pp. 2399–2406.

[46] Close, C. M. and Frederick, D. K., *Modeling and Analysis of Dynamic Systems*, Wiley, New York, 2nd ed., Jan. 1993.

[47] Hodgman, C. D., editor, *Handbook of Chemistry and Physics*, Chemical Rubber Publishing Company, Cleveland, OH, 34th ed., 1952.

Initial Distribution List

1. Defense Technical Information Center
   Ft. Belvoir, Virginia

2. Dudley Knox Library
   Naval Postgraduate School
   Monterey, California